The role of TBX2 and the anti-cancer activity of Chromomycin A5 in Pancreatic Ductal Adenocarcinoma

By

Jinming Bai

This thesis is presented for the degree of

MSc (Med) in Cell Biology

Supervisor: Prof. Sharon Prince

Co-supervisor: Dr. Karabo Serala

Division of Cell Biology
Department of Human Biology
Faculty of Health Sciences
University of Cape Town
South Africa

January 10, 2025

DECLARATION

I, ***Jinming Bai***, hereby declare that the work on which this thesis is based is my original work (except where acknowledgements indicate otherwise) and that neither the whole work nor any part of it has been, is being, or is to be submitted for another degree in this or any other university.

I empower the university to reproduce for the purpose of research either the whole or any portion of the contents in any manner whatsoever.

Signed by candidate

Jinming Bai

January 10, 2025

Acknowledgments

As I reach the completion of this thesis, I am filled with profound gratitude for all those who have supported me throughout this transformative academic journey. This accomplishment, representing years of dedication and collaborative effort, would not have been possible without the collective support and guidance of many remarkable individuals.

First and foremost, I am deeply indebted to those who have directly shaped my academic development. I would like to express my deepest gratitude to my supervisor, Professor Sharon Prince, for her exceptional guidance, profound knowledge, and unwavering support. Her rigorous academic standards and dedication to research have not only guided my academic pursuits but have also set an inspiring example for my future career. I am particularly grateful to Dr. Karabo Serala for his valuable advice and care throughout my research. My sincere thanks also go to Dr. Annick van Niekerk, Dr. Lucy Macharia, Dr. Saif Khan and Dr. Mihlali Vuyo Mlaza for their meticulous assistance in proofreading this thesis.

I would like to acknowledge my laboratory colleagues who have been instrumental in the success of my experimental work: Anjani Rama, Carly Burmeister, Nirvashi Autar, Dr. Claire Bellis, Dr. Thato Medupe, Dr. Mohsin Khan, Dr. Athi Welsh, Dr. Stephanie Ncube, Dr. Abid Ali, Tawfeeq Khalfe, Michael Goldschagg, Oreneile Maiphetlho, Kiera Hürlimann, Jenna Mühlberg, Ayesha Shaik, Sidrah Palekar, Rodrigo Miguel, Dr. Supratim Biswas, Associate Prof. Dirk Lang, and Dr. Tim Reid. Their technical guidance, valuable experimental advice, and shared expertise have been crucial in overcoming research challenges and achieving successful outcomes.

I am deeply indebted to Guru Liu, Rui Zhang, and Han Zhang for guiding me to South Africa and helping me establish my life here. Special thanks to Zebiao Wu for his

extensive computer technical support, which greatly enhanced both my research and daily life. I am particularly grateful to Junjie Shi, Bingyu Bai, Aobing Zeng, and Yu Li for serving as my emergency contacts in Cape Town and providing immediate assistance whenever needed.

My heartfelt appreciation goes to Peiyi Wang, Yifan Zhang, Philo Yang, Yinxiin Zeng, Kui KiKi Ching Lam, Mika Chan, and Vivian Cheung for their professional support and emotional encouragement. I would also like to thank counsellor Li, Yun Wang, Danzeng Zhuogua, Rebecca Lee, Master Rumu Shi, Frans van Beeck, and Dr. Chen Tian for their guidance in my spiritual growth.

Most importantly, I want to express my profound gratitude to my parents, Jie Bai and Yali Qu. Your unconditional love and support have been the foundation of all my achievements. This accomplishment is as much yours as it is mine.

While space constraints prevent me from naming everyone individually, I am deeply grateful to all those who have graced my journey with their presence and support. Moving forward, I shall strive to honour the wisdom and kindness received by dedicating myself to the betterment of humanity through rigorous scholarship and sincere service - for in this lies the true meaning of academic pursuit.

Research outputs

Publication

Serala K, **Bai J**, Prince S. Pyrvinium Pamoate Alone and With Gemcitabine Exhibits Anti-Pancreatic Cancer Activity in 2D and 3D Cell Culture Models. J Cell Mol Med. 2024 Dec;28(23):e70222. doi: 10.1111/jcmm.70222. PMID: 39632282; PMCID: PMC11617115.

Serala K, Mdletshe S, **Bai J**, Abrahams A, Gayet O, Moubri L, Dusetti N, Prince S. The T-box transcription factors TBX2 and TBX3 are molecular targets of piroctone olamine in the treatment of pancreatic cancer. In preparation.

Conferences

Bai J, Serala K, Prince S. Therapeutic strategies for pancreatic cancer: targeting the oncogenic transcription factor TBX2 with chromomycin A5. Oral presentation at: Biomedical Research & Innovation Platform (BRIP) Conference 2024; 2024 October 16-17; Cape Town, South Africa.

Bai J, Serala K, Prince S. Exploring New Therapeutic Strategies for Pancreatic Cancer: Targeting the Oncogenic Transcription Factor TBX2 with Novel Drug Treatments. Poster presented at: 28th Congress of the South African Society for Biochemistry and Molecular Biology (SASBMB); 2024 July 7-10; Polokwane, South Africa.

Serala K, Mdletshe S, **Bai J,** Abrahams A, Goding C, Prince S. The T-box Transcription Factors TBX2 and TBX3 are Molecular Targets of Piroctone Olamine in Pancreatic Ductal Adenocarcinoma. Poster presented at the 36th EORTC-NCI-AACR Symposium on Molecular Targets and Cancer Therapeutics; 2024 October 23-25; Barcelona, Spain.

TABLE OF CONTENTS

LIST OF FIGURES AND TABLES

Abstract

Pancreatic ductal adenocarcinoma (PDAC) remains one of the most lethal malignancies, with a dismal 5-year survival rate of 13%. Current treatments show limited efficacy due to late diagnosis and therapy resistance, highlighting an urgent need for novel therapeutic strategies. The T-box transcription factor, TBX2, is significantly overexpressed in PDAC tissues and correlates with poor prognosis and distant metastasis, suggesting its potential as a therapeutic target. Recently, Chromomycin A5 (CA5), a marine-derived compound, was identified as a TBX2-specific inhibitor with demonstrated anticancer effects in several cancer types. However, its efficacy in PDAC and the specific molecular mechanisms remains unexplored. This study aimed to: (1) elucidate the role of TBX2 in PDAC progression and its potential as a therapeutic target, and (2) evaluate the anticancer activity and underlying molecular mechanisms of CA5 in PDAC.

Initial screening for TBX2 expression over four PDAC cell lines identified SW1990 cells as high TBX2-expressing cells suitable for the functional studies. Both SW1990 and CFPAC-1 metastatic PDAC cells were ideal for drug evaluation studies. TBX2's function was assessed in SW1990 cells through siRNA-mediated knockdown followed by cell counting for proliferation analysis, wound healing assays for migration assessment, and western blot analysis of cell cycle regulators and EMT markers. CA5's anticancer activity was evaluated in both cell lines using 2D and 3D culture models (MTT cytotoxicity assays, colony formation assays, Matrigel transwell invasion assays, wound healing assays, and spheroid formation with Calcein-AM/propidium iodide viability staining), with gemcitabine serving as a reference drug. Molecular mechanisms of CA5 were investigated through fluorescence spectroscopy for DNA-binding, immunofluorescence and western blot detection of γH2AX for DNA damage

assessment, flow cytometry for cell cycle and Annexin V-FITC/PI apoptosis analyses, western blot analysis of apoptotic pathway proteins, and qRT-PCR examination of TBX2 and its downstream targets. The relationship between TBX2 expression and CA5 efficacy was further explored using doxycycline-inducible TBX2-overexpressing SW1990 cell lines established through the PiggyBac transposon system.

The study revealed that while TBX2 knockdown in SW1990 cells had minimal impact on cell proliferation, it significantly impaired cell migration through an EMT-independent mechanism. In both SW1990 and CFPAC-1 cells, CA5 demonstrated potent and selective anticancer activity in 2D and 3D models. Mechanistically, CA5 exhibited strong DNA-binding capabilities, as evidenced by fluorescence quenching and emission peak shifts. These DNA-binding properties increased γH2AX levels in both cell lines, triggering S-phase and G2/M cell cycle arrests in SW1990 cells and predominantly S-phase arrest in CFPAC-1 cells. CA5 activated primarily the intrinsic apoptotic pathway in SW1990 cells while engaging both intrinsic and extrinsic pathways in CFPAC-1 cells. Furthermore, CA5 reduced TBX2 protein levels in both cell lines and relieved its potential downstream tumour suppressors p21 and NDRG1.

This study demonstrated that TBX2 promotes PDAC cell migration through an EMT-independent mechanism, establishing its role in PDAC metastasis. Additionally, CA5 exhibits promising anticancer activity in PDAC cells through multiple mechanisms, including DNA damage induction and TBX2 inhibition, supporting its potential as a novel therapeutic agent for PDAC treatment.

CHAPTER 1
Literature Review

1.1. Pancreatic Cancer

Pancreatic cancer (PC) is a highly lethal malignancy with increasing incidence and mortality rates across the world[1]. According to global cancer statistics, the incidence and mortality rates of PC are approximately 4.7 and 4.2 per 100,000 people per year, respectively[2]. In 2020, the Global Cancer Observatory (GLOBOCAN) reported 495,773 new cases of PC and 466,003 cancer-related deaths, making it the seventh leading cause of cancer-related mortality worldwide[1]. In the absence of significant advancements in early detection methods, PC is projected to surpass breast cancer and become the second leading cause of cancer-related deaths by 2030[3]. The disease predominantly affects individuals over the age of 55 and demonstrates higher incidence and mortality rates in men compared to women[1]. Family history, chronic pancreatitis, smoking, and obesity are the main risks factors for PC[4,5]. For example, studies have shown that about 10% of PC patients have a family history, suggesting the importance of genetic factors in its pathogenesis[6]. Furthermore, chronic pancreatitis causes damage and carcinogenesis of pancreatic cells through long-term inflammatory reactions[7]. Smokers have twice the risk of developing PC compared to non-smokers, and obesity also significantly increases the risk of PC[6].

Based on histological characteristics, PC can be broadly classified into two main types: pancreatic ductal adenocarcinoma (PDAC) and pancreatic neuroendocrine tumours (PNETs)[8]. PDAC represents approximately 85-90% of all PC cases and is characterised by its aggressive nature and poor prognosis, while PNETs account for the remaining

PC cases and are associated with a favourable prognosis[9,10]. Due to the focus of the current thesis, the rest of the information on PC in this chapter will focus on PDAC.

1.1.1. Origins and molecular underpinnings of PDAC

The pancreas is a soft, flattened glandular organ with a characteristic yellowish appearance and it has distinct anatomical and functional characteristics[11]. Morphometric studies indicate that the adult pancreas measures approximately 15 centimetres in length with a mass ranging from 70 to 100 grams [11]. Anatomically, the organ is subdivided into four distinct regions: the head, which interfaces with the duodenum; the neck, which is adjacent to the portal vein; the body, positioned posterior to the pylorus; and the tail, which extends toward the splenic hilum[11] (**Figure 1.1**).

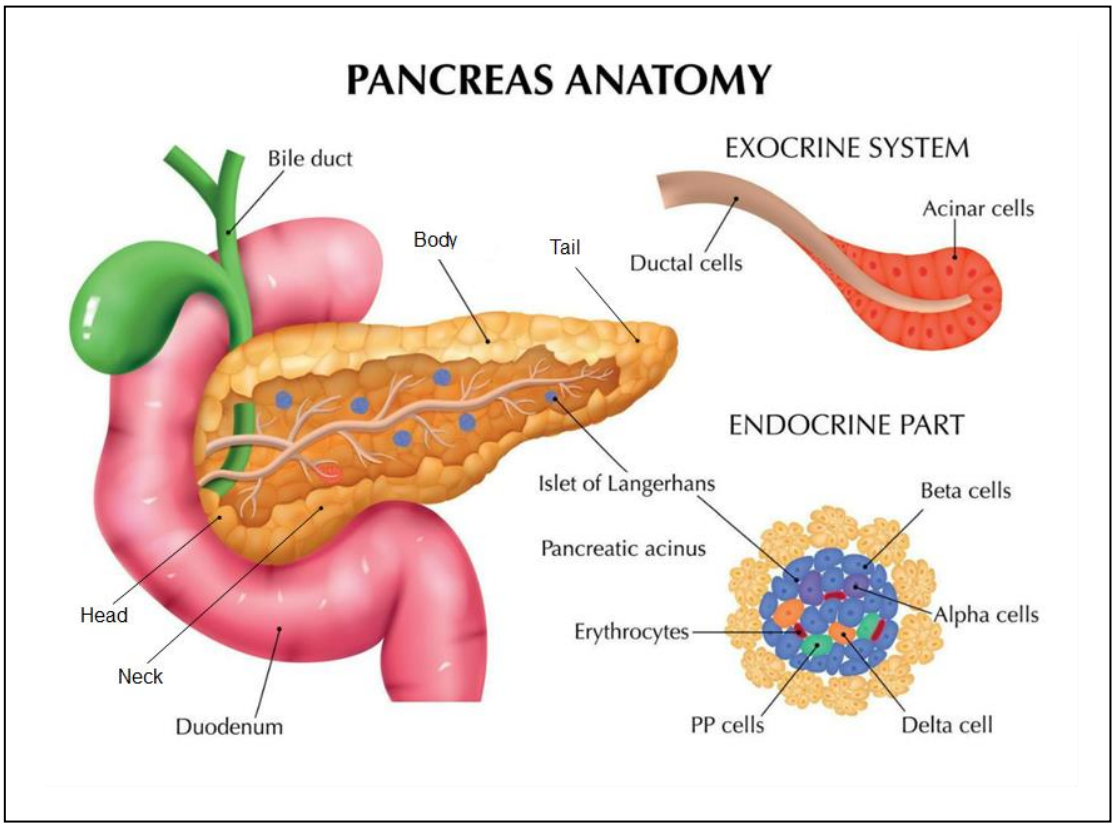

Figure 1.1. Schematic illustration of pancreatic anatomical structure and cellular composition[12]. The pancreas consists of four anatomical regions (head, neck, body and tail) and two functional systems. The exocrine system comprises ductal and acinar cells responsible for digestive enzyme secretion, while the endocrine system features the

islets of Langerhans containing specialized hormone-secreting cells (α, β, δ, and PP cells) that regulate glucose homeostasis. The figure also shows the anatomical relationship between the pancreas, bile duct and duodenum.

The pancreas demonstrates a complex organisational structure comprising two functionally distinct components: the endocrine and exocrine portions[11] (**Figure 1.1)**. The endocrine component accounts for approximately 2% of the total mass of the adult pancreas and consists of the islets of Langerhans[13]. These specialized structures contain four primary endocrine cell populations: A, B, D and F cells that produce glucagon, insulin, somatostatin, and pancreatic polypeptides respectively[14]. The exocrine portion constitutes approximately 80% of the mass of the pancreas and is composed of acinar and ductal epithelial cells that are responsible for digestive enzyme production and secretion[15].

PDAC originates within the exocrine compartment of the pancreas and develops along a complex pathway through distinct precursor lesions[16]. These precursor lesions encompass three primary categories (**Figure 1.2**): pancreatic intraepithelial neoplasia (PanIN), intraductal papillary mucinous neoplasia (IPMN), and mucinous cystic neoplasia (MCN)[17]. While traditional perspectives attributed PDAC origin exclusively to ductal cells, contemporary research utilizing genetically engineered mouse models has revealed a more complex etiology[18]. Indeed, these studies have demonstrated that acinar cells can also serve as a cellular origin for PDAC development, suggesting a broader spectrum of initiating events in pancreatic carcinogenesis[19].

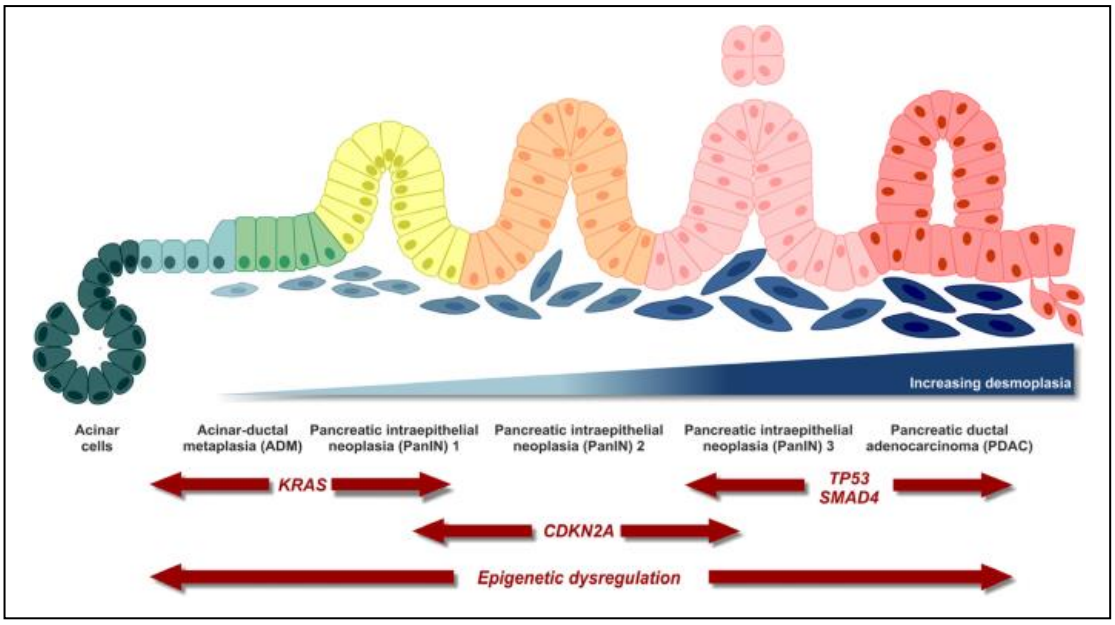

Figure 1.2. Schematic representation of pancreatic ductal adenocarcinoma (PDAC) progression and associated molecular alterations[20]. The progression from normal acinar cells to PDAC involves a stepwise transformation through acinar-ductal metaplasia (ADM) and pancreatic intraepithelial neoplasia (PanIN 1-3) stages. This process is accompanied by increasing desmoplasia and characterised by specific genetic alterations, including KRAS mutations in early stages, CDKN2A inactivation in intermediate stages, and TP53/SMAD4 mutations in late stages. Epigenetic dysregulation occurs throughout the entire progression sequence.

The molecular pathogenesis of PDAC is characterised by a sequence of genetic alterations[21]. The most frequent and critical mutations occur in four key driver genes namely *KRAS*, *CDKN2A, TP53*, and *SMAD4* (**Figure 1.2**) that regulate fundamental cellular processes[21,22]. Over 90% of PDAC cases have mutations in *KRAS* (Kristen rat sarcoma viral oncogene homolog) which lead to constitutive activation of proliferative signalling pathways and serve as an initiating event in PDAC development[23]. About 95% of PDAC cases have mutations in *CDKN2A* (cyclin dependent kinase inhibitor 2A) which encodes p16, a critical cell cycle regulator that prevents uncontrolled cell division. Inactivating mutations in *CDKN2A* thus removes an essential checkpoint in cell cycle control[21]. Approximately 75% of PDAC cases have mutations in *TP53* (tumour protein 53) which is known as the guardian of the genome[21]. TP53 plays a crucial role in maintaining genomic stability and regulating cell cycle checkpoints and

mutations in *TP53* compromises the DNA damage response and apoptotic mechanisms[21]. *SMAD4* (SMAD family member 4) loss due to deletions or mutations occurs in roughly 55% of PDAC cases. It functions as a central mediator of the transforming growth factor beta (TGF-β) signalling pathway and loss of SMAD4 disrupts this pathway's tumour-suppressive functions and promotes metastatic progression[24].

1.1.2. Clinical Pathology, Management and Treatment of PDAC

The treatment of PDAC primarily depends on the stage of the disease, with surgical resection and chemotherapy serving as the cornerstone of clinical management[25]. The disease can be staged by histological examination or imaging. Histological grading assesses tumour differentiation from well to poorly differentiated states. While well-differentiated tumours maintain normal ductal cell features and suggest better prognosis, poorly differentiated tumours exhibit marked cellular abnormalities and typically indicate more aggressive disease progression[26]. The diagnosis of PDAC also relies on comprehensive clinical evaluation by advanced imaging techniques such as Computed Tomography (CT) and Magnetic Resonance Imaging (MRI), and tissue biopsy[25]. Therapeutic strategies are based on the TNM staging system which refers to the primary tumour size and local invasion (T stage), regional lymph node involvement (N stage), and the presence of distant metastasis (M stage)[27] (**Table 1.1** and **Figure 1.3**).

Table 1.1. TNM classification and stage grouping system for pancreatic cancer[28]. The staging system comprises primary tumour (T) characteristics based on size and local invasion, regional lymph node involvement (N) status, and presence of distant metastases (M). The stage grouping integrates TNM categories to define prognostically distinct disease stages (0-IV).

Category	Code	Description
Primary Tumor (T)	Tx	Tumor cannot be assessed
	T0	No evidence of primary tumor
	Tis	Carcinoma in situ
	T1	Tumor ≤2 cm in greatest dimension
	T1a	Tumor ≤0.5 cm in greatest dimension
	T1b	Tumor >0.5 cm and <1 cm in greatest dimension
	T1c	Tumor 1-2 cm in greatest dimension
	T2	Tumor >2 cm but ≤4 cm in greatest dimension
	T3	Tumor >4 cm in greatest dimension
	T4	Involvement of celiac axis, superior mesenteric artery, and/or common hepatic artery
Regional Lymph Nodes (N)	Nx	Nodes cannot be assessed
	N0	No evidence of nodal involvement
	N1	1-3 regional node metastases present
	N2	4 or more regional node metastases present
Metastases (M)	Mx	Presence of metastases cannot be assessed
	M0	No evidence of metastases
	M1	Distant metastases present
Stage Groupings	Stage 0	Tis N0 M0
	Stage Ia	T1 N0 M0
	Stage Ib	T2 N0 M0
	Stage IIa	T3 N0 M0
	Stage IIb	T1, T2, or T3 with N1 M0
	Stage III	N2 M0 with any T, or T4 with any N M0
	Stage IV	M1 with any T and N

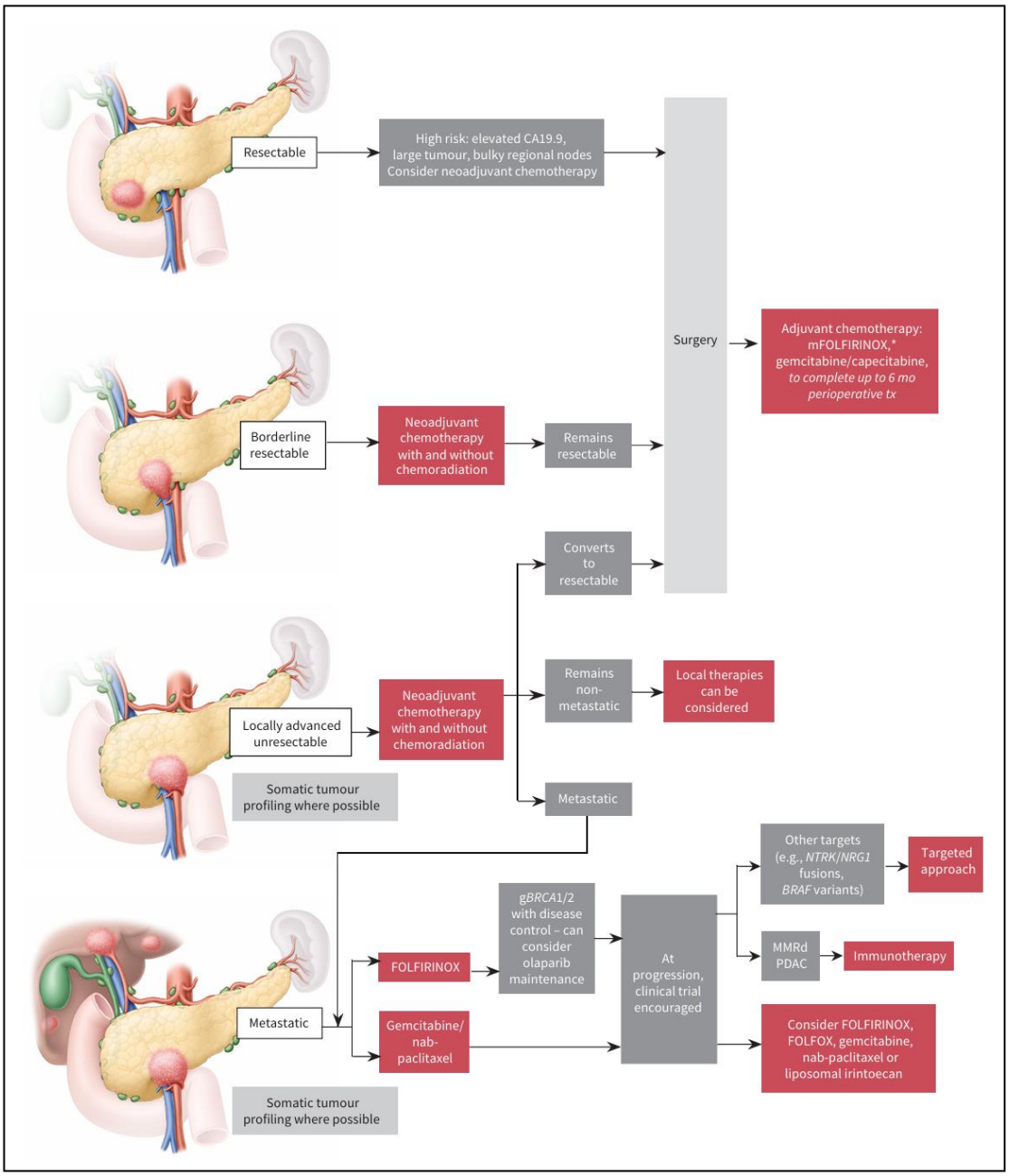

Figure 1.3. Treatment algorithm for pancreatic cancer based on resectability status and disease stage[29]**.** The algorithm illustrates therapeutic strategies for four distinct clinical scenarios: resectable, borderline resectable, locally advanced unresectable, and metastatic disease. Treatment pathways incorporate neoadjuvant therapy, surgical intervention, adjuvant chemotherapy, and targeted approaches based on molecular profiling. For metastatic disease, the algorithm includes first-line treatment options and subsequent therapeutic considerations at disease progression, including clinical trials and biomarker-directed therapies.

For early-stage PDAC (stage I/II: T1-3, N0-1, M0, **Table 1.1**), the primary goal is to achieve a complete, margin-negative (R0) surgical resection, as residual microscopic disease significantly reduces patient survival[30]. Surgeons typically perform a pancreatoduodenectomy (Whipple procedure) for tumours in the pancreatic head and a distal pancreatectomy with splenectomy for lesions in the body or tail of the pancreas[31]. Adjuvant chemotherapy, often with modified FOLFIRINOX (a combination regimen of fluorouracil, irinotecan, leucovorin, and oxaliplatin), follows surgery to eradicate any potential micrometastatic disease[32] (**Figure 1.3**). This multi-drug regimen has demonstrated superior survival outcomes with median overall survival (OS) of 54.4 months compared to 35 months with traditional gemcitabine therapy (hazard ratio 0.64, P = 0.003)[32]. This strategy exploits the post-surgical vulnerability of residual cancer cells and leverages the synergistic effects of combination chemotherapy to induce DNA damage, disrupt microtubule function, and inhibit key metabolic pathways, thereby reducing recurrence risk[33].

Stage III PDAC (T4, any N, M0, **Table 1.1**), encompassing borderline resectable and locally advanced tumours, presents unique challenges that require a nuanced approach. This involves neoadjuvant therapies such as FOLFIRINOX or gemcitabine/nab-paclitaxel which aim to shrink tumours in order to increase the likelihood of an R0 resection, and to address systemic disease earlier in the treatment course[32] (**Figure 1.3**). This preoperative strategy not only reduces tumour burden but also provides an *in vivo* assessment of tumour biology, with responsive tumours suggesting a more favourable prognosis[32].

For metastatic PDAC (stage IV, **Table 1.1**), systemic therapy becomes the central focus since curative surgery is not typically an option[33]. Treatment decisions in this setting depend on patient performance status and the molecular characteristics of the tumour. FOLFIRINOX remains a potent first-line option for fit patients due to its multi-agent mechanism targeting various cancer cell processes[32] (**Figure 1.3**). In cases where

patients cannot tolerate this regimen, alternatives such as gemcitabine combined with nab-paclitaxel or newer combinations like NALIRIFOX (a combination regimen of liposomal irinotecan, oxaliplatin, leucovorin, and fluorouracil) are employed[34]. These regimens not only disrupt tumour cell division but also modify the tumour stroma—a dense, fibrotic barrier that hinders drug delivery[35]. Nab-paclitaxel, in particular, enhances the intratumoural delivery of gemcitabine by altering the stroma and increasing vascular permeability, thereby overcoming one of the key mechanisms of chemoresistance[36].

Despite significant advances in understanding and treating PDAC, several fundamental challenges continue to hamper progress in improving patient outcomes. The deep anatomical location of the pancreas means that early-stage tumours rarely cause noticeable symptoms, and when symptoms appear, they often indicate advanced disease[37]. Treatment resistance presents another significant hurdle. This stems from multiple factors including the dense fibrotic tissue (desmoplasia) that characterises the tumour microenvironment, which not only impedes drug delivery but also creates a hypoxic environment promoting cancer cell survival and drug resistance[37]. It is worth noting that immuno- and targeted therapies for PDAC are emerging as promising approaches to address these challenges. For example, chimeric antigen receptor T-cell (CAR-T) therapy aims to overcome these barriers by engineering patient T-cells to recognize and attack tumour-specific antigens[38]. Furthermore, targeted therapy aims to overcome treatment resistance but to date, the poly-ADP ribose polymerase (PARP) inhibitor, Olaparib, is one of the few approved targeted agents used to treat PDAC[39]. Olaparib exploits genetic vulnerabilities in PDAC tumours, particularly those with BRCA1/2 mutations, by blocking DNA repair pathways and inducing synthetic lethality[40]. It is clear that there is a need to identify additional drug targets for PDAC and therefore the elucidation of the key molecules that drive this disease is important. In this regard, this thesis is interested in the T-box transcription factor 2, TBX2, because

it is significantly overexpressed in PDAC tissues [41]. Importantly, the overexpression of TBX2 in a number of other cancers is crucial for their malignant phenotypes and it has consequently been identified as an attractive therapeutic target for developing novel therapies for these cancers[42].

1.2. TBX2

TBX2 belongs to the highly conserved T-box family of transcription factors that all share a sequence-specific DNA-binding domain, called the T-box[43]. The T-box family is divided into 5 subfamilies (T, TBX1, TBX2, TBX6 and TBr1), with 17 T-box genes identified in humans. TBX2 specifically belongs to the TBX2 subfamily, which includes TBX3, TBX4 and TBX5[42]. T-box factors bind their target genes at a full palindromic sequence, [TTT(G/C)ACACCTAGGTGTGAAA], referred to as the T-element, but can also recognize and bind the half-sites, GGTCTGA, GGGTGA, or GTGTTA[43]. T-box transcription factors function as either transcriptional activators or repressors to regulate their target genes[44]. Some T-box factors are however capable of both activating and repressing target genes which is, in part, dependent on protein partners that they interact with in different contexts[43]. While TBX2 plays critical roles during embryonic development, its dysregulation in adult tissues has been implicated in multiple diseases, including cancer, where it functions as a potent oncogene[42,45].

1.2.1. Molecular Structure and Function of TBX2

TBX2 is located on chromosome 17q23, spans 9.53 kb, contains 7 exons, and encodes a 712 amino acid protein[46] (**Figure 1.4**). The TBX2 protein possesses several functionally distinct domains that together enable its complex regulatory functions. These include the T-box DNA-binding domain, two repression domains (R1 at the N-terminus and R2 at the C-terminus), and an activation domain embedded within the T-

box region[42,47]. The T-box domain spans approximately 200 amino acids and while it primarily recognizes the consensus sequence TCACACCT, known as the T-element, recent studies have revealed that TBX2 is also able to bind its target genes at other DNA sequences such as E-box motifs[48–50]. TBX2 can function as both a transcriptional activator and repressor, and chromatin immunoprecipitation sequencing (ChIP-seq) studies demonstrated that its repressive functions typically involve T-element binding while its activating functions often utilize E-box motifs[50].

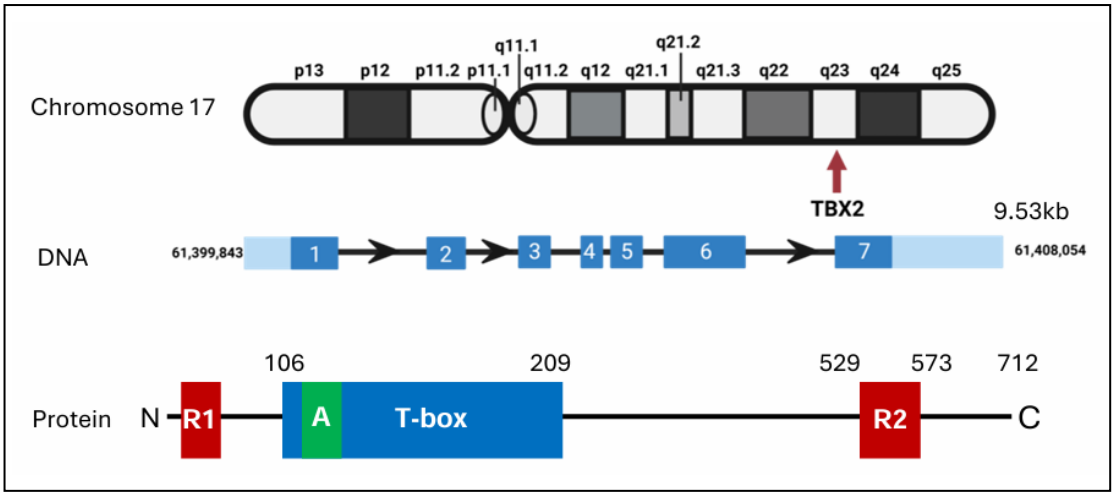

Figure 1.4. Genomic organisation and protein domain structure of human TBX2. The figure shows the chromosomal location of TBX2 on chromosome 17q23, spanning approximately 9.53kb of genomic DNA. The gene structure consists of 7 exons (numbered 1-7, blue boxes). The encoded protein (712 amino acids) contains characteristic functional domains including two repression domains (R1 and R2, red), an activation domain (A, green), and a conserved DNA-binding T-box domain (blue). Numbers indicate amino acid positions within the protein sequence.

TBX2 engages in numerous protein-protein interactions that are crucial for its regulatory functions. Biochemical studies have demonstrated that the N-terminal domain contains multiple phosphorylation sites and protein interaction motifs that facilitate these interactions[45]. For example, the amino acid region 1-53 has been shown to be critical for histone deacetylase 1 (HDAC1) binding, which enhances the transcriptional repression capabilities of TBX2[51]. Additionally, TBX2 interacts with and requires early growth response 1 (EGR1) to inhibit the tumour suppressor genes

such as N-myc downstream regulated 1 (*NDRG1)* and cysteine protease inhibitor cystatin 6 (*CST6)* that are involved in cell cycle control and differentiation[52,53].

1.2.2. TBX2 in Embryonic Development

During embryonic development, TBX2 exhibits precise temporal and spatial expression patterns that orchestrate the formation of multiple organ systems[54]. In cardiac development, TBX2 guides atrioventricular canal formation through repression of chamber-specific genes (*Nppa*, *Mycn* and *Cx40*), ensuring proper cardiac compartmentalization[55]. The protein's influence extends to limb development, where it interacts with Bone morphogenetic protein (BMP) signalling pathways to control digit patterning and identity[56]. Within the mammary gland, TBX2 directs ductal morphogenesis and branching through complex molecular interactions[57]. TBX2 also plays a crucial role in neural development, influencing the migration and differentiation of neural crest cells[58,59].

The critical importance of TBX2 in the above developmental processes has been clearly demonstrated in mice and human. Mouse studies have provided compelling evidence that proper TBX2 dosage is critical for its functions. Indeed, while heterozygous *Tbx2* mutant mice appear normal, homozygous mutants die of severe cardiac malformations including defective atrioventricular canal formation and pericardial oedma[60]. Although TBX2 has not yet been directly linked to any specific human genetic syndrome, TBX2 variants have been identified in patients displaying an overlapping spectrum of developmental defects. These include cardiac abnormalities (atrial septal defects, double outlet right ventricle), craniofacial defects (cleft palate, facial dysmorphisms), skeletal malformations (vertebral fusion, camptodactyly), and other developmental defects like thymic hypoplasia and growth abnormalities[59,61].

1.2.3. TBX2 in Cancer

TBX2 exhibits elevated expression in multiple cancer types, including carcinomas of the breast, ovaries, stomach, pancreas, lung, prostate, colon, oesophagus, nasopharynx, brain, and endometrium, as well as melanomas and specific sarcoma variants such as malignant peripheral nerve sheath tumours (MPNSTs) and rhabdomyosarcomas[62–80]. The increased expression of TBX2 correlates with advanced clinical stages and poor patient survival outcomes, and contributes to several cancer hallmarks including enhanced cellular proliferation, increased migration, metastasis formation, cell death resistance, and reduced therapeutic sensitivity[68,71]. Importantly, depleting TBX2 in cancers addicted to it inhibits key cancer phenotypes which positions it as an attractive therapeutic target[62,69,75].

Uncontrolled proliferation represents a fundamental hallmark of cancer as cells acquire the ability to bypass critical cell cycle checkpoints that serve as cancer prevention barriers[81]. This involves the downregulation of tumour suppressor genes to evade growth suppression or bypass senescence and resistance to apoptotic cell death[81]. TBX2 functions as a powerful proliferative and anti-senescence factor through its ability to transcriptionally repress key tumour suppressor genes[62,82,83]. Initial studies by Jacobs and colleagues[83] demonstrated that TBX2 overexpression promotes immortalization of Bmi-null- primary mouse embryo fibroblasts through *Cdkn2a* ($p19^{ARF}$) repression and delaying the onset of senescence[83]. Similarly, elevated TBX2 expression has been documented in melanoma, where it contributes to unlimited replicative potential through the suppression of senescence and promotion of cell cycle progression[82]. This is achieved through TBX2 repressing $p21^{Cip1/Waf1}$ via HDAC1 recruitment to the *CDKN1A* initiator[51,82]. This mechanism extends to rhabdomyosarcoma (RMS), where TBX2 recruits HDAC1 to repress myogenic regulatory factors (MyoD and myogenin) and multiple tumour suppressors ($p21^{Cip1/Waf1}$, $p14^{ARF}$ and *PTEN*), resulting in myogenic differentiation inhibition and proliferation promotion[79,84]. Studies in nasopharyngeal

cancer have demonstrated that TBX2 expression shows a negative correlation with several tumour suppressors including PTEN, $p21^{Cip1}$, $p27^{Kip1}$, and the epithelial marker E-cadherin[75]. Furthermore, when TBX2 expression is silenced, these tumour suppressors become upregulated, resulting in decreased cancer cell proliferation and reduced invasive capacity[75].

Epithelial-mesenchymal transition (EMT) represents a critical biological process during which epithelial cells acquire mesenchymal characteristics, enabling cancer cells to gain invasive and migratory capabilities[85]. The EMT process involves molecular alterations including adherent junction loss, cytokeratin and E-cadherin downregulation, and increased N-cadherin and β-catenin expression[85]. TBX2 functions as a crucial regulator of EMT, thereby facilitating tumour metastasis and progression across multiple cancer types[62,65,71,72,75]. In breast cancer, TBX2 drives EMT through direct repression of E-cadherin and activation of mesenchymal markers including N-cadherin and vimentin[62]. This process is further enhanced by TBX2's ability to activate the WNT3A signalling pathway, which promotes the expression of matrix metalloproteinases MMP2 and MMP9, facilitating cancer cell invasion and metastasis[70,72]. The role of TBX2 in metastasis is further supported by its ability to interact with neurotrophin receptor-interacting MAGE homolog (NRAGE) to repress $p14^{ARF}$ to confer resistance to anoikis, a form of programmed cell death triggered by detachment from the extracellular matrix, thereby enabling cancer cell survival during the metastatic process[86].

Accumulating evidence has implicated TBX2 in tumour drug resistance, particularly in response to conventional chemotherapeutics[87]. In breast cancer, TBX2 confers cisplatin resistance through a mechanism involving activation of checkpoint kinase 2 (CHK2), which ensures p53 phosphorylation and stability[87,88]. This enhances p53's transcriptional activation of p21, leading to S-phase cell cycle arrest that allows time for DNA damage repair and cancer cell survival[87]. Importantly, reducing TBX2 levels

in cisplatin-resistant breast cancer cells leads to mitotic catastrophe and restored drug sensitivity[87]. In endometrial carcinoma, TBX2 promotes cisplatin resistance through a distinct mechanism involving the regulation of ferroptosis, a form of regulated cell death[78,89]. This is achieved through TBX2's transcriptional upregulation of the nuclear factor erythroid 2-related factor 2 (NRF2) and enhancement of ferroptosis suppressor protein 1 (FSP1) expression[78,89]. In ovarian cancer, TBX2 overexpression strongly correlates with platinum resistance, and its suppression can restore sensitivity to these agents[64]. Similarly, in glioblastoma, TBX2 contributes to temozolomide resistance by modulating mitochondrial dynamics and apoptotic pathways[76]. The involvement of TBX2 in drug resistance extends to targeted therapies. In prostate cancer, TBX2 has been implicated in resistance to androgen deprivation therapy through its effects on chromatin regulation and cell survival pathways[90]. In rhabdomyosarcoma, TBX2 promotes resistance to actinomycin D, etoposide, and vincristine through its ability to inhibit the expression of EGR1-dependent cell cycle regulators and pro-apoptotic target genes[80].

1.2.4. TBX2 in PDAC

The dysregulation and clinical relevance of TBX2 has also been reported in PDAC. Indeed, immunohistochemical analysis of 48 patient samples revealed that TBX2 was strongly expressed in 60.4% of PDAC cases (**Table 1.2**), while no equivalent expression was observed in normal pancreatic tissues[41]. Notably, high-level TBX2 expression correlated with poor tumour differentiation, advanced TNM staging, and distant metastasis[41] (**Table 1.3**). Semiquantitative reverse transcription polymerase chain reaction (RT-PCR) and western blot analyses further confirmed increased TBX2 mRNA and protein levels in PDAC tissues[41]. Together, these data suggest that TBX2 may play an important role in the development, invasion, and malignant potential of PDAC and that it may be a novel therapeutic target for this highly lethal cancer.

Table 1.2. Differential expression of Tbx2 in pancreatic cancer versus non-cancer tissue[41]. Expression levels were evaluated across different stages (I-IV) in 48 pancreatic cancer specimens and 12 non-cancer tissue samples.

Tissue Type	Total Cases	Tbx2 Expression I II III IV	Positive Cases	Percentage	p-value
Non-cancer tissue	12	0, 0, 0, 0	0	0%	0.049
Pancreatic cancer	48	9, 10, 18, 11	29	60.4%	

Table 1.3. Association of Tbx2 expression with clinicopathological features in pancreatic cancer[41]. Tbx2 expression was analysed across different clinicopathological parameters including tumour differentiation (well/moderate/poor), TNM stage (early/advanced), and metastatic status.

Category	Group	Total Cases	Positive Cases	Percentage	p-value
Differentiation	Well	14	5	35.7%	0.015
	Moderate	15	8	53.3%	
	Poor	19	16	84.2%	
TNM Stage	I, II (Early)	27	13	48.1%	0.049
	III, IV (Advanced)	21	16	76.2%	
Metastasis	No	30	14	46.7%	0.012
	Yes	18	15	83.3%	

As a strategy to identify drugs that target TBX2, the Prince laboratory in South Africa established a collaboration with Prof Costa-Lotufo's laboratory in Brazil. The Costa-Lotufo laboratory has established a functional chromatography system which allows them to screen for new natural molecules of marine origin with anticancer activity and interact with TBX2. In this screen, Chromomycin A5 (CA5) was identified to have strong binding affinity for TBX2, and the current thesis examines the anticancer activity of CA5 in PDAC and whether this occurs through targeting TBX2[91].

1.3. Chromomycin A Compounds

Chromomycins are a group of antibiotics isolated from Streptomyces, which demonstrate remarkable anticancer activities through multiple mechanisms[91,92]. Their basic structure consists of a tricyclic skeleton with multiple glycosylated side chains which contribute to their ability to bind DNA and disrupt transcriptional processes[93]. The Chromomycin family includes Chromomycin A2 (CA2), A3 (CA3), A4 (CA4), A5 (CA5) , A6 (CA6), A7 (CA7) and A8 (CA8)[91,92,94–96] (**Figure 1.5**). Among these, CA2 and CA5 share the same molecular formula but differ in their optical rotation due to distinct spatial configurations, making them enantiomers. Similarly, CA3 and CA6 are enantiomers. The glycosylated moieties, particularly 2,6-dideoxy sugars, play a crucial role in their interaction with DNA by facilitating the formation of stable 2:1 complexes with Mg^{2+} in GC-rich DNA regions[92].

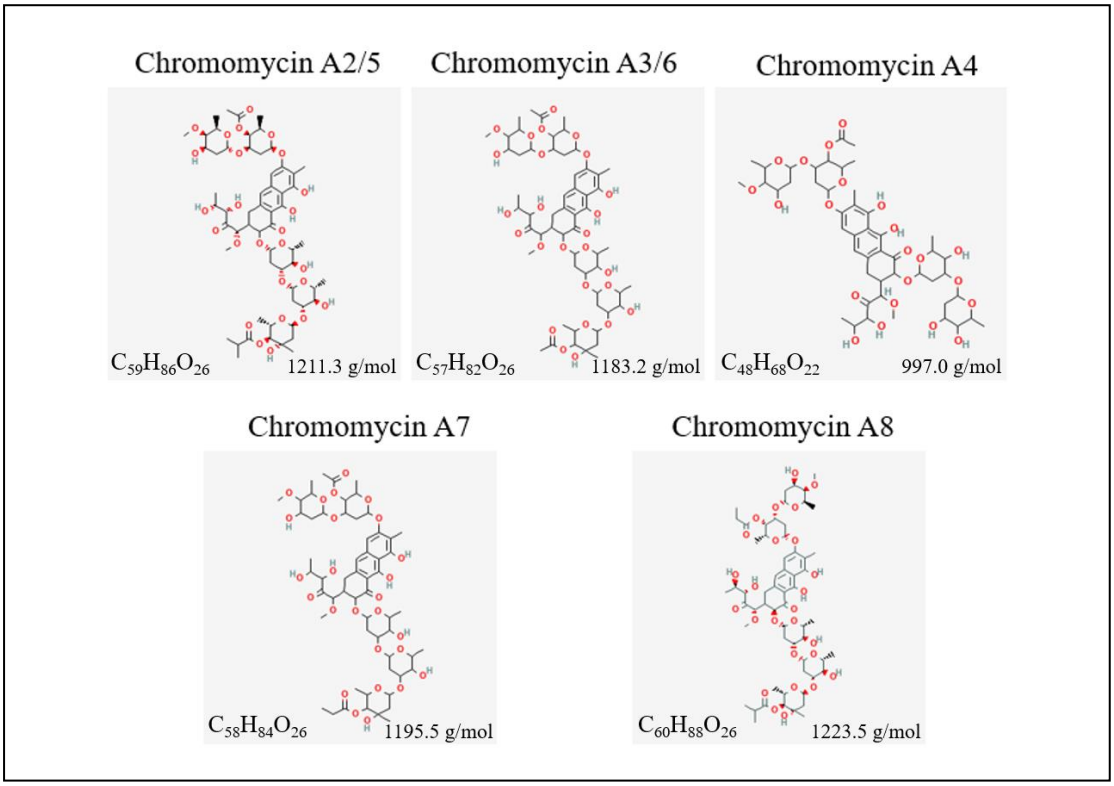

Figure 1.5. Chemical structures of chromomycin A family members[97]. The figure displays the molecular structures of five chromomycin A analogs (A2, A3, A4, A5, A6, A7, and A8). These compounds share a common aglycon core structure but differ in

their glycosylation patterns and substituent groups, which contribute to their distinct biological activities. The structural variations among these analogs, particularly in their sugar moieties and functional groups.

1.3.1. Anticancer Activity of Chromomycin A compounds

The anticancer effects of Chromomycin A compounds primarily arise from their ability to bind DNA and inhibit transcription processes. CA3 has been showed to reversibly bind to the minor groove of DNA, forming a stable 2:1 complex with Mg^{2+} in CG-rich DNA regions[92]. This binding disrupts essential processes such as DNA replication and transcription, effectively targeting rapidly dividing cancer cells[92].

CA2 and CA3 demonstrate potent cytotoxicity against human gastric adenocarcinoma cells (AGS cell line), with IC_{50} values of 1.7 nM and 22.1 nM, respectively[95]. This activity was attributed to inhibition of the TCF/β-catenin transcriptional activity which was demonstrated in human embryonic kidney STF/293 cells[90]. Indeed, CA3 was less effective in cells containing mutated TCF-binding sites compared to those have wild type β-catenin signalling pathway[90]. In addition, CA3 was shown to overcome tumour necrosis factor (TNF)-related apoptosis-inducing ligand (TRAIL) resistance in gastric adenocarcinoma cells[90]. This dual action on transcription and apoptosis pathways underscores its therapeutic potential[95]. In MALME-3M metastatic melanoma cells, CA2 is more cytotoxic than CA3, with IC_{50} values of 16.7 nM and 762 nM respectively [98]. Additionally, CA2 induced autophagy in the MALME-3M melanoma cells as was evidenced by increased LC3-II, autophagosome accumulation, and the formation of acidic vesicular organelles[98]. However, whether the autophagy induced by CA2 conferred cell death or survival was not investigated. Among the Chromomycins, CA3 is the only family member with a published X-ray crystal structure (**Figure 1.6**), providing crucial insights into its orientation within the minor groove and highlighting the structural basis for the anticancer activity of this compound class. CA4 shares structural similarities with CA3 but its β-sugar unit is substituted with an isobutyryl

group, which increases steric hindrance and weakens its ability to bind to the DNA minor groove[96]. Due to its reduced bioactivity, no further studies were pursued following its discovery. **Figure 6. Crystal Structure of Chromomycin A3-Mg^{2+} Complex Bound to DNA[99].** The figure shows the three-dimensional structure of chromomycin A3 (gray stick model) bound to double-stranded DNA (shown in orange and green ribbons) through Mg^{2+}-mediated coordination.

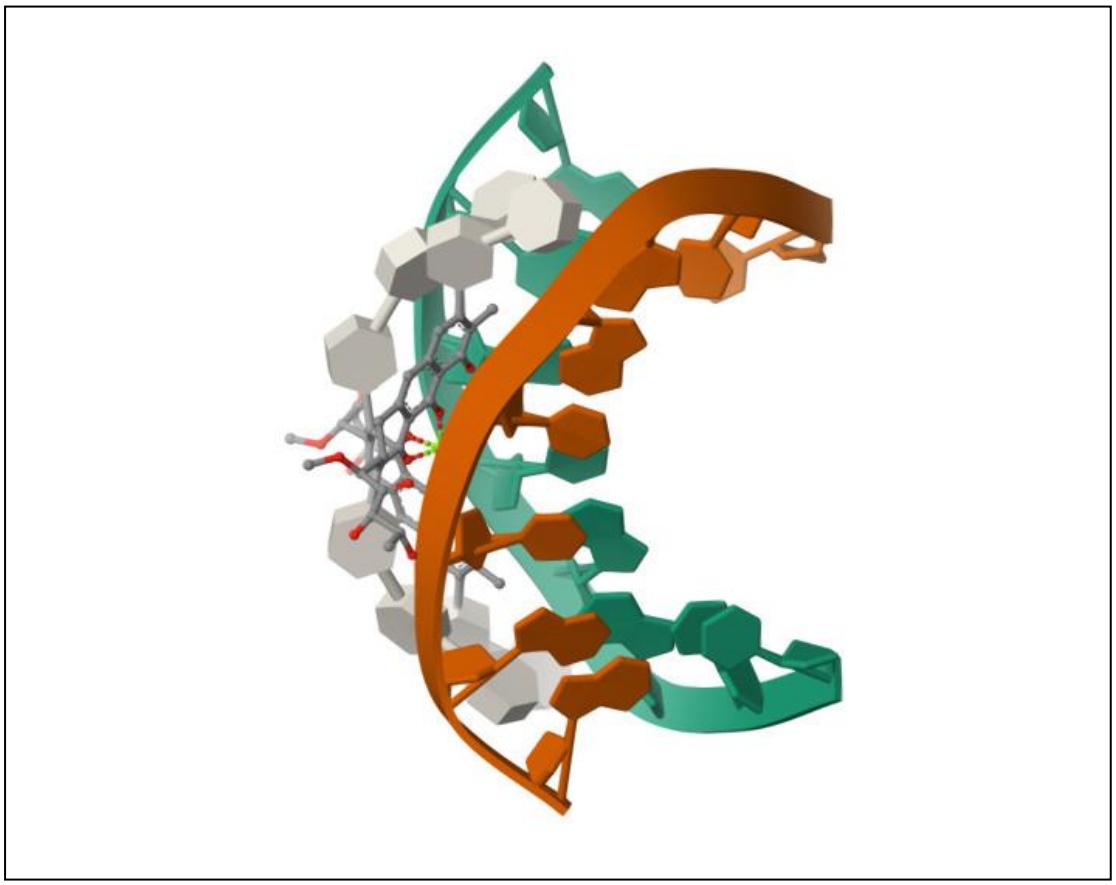

Figure 1.6. Crystal Structure of Chromomycin A3-Mg^{2+} Complex Bound to DNA[99]. The figure shows the three-dimensional structure of chromomycin A3 (gray stick model) bound to double-stranded DNA (shown in orange and green ribbons) through Mg^{2+}-mediated coordination.

Of the Chromomycin A family members, CA5 appears to be the most effective at inducing cytotoxicity at low concentrations across a variety of cancer cell lines including melanoma, breast, rhabdomyosarcoma, colon, prostate, pancreatic, lung and central nervous system[91,94,100] (**Table 1.4**). The cytotoxicity of CA5 is attributed to its

Table 1.4. IC_{50} Values of CA5 Across Multiple Cancer Types and Cell Lines[91,94,100]. Multiple entries for the same cell line (e.g., 501-mel, MCF-7, MM200) represent IC_{50} values characterised in independent experimental studies.

Cancer Type	Cell Line	IC_{50} Value (nM)
Melanoma	501-mel	0.8
		0.8
	WM293A	0.3
	MM200	0.5
		0.2
Breast Cancer	MCF-7	3.7
		2.1
		0.73
	T47D	6.5
Rhabdomyosarcoma	RD	3
	RH30	3.5
Colon Cancer	KM20L2	4.3
	HCT 116	0.4
Prostate Carcinoma	PC-3M	7.9
	DU-145	1.9
Pancreatic Cancer	BXPC-3	2.4
Lung Cancer	NCI-H460	1.4
Central Nervous System Cancer	SF-268	2.1

potential DNA minor-groove binding ability and its ability to interact with oncogenic transcription factors such as TBX2 to disrupt their ability to regulate their target genes[91]. Reverse-affinity chromatography confirmed that CA5 binds directly to the TBX2 DNA-binding domain, with a dissociation constant (k_D) in the micromolar range, which was validated by microscale thermophoresis[91]. The cytotoxic effects of CA5 were evaluated in TBX2-expressing cell lines, including melanoma, breast carcinoma, and rhabdomyosarcoma[91]. Notably, CA5 demonstrated nanomolar IC_{50} values, with melanoma cells (especially MM200 and 501MEL) showing the highest sensitivity, as

indicated by the lower IC_{50} values and relative low levels of TBX2[91]. In 501MEL melanoma cells, knockdown of TBX2 increased sensitivity to CA5, confirming that its cytotoxicity is at least partially mediated through TBX2 targeting[91]. Conversely, inducible expression of TBX2 reduced the sensitivity of melanoma cells to CA5, further supporting the above finding[91].

In addition, CA5 induces immunogenic cell death (ICD), a mechanism that stimulates antitumour immunity through the release of damage-associated molecular patterns (DAMPs) such as adenosine triphosphate (ATP), calreticulin (CRT), and high-mobility group box 1 (HMGB1)[101]. These DAMPs activate antigen-presenting cells and promote T-cell-mediated immunity, which enhances the systemic antitumour response. *In vivo* studies demonstrated that vaccination with CA5-treated melanoma cells significantly delayed tumour growth in a syngeneic mouse model[101]. Like CA5, CA6 was identified as a potent DNA-binding compound with significant binding affinity to TBX2[91,94]. However, in general, CA5 had lower IC_{50} values than CA6 across various tumour cell lines which suggests that it is more cytotoxic than CA6. For example, CA5 and CA6 exerted IC_{50} values of 0.5 nM and 4.2 nM in MM200 melanoma cells respectively[91]; and 3.7 nM and 10.5 nM in MCF-7 breast cancer cells respectively[94].

CA8 has a structure similar to CA5 and CA6 and inhibits RNA synthesis by binding to the DNA minor groove[94]. However, its cytotoxicity is considerably weaker compared to CA5[94]. For example, CA5 and CA8 have IC_{50} values of 0.1 nM and 0.8 nM in MM200 melanoma cells, respectively, 7.9 nM and 88.3 nM in PC-3M prostate cancer cells, respectively, 0.4 nM and 1.4 nM in HCT116 colon carcinoma, respectively, and finally 3.7 nM and 10.5 nM in MCF-7 breast cancer cells, respectively[94]. It is worth noting that CA7 exhibits even lower cytotoxicity than CA8[94]. Indeed, in MM200 melanoma cells, CA7 has an IC_{50} of 39.1 nM, and in MCF-7 breast cancer cells, its IC_{50} reaches 133.0 nM[94]. These data suggest that CA7, despite being structurally related to other active members, has substantially weaker antitumour effects[94]. Given that CA4,

CA7, and CA8 exhibit inferior tumour growth inhibition compared to other members of the aureolic acid family, such as CA3 and CA5, research on these compounds has remained limited, and they show little potential for further development as anticancer agents.

1.4. Aims of this study

PDAC remains one of the most lethal malignancies, with a dismal 5-year survival rate of 13%. Despite advances in understanding its molecular pathogenesis, effective therapeutic strategies are still lacking. Over past decades, the medical field has steadily pursued novel therapeutic approaches; however, patient outcomes have shown little improvement. Consequently, a thorough understanding of PDAC's molecular basis, along with the identification of new therapeutic targets, is crucial for enhancing patient prognoses. While the T-box transcription factor, TBX2, has been reported to correlate with PDAC metastasis and poor prognosis, its functional role in PDAC progression remains to be elucidated. CA5, a promising anticancer compound which has been recently identified to bind and inhibit TBX2, has shown potent cytotoxicity against several TBX2-dependent cancers. However, its efficacy and molecular mechanisms in PDAC have not been investigated. Therefore, the aims of this study are:

1. To elucidate the role of TBX2 in PDAC progression and its potential as a therapeutic target.
2. To evaluate the anticancer activity and underlying molecular mechanisms of CA5 in PDAC.

CHAPTER 2
Methodology

2.1. Cell Culture

Cell culture is based on providing an *in vitro* system that mimics the *in vivo* environment for cells, allowing them to survive, proliferate, and maintain their physiological functions under controlled and reproducible conditions[102]. This study utilized the human PDAC cell lines SW1990 and CFPAC-1. The SW1990 cells, derived from spleen metastasis, display typical epithelial cell characteristics and possess wild-type TP53 along with mutations in the KRAS oncogene and CDK2A and SMAD4 tumour suppressor genes[103]. The CFPAC-1 cells, originated from liver metastasis, harbor a distinct genetic profile including mutations in KRAS, TP53, and SMAD4[104]. The CFPAC-1 cell line serves as a valuable model for investigating the relationship between pancreatic cystic fibrosis and PDAC[104].

The PDAC cells SW1990 (ATCC, USA), PANC-1 (ATCC, USA), CFPAC-1 (gift from Dr. L. Zerbini, University of Cape Town), BxPC-3 (gift from Dr. L. Zerbini, University of Cape Town), and the human skin fibroblasts, FG0 (gift from Prof. D. Hendricks, University of Cape Town) were cultured in Roswell Park Memorial Institute (RPMI) 1640, Iscove's Modified Dulbecco's Medium (IMDM), and Dulbecco's Modified Eagle Medium (DMEM), respectively (all from Gibco, USA). The media were supplemented with 10% fetal bovine serum (FBS) and 1% penicillin/ streptomycin (Gibco, USA). Cells were maintained at 37°C, 5% CO_2, saturated humidity in various culture vessels (96-well to 6-well plates, 6-15 cm dishes; Corning, USA).

At 80-90% confluence, cells were washed with phosphate buffered saline (PBS) (pH 7.4: 137 mM NaCl, 2.7 mM KCl, 10 mM Na_2HPO_4, 1.8 mM KH_2PO_4), trypsinised (0.25% Trypsin-EDTA, Gibco, USA, 3-5 minutes), neutralized with 2-3 volumes medium, centrifuged (300×g, 5 minutes), and reseeded 1:3 to 1:5. Medium was changed every 2-3 days. For cryopreservation, cells were frozen in medium with 10% FBS and 10% dimethyl sulfoxide (DMSO), stored in liquid nitrogen, and revived by rapid thawing at 37°C with medium change within 24 hours.

2.1.1. Mycoplasma Detection

Only mycoplasma negative cells were used in this study. To test for mycoplasma, cells were trypsinised and seeded onto anhydrous ethanol-treated coverslips (Corning, USA) in 35 mm culture dishes with 2 mL antibiotic-free DMEM + 10% FBS. Following overnight incubation at 37°C, cells were fixed using 1 mL fixative solution (25% glacial acetic acid from Sigma-Aldrich, USA, 75% methanol from Merck, Germany) twice for 10 seconds, followed by three rinses with distilled water. Air-dried coverslips were stained with Hoechst 33342 (5 µg/mL in PBS; Thermo Fisher Scientific, USA) for 5-10 seconds, rinsed thrice with distilled water, and mounted cell-side down onto glass slides (Lasec, South Africa) with mounting medium (20 mM citric acid, 55 mM $Na_2HPO_4 \cdot 2H_2O$, 50% glycerol, pH 5.5; all from Sigma-Aldrich, USA). Slides were examined using the DAPI channel of a EVOS M5000 Imaging System (Thermo Fisher Scientific, USA), with mycoplasma-positive samples showing star-like distributed small nuclei around cell nuclei, while negative samples displayed only clear blue cell nuclei.

2.2. Cell Transfection

2.2.1. siRNA Transfection

The principle of small interfering RNA (siRNA) transfection is based on the RNA interference (RNAi) mechanism[105], which involves specific mRNA degradation guided by double-stranded RNA, thereby inhibiting the expression of the target gene (**Figure 2.1**). In cells, siRNA is processed into small fragments by the Dicer enzyme and binds to the RNA-induced silencing complex (RISC). RISC uses the complementarity of the siRNA sequence to guide its binding to the target mRNA, leading to the cleavage and degradation of the mRNA, thus inhibiting the translation of that gene. To improve transfection efficiency and specificity, cationic liposomes such as Hiperfect® transfection reagent are commonly used to deliver siRNA into cells[106]. The gene silencing effect after transfection usually peaks 48-72 hours post-transfection and is suitable for studying gene function and its role in cellular physiological processes[106].

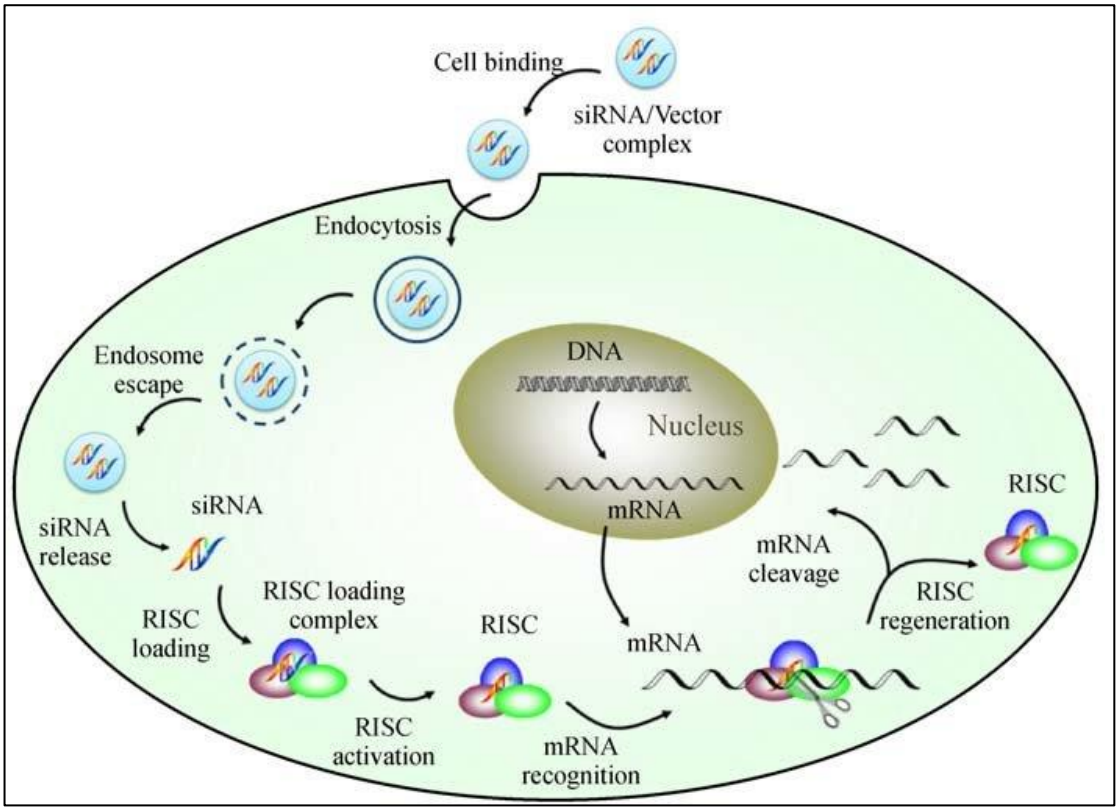

Figure 2.1. Schematic illustration of the cellular siRNA delivery and RNA interference mechanism[105]**.** The diagram depicts the sequential steps of siRNA-mediated gene silencing, from initial cell binding of the siRNA/vector complex through endocytosis, endosomal escape, and RISC-mediated target mRNA degradation. Key processes include cellular uptake, siRNA release, RISC complex formation, target mRNA recognition, cleavage, and RISC regeneration, demonstrating the complete cycle of RNAi-based gene silencing.

In this study, SW1990 cells (1×10^5/well) were seeded in 12-well plates and grown to 70-80% confluency after which they were transfected with TBX2 siRNAs (#1 [ACAGCTGAAGATCGACAACAA] and #2 [TGGGACGTGTACAGCACAGAA]) or negative control siRNA [AATTCTCCGAACGTGTCACGT] (all from Qiagen, USA). siRNAs were diluted to 20 nM in 100 µL serum-free, antibiotic-free medium, mixed with 3 µL Hiperfect® transfection reagent (Qiagen, USA), and incubated for 10 minutes at room temperature. Transfection complexes were added dropwise to cells with gentle agitation and cultured for 48-72 hours.

2.2.2. Establishment of Inducible Expression Cell Lines

The principle of establishing inducible expression cell lines is based on stable transfection and controllable expression of exogenous genes. Using the PiggyBac (PB) transposon system, exogenous genes, such as TBX2, can be stably and efficiently integrated into [TTAA] chromosomal sites of the host cell genome via transposase (**Figure 2.2A**)[107]. This system enables transfection of large DNA cargo (up to 200 kb) and minimizes insertional mutagenesis compared to traditional transfection methods, as DNA repair enzymes restore genomic integrity without leaving transposon footprints. The PB transposase recognizes specific inverted terminal repeat sequences (ITRs) flanking the gene of interest, excises the genetic cargo, and precisely integrates it into the host genome at [TTAA] sites, ensuring stable inheritance during cell division.

During the establishment of the cell line, the selection process relies on the neomycin resistance gene (Neo) carried by the vector, allowing only successfully transfected cells to survive under antibiotic pressure. The successfully transfected cells are selected by adding G418 (geneticin), an analogue of neomycin. The induction expression system (rtTA-Tet-On) employs a reverse tetracycline-controlled transactivator (rtTA) that allows researchers to control TBX2 expression under the tetracycline-inducible human cytomegalovirus (hCMV1) promoter by adding tetracycline derivatives, such as Doxycycline[108]. In this binary system, rtTA proteins bind to tetracycline response elements (TREs) in the presence of doxycycline, activating transcription from the minimal CMV promoter (**Figure 2.2B**). The absence of doxycycline prevents rtTA binding, maintaining tight transcriptional control with minimal leaky expression[108]. This system provides precise temporal and dose-dependent control, making it ideal for

studying time-dependent gene functions and their dynamic effects on cell signalling pathways.

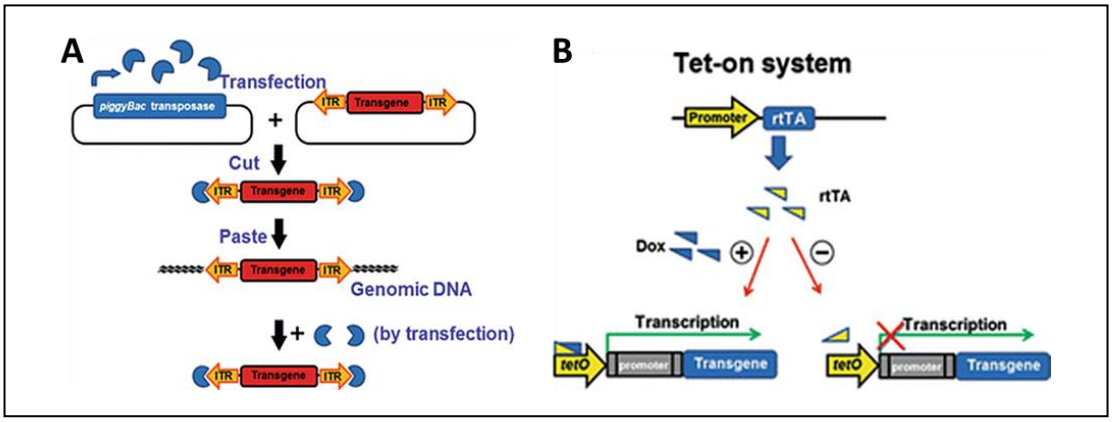

Figure 2.2. Schematic representation of PiggyBac transposon-based inducible gene expression system[108]. The figure illustrates two key components: (A) PiggyBac transposition mechanism for stable genomic integration of transgenes at [TTAA] sites, facilitated by transposase-mediated cut-and-paste process. (B) Doxycycline-inducible Tet-On system showing rtTA-dependent transcriptional regulation, where doxycycline presence (+) enables transgene expression while its absence (-) maintains transcriptional silence.

To establish a PDAC cell culture model with inducible TBX2 overexpression, SW1990 cells were first treated with G418 (100-1000 μg/mL, Sigma-Aldrich, USA) for 10 days to determine optimal selection concentration. For stable transfection, cells (5×10^5/well) in 6-well plates were transfected at 70% confluency with pPB-hCMV1-cHApA-TBX2-3xFLAG or pPB-hCMV1-cHApA-Empty-3xFLAG, pPB-CAG-rtTA-INeo, and pPyCAG-PBase plasmids (gift from Professor Colin Goding from Ludwig Institute of Cancer Research, Oxford University, United Kingdom), 500:500:50 ng, using FuGENE HD (Promega, USA, 3 μL in 100 μL total volume) , as a transfection reagent. After 48 hours, cells were transferred into 10 cm dishes and treated with G418 (400 μg/mL). Single colonies were isolated after 10-14 days using petroleum jelly-sealed cloning rings, trypsinised, and expanded in 24-well plates. Stable clones were verified by 24-hour Doxycycline (10 μg/mL, Sigma-Aldrich, USA) induction followed by western blotting detection of TBX2-Flag expression.

2.3. PCR

Polymerase chain reaction (PCR) is a molecular biology technique for amplifying specific DNA sequences[109]. Using specific primers and thermostable DNA polymerase, PCR can amplify specific DNA fragments millions of times *in vitro*. The process consist of several steps, such as RNA extraction, reverse transcription PCR (RT-PCR) and quantitative real-time PCR (qRT-PCR).

2.3.1. RNA Extraction

In this study, total RNA was extracted from cells under experimental conditions (1×10^6) using Trizol reagent (Invitrogen, USA). Briefly, cells were lysed in 1 mL Trizol for 5 minutes, mixed with 0.2 mL chloroform (Sigma-Aldrich, USA), and centrifuged (12,000 g, 4°C, 15 minutes). The aqueous phase was precipitated with an equal volume of isopropanol (Sigma-Aldrich, USA) for 10 minutes, centrifuged (12,000 g, 4°C, 10 minutes), washed with 75% ethanol (Merck, Germany), and centrifuged again (7,500 g, 4°C, 5 minutes). Air-dried RNA pellets were resuspended in 30-50 µL RNase-free water (Invitrogen, USA) and quantified using a NanoDrop 1000 spectrophotometer (Thermo Scientific, USA).

2.3.2. RT-PCR

Reverse transcription PCR (RT-PCR) includes two steps: first, RNA is reverse transcribed into complementary DNA (cDNA) by reverse transcriptase, and then specific cDNA sequences are amplified using conventional PCR[110].

First-strand cDNA was synthesized using ImProm-II™ Reverse Transcription System (Promega, USA). RNA mixture (1 µg RNA, 1 µL Oligo(dT)15 primer in 5 µL total volume) was denatured at 70°C for 5 minutes, ice-cooled, then combined with 15 µL reaction mixture (4 µL 5X buffer, 2.4 µL MgCl2 [25 mM], 1 µL dNTP Mix [10 mM

each], 0.5 µL RNasin® Inhibitor, 1 µL reverse transcriptase, 6.1 µL RNase-free water [Invitrogen, USA]). Reactions were performed in a Bio-Rad thermocycler: 25°C/5 min, 42°C/60 min, 70°C/15 min. cDNA was stored at -20°C.

2.3.3. qRT-PCR

Quantitative real-time PCR (qRT-PCR) combines RT-PCR and fluorescent dye technology, enabling real-time monitoring of PCR product accumulation, thereby achieving accurate quantification of gene expression (**Figure 2.3**)[111]. SYBR Green is a fluorescent dye that emits a strong fluorescent signal when bound to double-stranded DNA[112]. qRT-PCR measures the intensity of the fluorescent signal in each PCR cycle, plots an amplification curve, and calculates the initial template amount of the target gene. Using the $2^{-\Delta\Delta Ct}$ method, the relative expression level of the target gene can be quantitatively analysed with respect to the reference gene[113]. Due to its high sensitivity and specificity, qRT-PCR has become an important tool for studying gene expression and regulation.

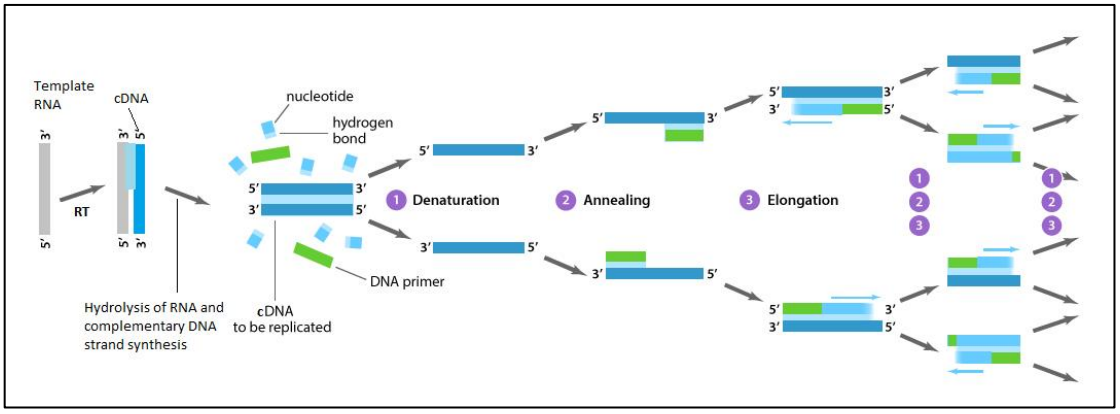

Figure 2.3. Schematic diagram of quantitative Reverse Transcription PCR (qRT-PCR)[111]. qRT-PCR includes the three main steps: denaturation, annealing, and elongation, preceded by cDNA synthesis from template RNA.

qRT-PCR was performed using Power SYBR™ Green PCR Master Mix (Applied Biosystems, USA) on a StepOne Real-Time PCR System with commercial primers Hs_GUSB_1_SG, and Hs_TBX3_1_SG (QIAGEN), and custom primers (IDT) for

TBX2 (F-GATCCCCACAGCTGAAGATCGACAAC, R-AGCTTAAAAATCAGCTG AAGATCGAC), p21 (F-GGCCAGCTGAGGTGTGAGCAGCTGCC, R-CGGCAGC TGCTCACACCTCAGCTGGC), CST6 (F-GCAACAGCATCTACTACT TC, R-AGTCTGTGCTCCCCATCTCC), and NDRG1 (F-CCTACCGCCAGCACATT GTGA, R-TTCATCAATGCCTACAACAGCCG). Reactions (20 μL) contained 10 μL master mix, 0.5 μL each primer (10 μM), 1 μL cDNA (1000 μg/μL), and 8 μL RNase-free water, with cycling conditions: 95°C/10 min; 40 cycles of 95°C/15 s, 60°C/60 s; melting curve 60-95°C (0.3°C increments). Data were analysed using $2^{-\Delta\Delta Ct}$ method, and GUSB as a housekeeping gene.

2.4. Western Blotting

Western blotting is a molecular biology technique used to detect and quantify specific proteins (**Figure 2.4**)[114]. The technique involves protein extraction and separation by Sodium dodecyl sulphate-polyacrylamide gel electrophoresis (SDS-PAGE) based on molecular weight, followed by transfer to a membrane. Specific proteins are then detected using antibodies and visualised through chemiluminescent or colourimetric methods[115].

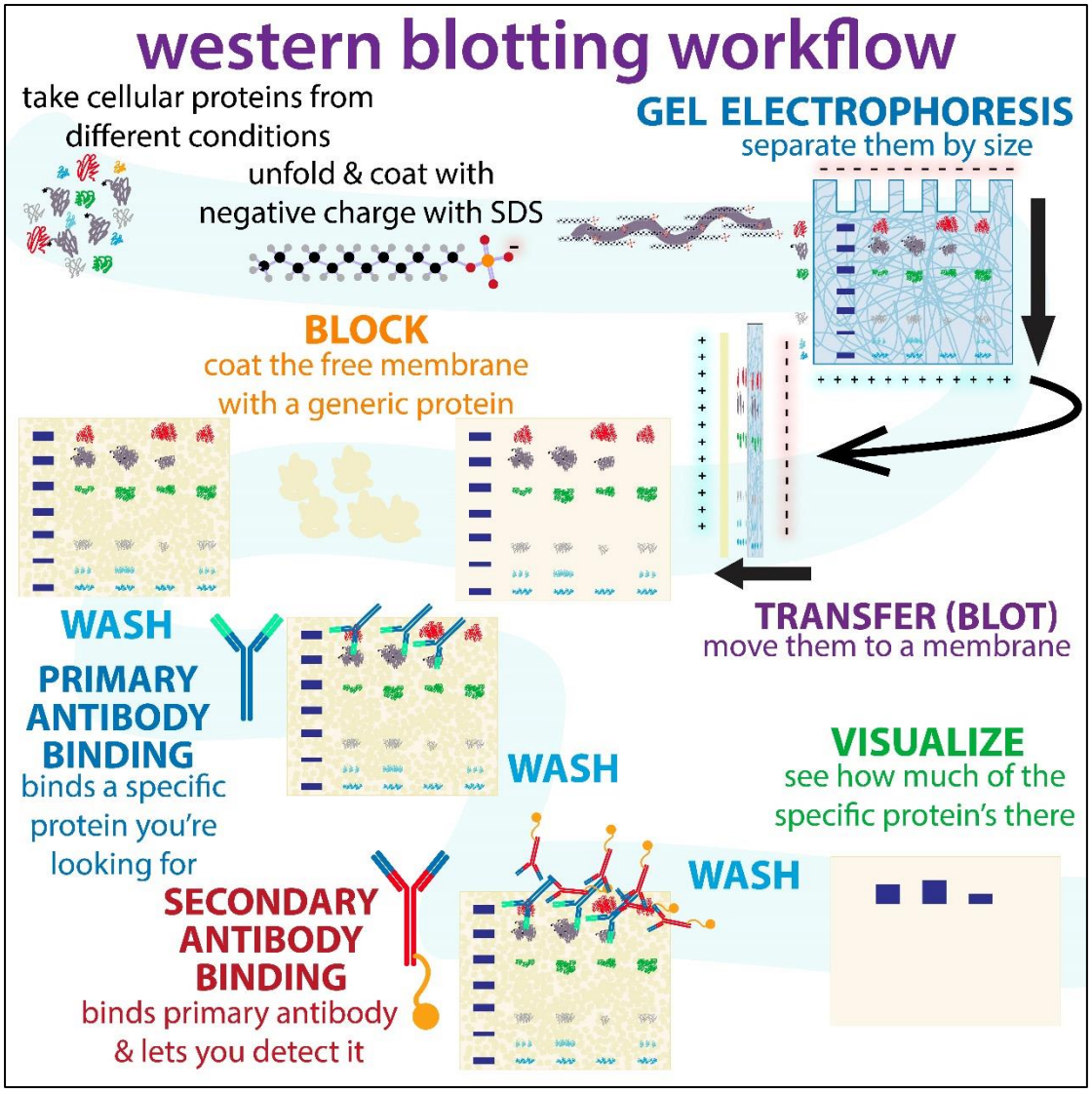

Figure 2.4. Sequential Process of Western Blotting to Detect and Analyse Specific Proteins[114]**.** The diagram depicts the step-by-step workflow of Western blotting, proceeding from initial protein extraction through SDS treatment, gel electrophoresis for size separation, protein transfer to membrane, blocking, primary and secondary antibody binding, and final protein visualization, illustrating the complete experimental protocol for protein detection and analysis.

2.4.1. Protein Sample Preparation

Cell pellets were washed with PBS, centrifuged (300×g, 2 minutes), and lysed in Laemmli buffer (375 mM Tris-HCl pH 6.8, 9% SDS, 50% glycerol, 9% β-mercaptoethanol, 0.03% bromophenol blue, all from Sigma-Aldrich, USA). Samples were boiled at 90-100°C for 10 minutes in pierced tubes and stored at -20°C.

2.4.2. SDS-PAGE Gel Preparation

Separating and stacking gels were prepared using 40% acrylamide/bisacrylamide, 1.5 M Tris-HCl (pH 8.8 or 6.8), 10% sodium dodecyl sulphate (SDS), 10% ammonium persulphate (APS), and tetramethylethylenediamine (TEMED) (all from Sigma-Aldrich, USA) in Bio-Rad gel equipment. Separating gel (vary from 8-15%) was overlaid with isopropanol until polymerization was complete, then rinsed with distilled water (Millipore, USA), before being topped with 5% stacking gel. A stacking gel comb was used to create the wells in which the proteins were loaded.

2.4.3. SDS-PAGE Electrophoresis

SDS-PAGE was performed using Bio-Rad Mini-PROTEAN Tetra Cell (Bio-Rad, USA). Samples (20-50 µL) and PageRuler™ ladder (Thermo Fisher, USA, 5 µL) were separated at 100V for 90-120 minutes using running buffer (25 mM Tris, 192 mM glycine, 0.1% SDS, pH 8.3).

2.4.4. Protein Transfer

Proteins were transferred to nitrocellulose membranes (0.45 µm, Advansta, USA) using transfer buffer (25 mM Tris, 192 mM glycine, 20% methanol, pH 8.3) by either semi-dry (Bio-Rad, USA, Trans-Blot SD, 25V/2.5A, 20 minutes) or wet transfer (Bio-Rad, USA, Mini Trans-Blot, 100V, 80-100 minutes at 4°C) methods, with sandwich assembly (anode-filter paper-membrane-gel-filter paper-cathode).

2.4.5. Immunoblotting and Development

Membranes were blocked with 5% skim milk (Merck, Germany) in Tris buffered saline with Tween (TBST) (20 mM Tris, 150 mM NaCl, 0.1% Tween-20, pH 7.5) for 0.5h at room temperature on a shaker, followed by overnight 4°C incubation on a shaker with

primary antibodies. The primary antibodies used were: TBX2 (1:500, sc-514291, Santa Cruz, USA), TBX3 (1:1000, MAH858Hu21, Cloud-Clone, USA), Flag-M2 (1:4000, SLCM4081, Merck, Germany), p-AKT(S473) (1:1000, 9271S, Cell Signaling Technology, USA), CDK2 (1:1000, sc-136191, Santa Cruz, USA), Cyclin A (1:1000, sc-271682, Santa Cruz, USA), Cyclin B1 (1:1000, 4135S, Cell Signaling Technology, USA), E-cadherin (1:1000, 14472S, Cell Signaling Technology, USA), N-cadherin (1:1000, 14215S, Cell Signaling Technology, USA), Vimentin (1:1000, 5741S, Cell Signaling Technology, USA), β-catenin (1:1000, 8480S, Cell Signaling Technology, USA), PARP (1:1000, 9542S, Cell Signaling Technology, USA), Caspase-8 (1:1000, 9746S, Cell Signaling Technology, USA), Caspase-3 (1:1000, 9662S, Cell Signaling Technology, USA), Cleaved Caspase-7 (1:1000, 8438S, Cell Signaling Technology, USA), Caspase-9 (1:1000, 9502S, Cell Signaling Technology, USA), P-Histone H2A.X (1:2000, 2577S, Cell Signaling Technology, USA), β-actin (1:4000, sc-47778, Santa Cruz, USA). After TBST washes (3×10min), membranes were incubated with horseradish peroxidase- (HRP-) conjugated anti-mouse or anti-rabbit secondary antibodies (1:5000, 1706516/1706515, Bio-Rad, USA) for 1h at room temperature, washed again (3×10min TBST), and developed using WesternBright ECL (Advansta, USA) on a ChemiDoc MP imaging system (Bio-Rad, USA). Band intensities were quantified using Fiji software[116] and normalized to β-actin.

2.5. Cell Proliferation Assay

Cell proliferation was assessed by direct cell counting using a Neubauer improved haemocytometer (Marienfeld, Germany) and CKX53 microscope (Olympus, Japan). Cells (5×10^4/well) were seeded in triplicate in 12-well plates. For collection, cells were washed with PBS, trypsinised with 0.5 mL 0.25% Trypsin-EDTA (3-5 minutes, 37°C), and neutralized with equal volume of complete medium. Cell counts were performed by adding 10 µL of cell suspension in the counting chamber, counting four corner

squares, and calculating cells/mL using the formula: average count × 10^4 × dilution factor. Results were normalized to control group cell numbers to obtain relative proliferation rates.

2.6. Invasion and Migration Assay

Invasion and migration assays are used to assess the invasive and migratory ability of cells under specific conditions and are commonly used to study the molecular mechanisms related to cancer metastasis.

2.6.1. Transwell Assay

The principle of the transwell migration assay is based on the migration of cells from the upper chamber to the lower chamber through a membrane with pores, and this migration is usually driven by chemoattractants (**Figure 2.5**)[117].

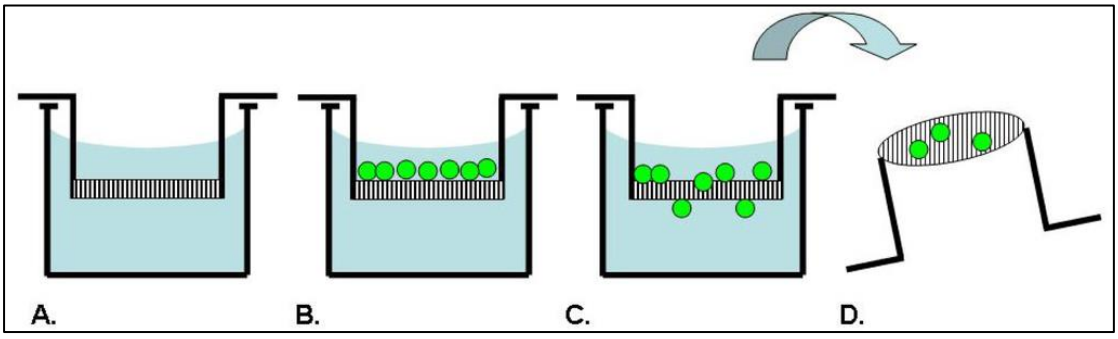

Figure 2.5. Schematic Overview of Transwell Migration Assay for Cell Motility Assessment[117]. The diagram illustrates the sequential steps of a Transwell assay, showing (A) the initial setup with two compartments separated by a porous membrane, (B) cell seeding in the upper chamber, (C) active cell migration through membrane pores, and (D) final analysis of migrated cells on the membrane's underside, demonstrating a standard method for quantifying cellular migration and invasion capabilities.

Cell invasion was assessed using Matrigel-coated transwell inserts (8 μm pore size, Corning, USA). Matrigel (Corning, USA) was thawed overnight at 4°C, diluted to 0.3

mg/mL in serum-free medium, applied to inserts (200 µL/well), and solidified overnight at 37°C. Cells were trypsinised, resuspended in 1% FBS medium (1×10^5 cells/mL), and seeded (2×10^4 cells/200 µL) in upper chambers, with 500 µL 10% FBS medium in lower chambers. After 24h at 37°C, non-invaded cells were removed using cotton swabs (Puritan), and invaded cells were PBS-washed, crystal violet-stained (0.1%, 30 minutes, Sigma-Aldrich, USA), and imaged using an EVOS microscope (Thermo Fisher Scientific, USA). Invasion was detected using the Segment Anything Model (SAM)[118] for mask generation (source code: https://github.com/baijinming97/detection.git). To quantify the invasion, the stained area was calculated by the pixel count ratio (purple pixels/total pixels).

2.6.2. Scratch Wound Healing Assay

Scratch wound healing assay (wound healing assay) is based on creating an artificial "scratch" or "wound" on a cell monolayer and observing how cells migrate to fill this gap (**Figure 2.6**)[117].

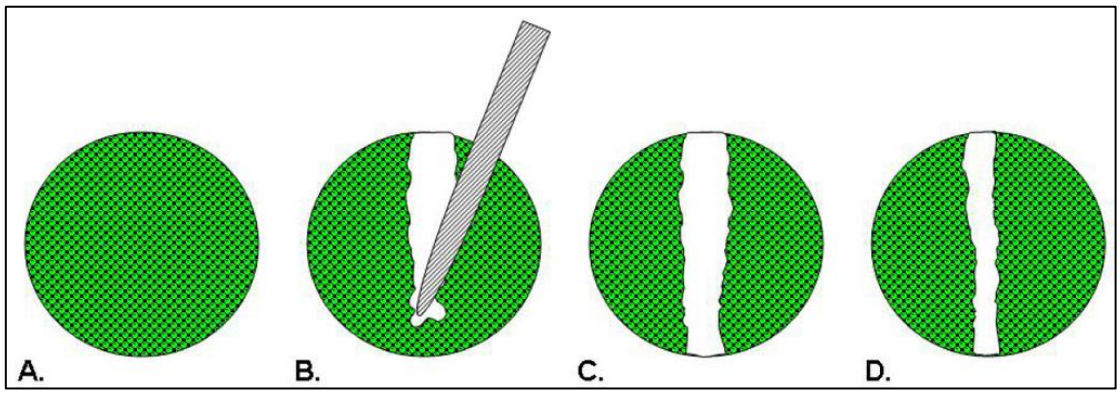

Figure 2.6. Schematic Demonstration of Wound Healing/Scratch Assay for Cell Migration Analysis[117]**.** The diagram shows the key steps of a scratch assay, including (A) initial confluent cell monolayer, (B) creation of an artificial wound using a pipette tip, (C) initial wound boundary measurement, and (D) assessment of cell migration through wound closure, representing a standard method to evaluate collective cell migration *in vitro*.

Cells were grown to 90-95% confluence in 12-well plates under experimental conditions (transfection or drug treatment), wounds were made using sterile white pipette tips (Corning, USA), washed twice with PBS, and maintained in serum-free medium. Wound areas were imaged at 0, 3, 6, 9, 12, and 24h using an EVOS microscope (Thermo Fisher Scientific, USA) with minimum three fields of view per well. Images were analysed using YOLOv10[119] for initial wound detection followed by SAM[118] for mask generation (source code: https://github.com/baijinming97/detection.git). Migration was quantified as (initial scratch area - current scratch area), normalized to 24h control group, with scratch area calculated as pixel count ratio (scratch pixels/total pixels).

2.7. MTT Assay

The MTT assay is based on mitochondrial enzyme-catalysed reactions, specifically using the dehydrogenases in the mitochondria of living cells to reduce the yellow tetrazolium salt MTT (3-(4,5-dimethylthiazol-2-yl)-2,5-diphenyltetrazolium bromide) to insoluble purple formazan crystals[120].

MTT (5 mg/mL in PBS, Sigma-Aldrich, USA) was filtered (0.22 μm, Millipore, USA) and stored at 4°C protected from light. Cells (3000-5000/well) were seeded in 96-well plates in quadruplicate, grown to 60% confluence, and treated with different concentration of Chromomycin A5 or Gemcitabine. After treatment, MTT solution (10 μL/well, final 0.5 mg/mL) was added and incubated for 4h at 37°C, 5% CO_2. Medium was then aspirated and formazan crystals were dissolved in DMSO (100 μL/well) by 30-minute shaking in the dark. Absorbance was measured at 600 nm using a GloMax reader (Promega, USA). Cell viability was calculated as (treatment Abs_{600nm} - blank Abs_{600nm})/(vehicle control Abs_{600nm} - blank Abs_{600nm}) × 100%.

The half-maximal inhibitory concentration (IC_{50}) was determined using nonlinear regression analysis with the "Inhibitor vs. response – Variable slope" model in GraphPad Prism 9.5 software[121]. The Selectivity Index (SI) was calculated using the formula:

$$SI(Selectivity\ Index) = \frac{IC_{50}(normal\ cell)}{IC_{50}(cancer\ cell)}$$

2.8. Clonogenic Assay

The colony formation assay evaluates the proliferative and survival abilities of individual cells by culturing them at low density, allowing each cell to grow into a visible colony.

Cells were treated with drugs for 24h, then trypsinised and seeded (1000 cells/well) in 6-well plates in drug free media. After 10-14 days culture at 37°C with medium changes every 3-4 days, colonies were fixed with methanol:glacial acetic acid (3:1, Merck, Germany/Sigma-Aldrich, USA) for 15 minutes, stained with 0.5% crystal violet (in methanol, Sigma-Aldrich, USA) for 15 minutes, and gently rinsed with tap water. Dried plates were photographed (OPPO Find X3), and colonies were quantified using Fiji software[116] threshold analysis. Results were expressed as relative colony area (treatment/control) after background subtraction.

2.9. Three-dimensional cell culture

Three-dimensional (3D) cell culture represents an advanced approach that better mimics the *in vivo* cellular microenvironment compared to traditional two-dimensional culture[122]. This method enables cells to grow and interact within a three-dimensional space, allowing for more physiologically relevant cell-cell and cell-matrix

interactions[122]. The 3D culture system supports the formation of complex structures such as spheroids, which better reflect native tissue architecture and cellular behavior[122]. This approach is particularly valuable for studying cellular organisation, drug responses, and disease mechanisms under conditions that more closely resemble the *in vivo* state[122].

2.9.1. Spheroid Formation Assay

Spheroids were generated on agarose-coated plates (1.2% in PBS, Sigma-Aldrich, USA) as shown in **Figure 2.7**. After UV sterilization (2h), cells (5000/well in 100 µL) were seeded in agarose-coated 96-well plates, cultured at 37°C with half-medium changes every 3 days. Spheroid growth was monitored every 48h using an EVOS microscope (Thermo Fisher Scientific, USA), with more than 3 spheroids per treatment group. Growth was quantified using SAM[118] for spheroid segmentation, calculating relative volumes (treatment/control area ratio).

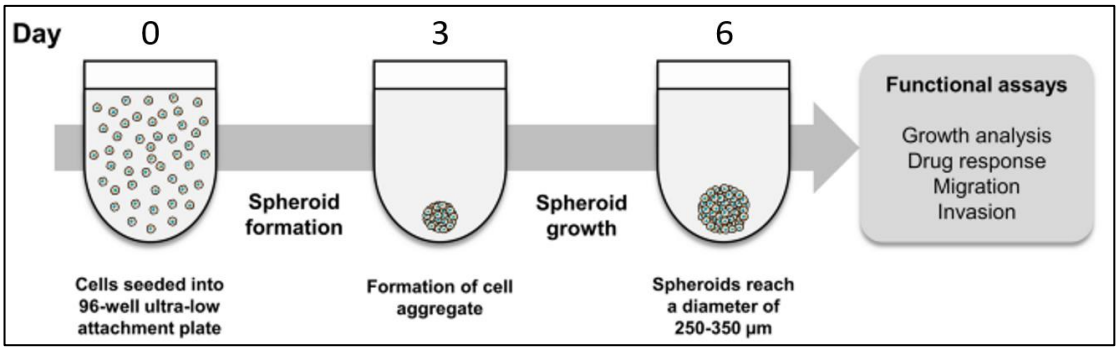

Figure 2.7. Timeline and Protocol for 3D Spheroid Generation and Functional Analysis[123]. The diagram outlines the temporal progression of spheroid development, from initial cell seeding in agarose-coated plates (Day 0), through aggregate formation (Day 3), to mature spheroids (Day 6) reaching 250-350 µm in diameter, followed by various downstream functional assays including growth analysis, drug response, migration, and invasion studies.

2.9.2. Calcein-AM/propidium iodide Staining

The triple staining method combines three fluorescent indicators to comprehensively assess cell viability and death in 3D cultures[124]. Calcein-AM, a cell-permeant dye, is

converted to fluorescent calcein by intracellular esterases in living cells, producing green fluorescence. propidium iodide (PI), unable to penetrate intact membranes, enters only dead cells with compromised membranes, binding to DNA to emit red fluorescence. Hoechst 33342, which readily permeates cell membranes and binds to DNA, provides nuclear visualization through blue fluorescence[124].

Spheroid viability was assessed using triple staining: Calcein-AM (2 mM stock in DMSO, Invitrogen), PI (1 mg/mL in PBS, Sigma-Aldrich, USA), and Hoechst 33342 (10 mg/mL in PBS, Thermo Fisher Scientific, USA). Working solution (2 μM Calcein-AM, 8 μg/mL PI, 10 μg/mL Hoechst 33342) were prepared in serum free media and was added 1:1 to 50 μL remaining medium and incubated 30 min at 37°C in the dark. Fluorescence (green/living, red/dead, blue/nuclei) was imaged using an EVOS microscope and quantified by Fiji software[116].

2.10. Immunofluorescence Staining

Immunofluorescence staining is based on the specific binding of antigens to antibodies and the detection of target antigen expression and localization by fluorescently labelled secondary antibodies (**Figure 2.8**)[125]. First, the target antigen in the sample binds to a specific primary antibody, followed by the introduction of a fluorescently labelled secondary antibody that binds to the primary antibody, allowing the distribution and expression level of the target protein to be observed under a fluorescence microscope through the fluorescent signal[126]. The fluorescence confocal microscope provides high-resolution images, enabling researchers to precisely analyse the expression of target proteins in different regions of the cell.

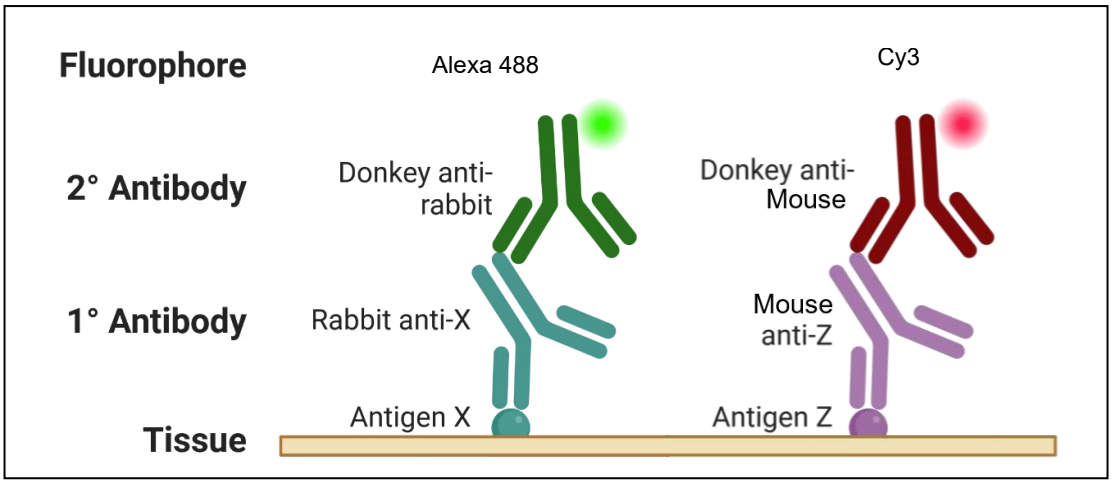

Figure 2.8. Schematic illustration of immunofluorescence labelling using primary and secondary antibodies for antigen detection in cells[125]**.** The diagram demonstrates the layered binding where primary antibodies specifically recognize cellular antigens, while fluorescently-labelled secondary antibodies bind to the primary antibodies, enabling visualization of target proteins.

Cells were seeded on sterilized 13 mm round coverslips (Thermo Fisher Scientific, USA) in 24-well plates (Corning, USA) and cultured to appropriate density. Cells were fixed with 4% paraformaldehyde (PFA) (Sigma-Aldrich, USA) for 15 minutes, permeabilized with 0.1% Triton X-100 (Sigma-Aldrich, USA) for 10 minutes, and blocked with 5% bovine serum albumin (BSA) (Sigma-Aldrich, USA) for 1 hour at room temperature. Primary antibodies (1:100 in 1% BSA) were applied overnight at 4°C in a Parafilm™ -lined humidified chamber, followed by fluorescent secondary antibodies (1:1000, Invitrogen, USA) plus Hoechst 33342 for 1 hour in the dark. Coverslips were mounted using Mowiol + triethylenediamine (DABCO) medium (Invitrogen, USA), and the secondary-only control was used to remove the background before imaging with a LSM 880 confocal microscope (Zeiss, Germany). Images were analysed using Fiji software[116] for fluorescence intensity.

2.11. Fluorescence Spectrum

After absorbing light energy, electrons in fluorescent molecules transition from the ground state to the excited state, and when the electrons return to the ground state, energy is released in the form of light, a process called fluorescence[127]. By measuring fluorescent molecules' excitation and emission spectra, their electronic states, molecular environment, and intermolecular interactions can be investigated. (**Figure 2.9**).

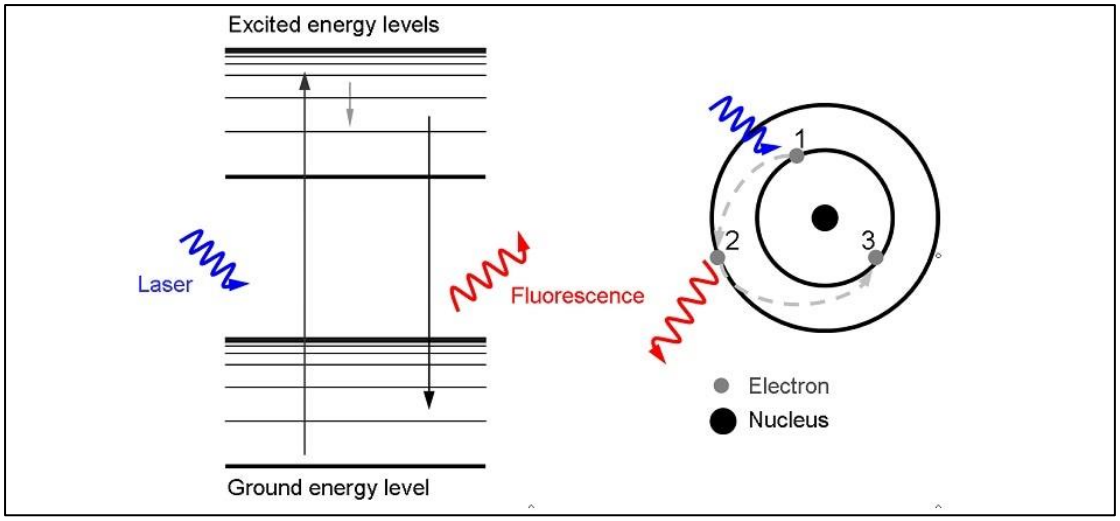

Figure 2.9. Principle of fluorescence emission through electronic state transitions[127]**.** The diagram illustrates both energy level transitions (left) and electron orbital changes (right) during fluorescence. Laser excitation (blue) promotes electrons from ground to excited states, followed by energy release through fluorescence emission (red) during the return to ground state. The orbital diagram shows the corresponding electron transitions (1), excitation state (2), and ground state (3).

2.11.1. CA5 Fluorescence Spectrum Measurement

Chromomycin A5 (CA5) is one such fluorescent molecule which is advantageous for studying its interaction with relevant biomolecules. However, the optimal excitation and emission wavelengths of CA5 were to be determined before investigating the interaction between CA5 and DNA. The measurement of its fluorescence spectrum

involves two main steps: first, determining the optimal excitation wavelength, i.e., measuring the fluorescence emission at different excitation wavelengths to find the excitation wavelength that can induce the strongest fluorescence intensity; and second, measuring the emission spectrum, i.e., recording the emission intensity at different wavelengths using the determined optimal excitation wavelength.

Chromomycin A5 (CA5, Santa Cruz, USA) was dissolved in DMSO (Sigma-Aldrich, USA) to 100 μM and analysed using a Cary Eclipse fluorescence spectrophotometer (Agilent, USA) in a quartz cuvette (Hellma, Germany). Excitation (200–500 nm) and emission (450–700 nm) wavelengths were systematically scanned, yielding discrete fluorescence intensity data at each wavelength pair. These data were imported into Python, where SciPy's Clough–Tocher 2D interpolator precisely fitted the original measurements to construct a smooth, continuous intensity surface. A uniform grid spanning the scanned wavelengths was generated, the interpolator evaluated intensities on this grid, and the resulting continuous matrix was visualised as a heat map using Matplotlib's imshow, providing a detailed representation of CA5's fluorescence behaviour.

2.11.2. CA5 and DNA-binding Measurement

The binding between DNA molecules and fluorescent molecules like CA5 affects the electronic properties of the compound, thereby changing its fluorescent behaviour. During the measurement, the concentration of CA5 remains constant, and the concentration of DNA is gradually increased. The fluorescence emission spectra at different DNA concentrations are measured, and changes in CA5 fluorescence intensity can be observed as DNA concentration increases. By analysing the relationship between fluorescence intensity and DNA concentration, the binding affinity and binding mode of CA5 to DNA can be inferred. This measurement method is commonly used to study DNA-drug interactions and the fluorescent labelling properties of drugs.

pCMV-TBX2-Flag plasmid DNA (1 mg/mL in DMSO) was serially diluted (5-30 μg/mL) and background fluorescence was measured at 410 nm excitation (emission: 450-700 nm). DNA solutions were mixed with CA5 (100 μM) and incubated for 5 minutes in the dark. Fluorescence spectra were recorded (excitation: 410 nm, emission: 450-700 nm) using a Cary Eclipse fluorescence spectrophotometer (Agilent, USA). Binding was analysed through relative fluorescence intensity changes versus DNA concentration.

2.12. Flow Cytometry Analysis

Flow cytometry is based on the light scattering and fluorescence signals generated by the interaction of a laser with single cells or particles passing through the laser beam in a flowing fluid stream[128]. These signals can be detected by photodetectors and converted into electronic signals to analyse the physical and chemical properties of cells (**Figure 2.10**)[128]. Flow cytometry can rapidly analyse thousands to millions of cells, providing important information about cell size, granularity, protein expression levels, and other cellular biological characteristics[128].

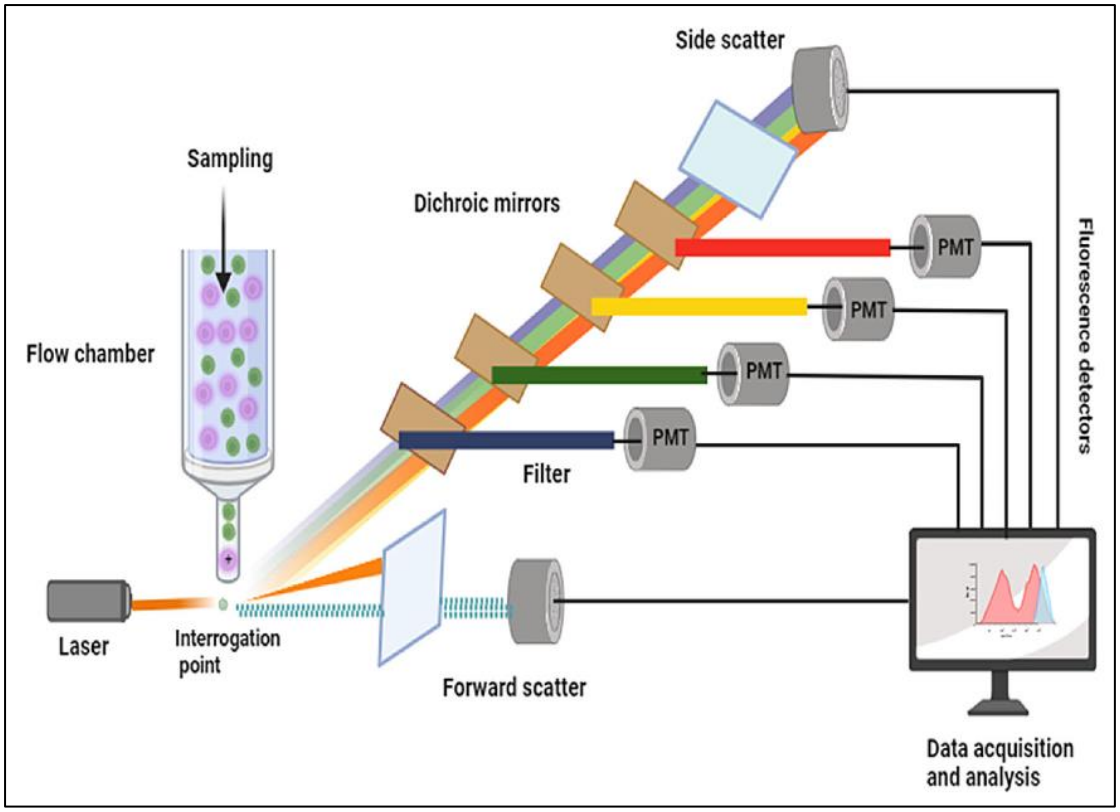

Figure 2.10. Schematic diagram of a flow cytometry and analysis[128]. The diagram illustrates how single cells in a fluid stream are interrogated by laser light, generating multiple optical signals (forward scatter, side scatter, and fluorescence) that are collected and converted to digital data for quantitative cellular analysis

2.12.1. Cell Cycle Analysis

Cell cycle analysis quantitatively detects the DNA content of cells using PI to assess the distribution of cells in different cycle phases (G0/G1, S, G2/M)[129]. PI is a fluorescent dye that can penetrate the cell membrane and bind to double-stranded DNA, and the fluorescence intensity after binding is proportional to the DNA content[129]. In cell cycle analysis, fixed cells are stained with PI in the presence of RNase, and the fluorescence intensity of each cell is measured by a flow cytometer to infer the distribution of cell populations in each cycle phase. Cells in G0/G1 phase have a single DNA content (2N), S phase cells have DNA content between 2N and 4N, and G2/M phase cells have a double DNA content (4N)[129].

Cells were seeded and treated for 48 hours after which they were trypsinised, washed with PBS, and fixed in cold 70% ethanol (2 mL PBS cell suspension added to 8 mL ethanol) at -20°C for ≥30 minutes. Fixed cells (1×10^6) were collected (300×g, 5 minutes), washed twice with PBS (600×g, 5 minutes), and stained with 0.5 mL FxCycle™ PI/RNase solution (Thermo Fisher Scientific, USA) for 15-30 minutes in the dark. Analysis was performed using FACSymphony A5 flow cytometer (BD Biosciences, USA; 488 nm excitation, 585/42 nm emission) with minimum 50,000 events/sample. Cell cycle distribution was determined using FlowJo software[130].

2.12.2. Cell Apoptosis Detection

Annexin V-FITC/PI double staining is used to detect cell apoptosis by detecting the externalization of phosphatidylserine (PS) on the cell membrane and cell membrane integrity to distinguish cells in different stages of apoptosis and necrosis[131]. Annexin V is a protein with high affinity for PS. In the early stages of apoptosis, PS flips from the inner side of the cell membrane to the outer side, allowing Annexin V to bind and be detected. FITC (fluorescein isothiocyanate)-labelled Annexin V is used to detect early apoptotic cells ($FITC^+/PI^-$), while PI is a fluorescent dye that binds to DNA and can enter late apoptotic or necrotic cells with damaged membranes (PI^+)[131]. By separately detecting the fluorescent signals of FITC and PI using a flow cytometer, living cells ($FITC^-/PI^-$), early apoptotic cells ($FITC^+/PI^-$), late apoptotic cells ($FITC^+/PI^+$), and necrotic cells ($FITC^-/PI^+$) can be accurately distinguished[131].

Cells were seeded and treated for 48 hours after which they were collected by trypsinisation, washed with PBS (300×g, 5 minutes), and resuspended in 1X binding buffer (1×10^6 cells/mL). Cell suspension (100 µL, 1×10^5 cells) was stained with FITC Annexin V (5 µL) and PI (1 µL, 100 µg/mL) from FITC Annexin V/Dead Cell Apoptosis Kit (Invitrogen, USA) for 15 minutes in the dark, followed by 400 µL binding buffer addition. Analysis was performed using FACSymphony A5 flow

cytometer (BD Biosciences, USA; FITC: 488/530 nm; PI: 488/>575 nm) with minimum 50,000 events/sample. Population distribution was analysed using FlowJo software[130].

2.13. Statistical Analysis

All analyses were performed using GraphPad Prism version 9.5[121]. Unless otherwise specified, data are presented as the mean ± standard deviation (SD) from at least three independent experiments with at least three samples per group. The following asterisk notations are used in graphical representations to denote the level of statistical significance between compared groups: $p < 0.05$: *, $p < 0.01$: **, $p < 0.001$: ***, $p < 0.0001$: ****.

2.13.1. Statistical Tests

One-Way ANOVA: Used to compare means among three or more independent groups with a single factor.

Two-Way ANOVA: Applied to analyse the effects of two independent variables and their interaction on a dependent variable.

Three-Way ANOVA: Employed to investigate the impact of three independent variables and their interactions on a dependent variable.

Multiple Comparisons: Applied when a significant result was obtained from an ANOVA, appropriate *post hoc* tests, such as Tukey's or Dunnett's test, were conducted to identify specific group differences while controlling for multiple comparisons.

CHAPTER 3
Results

TBX2, a member of the T-box transcription factor family, is frequently overexpressed in various cancers and plays crucial roles in tumour progression through multiple mechanisms, including cell cycle regulation and epithelial-mesenchymal transition[132–134]. While TBX2 has been found to be significantly upregulated in pancreatic ductal adenocarcinoma (PDAC) patient tissues[135] and is associated with poor prognosis and distant metastasis[136], its specific molecular mechanisms in PDAC remain largely unexplored. Recently, a marine-derived compound Chromomycin A5 (CA5) was identified as a specific TBX2 inhibitor that can effectively suppress its transcriptional activity, and that can exert anticancer effects through TBX2 inhibition in several cancer types[100,101].

Given the challenges with current PDAC treatments, particularly drug resistance to standard therapies like gemcitabine, investigating both TBX2's role and its targeted inhibition by CA5 could provide new therapeutic strategies for PDAC treatment.

3.1. Identification of TBX2 function in PDAC

To date, only one clinical study has associated high TBX2 expression with PDAC development and metastasis[135], but whether TBX2 directly impacts these processes are not known. To fill this knowledge gap, TBX2 levels were first screened in four PDAC cell lines available in the laboratory. TBX2 was then transiently knocked down in the cell line which express high levels of TBX2 and the impact on cell proliferation and migration was investigated.

3.1.1. Screening of TBX2 expression in PDAC cell lines

To identify PDAC cell lines with high TBX2 levels, we first determined the TBX2 copy number and protein levels in the SW1990, BxPc-3, CFPAC-1, and PANC-1 PDAC cell lines using the DepMap database and western blotting respectively[137]. The results showed that the SW1990 and PANC-1 cell line had the highest TBX2 copy number (**Figure 3.1A**) and protein levels (**Figure 3.1B-C**).

3.1.2. Phenotypic changes following transient TBX2 knockdown

The SW1990 cell line, which exhibits the highest TBX2 levels, was selected and used to elucidate the function of TBX2 in PDAC cells. Briefly, SW1990 cells were transiently transfected with two different siRNAs that specifically target TBX2 or a siCTRL to exclude off target effects. After 48 hours of transfection, the cells were harvested, and total protein was extracted and subjected to western blotting to verify the TBX2 knockdown (**Figure 3.1D**), and cell proliferation (**Figure 3.1E-F**) and migration (**Figure 3.1G-I**) were measured.

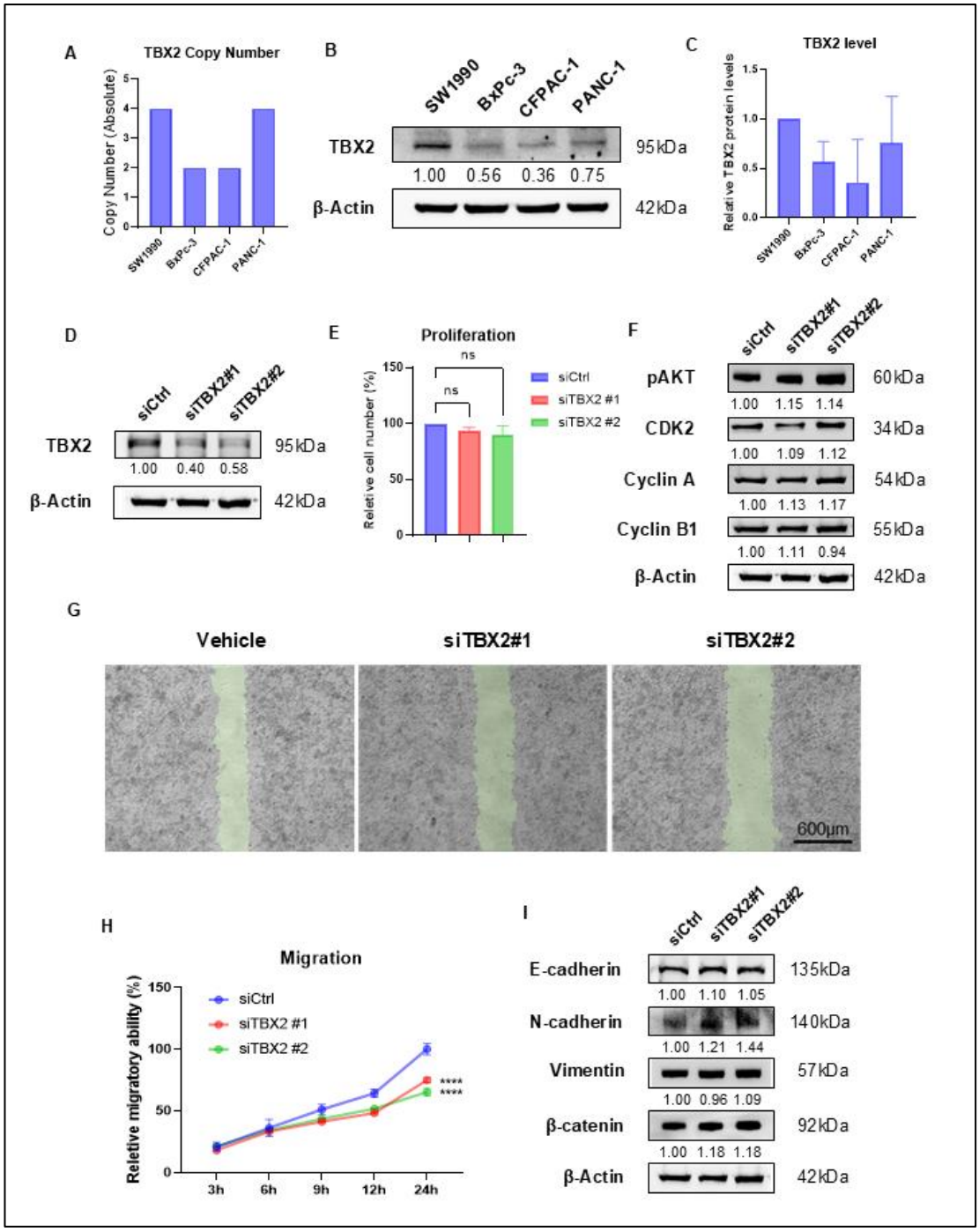

Figure 3.1. TBX2 expression in PDAC cell lines and the functional analysis of its depletion in SW1990 PDAC cells.

A. Analysis of TBX2 gene copy number in four PDAC cell lines (SW1990, BxPC-3, PANC-1, and CFPAC-1). Data were retrieved from the DepMap public database (2022 Q2 version). **B.** The levels of TBX2 protein in the indicated PDAC cell lines detected by western blot analysis. **C.** Quantification of TBX2 protein levels from the western blotting in (B). **D.** Western blot analysis of TBX2 knockdown efficiency in SW1990 cells transiently transfected with siTBX2#1 and siTBX2#2 or siCTRL for 48 hours. **E.**

SW1990 cells were transiently transfected with siTBX2#1 and siTBX2#2 or siCTRL for 48 hours, followed by cell counting using a hemocytometer. **F.** Total proteins were extracted from cells transfected for 48 hours, followed by western blot analysis of pAKT, CDK2, Cyclin A, and Cyclin B1 levels. **G.** SW1990 cells were transfected with siTBX2#1 and siTBX2#2 or siCTRL for 24 hours, followed by scratch wound creation using a sterile 2 μL pipette tip and starvation in FBS-free medium. Cells were imaged under a light microscope at 0, 3, 6, 9, 12, and 24 hours. Scale bar: 600 μm. **H.** Quantification of cell migration in wound healing assay in (G). The percentage of cell migration into the scratch area was calculated using Segment Everything plugin and normalized to the migration area of the control group. **I.** Total proteins were extracted from cells after the wound healing assay in (G) for western blot analysis of E-cadherin, N-cadherin, Vimentin, and β-catenin levels.

The numbers below the western blotting bands represent the average densitometry values from three biological repeats and protein band intensities were measured using ImageJ software and normalized to β-actin. Data represent the mean ± SD of at least three independent experiments where statistical analysis was performed using one-way ANOVA followed by *post hoc* test, with *p<0.05, **p<0.01, ***p<0.001, ****p< 0.0001, ns indicates no significant difference.

3.1.2.1. Transient TBX2 knockdown does not affect PDAC cell proliferation

Figure 3.1D shows that siTBX2#1 and siTBX2#2 were both able to effectively knock down TBX2. The impact of depleting TBX2 levels on cell proliferation was assessed through cell counting, and western blotting with antibodies to the cell proliferation markers pAKT, CDK2, Cyclin A, and Cyclin B1. pAKT is a key protein in the PI3K/AKT signalling pathway that modulates cell survival and proliferation; CDK2 is essential for G1/S phase transition; and Cyclin A and Cyclin B1 are crucial cyclins that drive cell cycle progression through S and G2/M phases, respectively. The results revealed that, knockdown of TBX2 had no significant effect on PDAC cell proliferation (**Figure 3.1E**). This observation was corroborated by the western blot analysis which showed no significant changes in the expression levels of pAKT, CDK2, Cyclin A, and Cyclin B1 (**Figure 3.1F**). These findings indicated that transient knock down of TBX2 levels had minimal impact on PDAC cell proliferation.

3.1.2.2. Transient TBX2 knockdown inhibits PDAC cell migration

We next investigated whether TBX2 might influence the migratory capacity of PDAC cells. To address this, TBX2 was transiently knocked down in SW1990 cells as described above and a scratch motility assay was performed. Briefly, following transient TBX2 knock down, SW1990 cells were cultured to confluence, after which a scratch wound was introduced using a pipette tip down the middle of the monolayer, and wound closure was monitored to assess cellular migration capacity. The results revealed that TBX2 knockdown significantly decreased the migratory ability of the SW1990 cells (**Figure 3.1G-H**).

Epithelial-Mesenchymal Transition (EMT) is a complex cellular process where epithelial cells lose their polarity and cell-cell adhesion to gain migratory and invasive properties, and it plays a crucial role in cancer metastasis. Based on the scratch motility assay results, it was therefore anticipated that the depletion of TBX2 would result in an inhibition of EMT markers. Interestingly, western blot analyses revealed that TBX2 knockdown resulted in a significant increase in levels of the mesenchymal marker N-cadherin, while the epithelial marker E-cadherin and other mesenchymal markers, vimentin, and β-catenin remained largely unchanged (**Figure 3.1I**). Considering evidence suggesting that cancer metastasis in PDAC can occur independently of the EMT pathway[138], and given the limited stability of transient TBX2 knockdown, further investigation is necessary to confirm these observations.

Through a brief study of TBX2 function in PDAC cell lines, we found that while transient TBX2 knockdown showed minimal impact on cell proliferation, it significantly decreased cell migration. These preliminary results suggest that TBX2 could represent a promising therapeutic target for PDAC treatment, though more comprehensive studies are needed to fully understand its functional roles and therapeutic potential.

3.2. Identification of CA5 as a promising compound for PDAC treatment

CA5 was previously reported to exert potent cytotoxicity against melanoma, rhabdomyosarcoma, and breast cancer cells through its ability to suppress TBX2 levels[94,100]. This study therefore evaluated the short-term and long-term cytotoxicity as well as selectivity of CA5 in 2D and 3D cell culture models of the metastatic PDAC SW1990 (spleen metastases) and CFPAC-1 (liver metastasis) cell lines. Subsequently, the impact of CA5 on SW1990 and CFPAC-1 cell migration, and invasion was measured and the molecular mechanism(s) by which CA5 exerts its anticancer activity was explored.

3.2.1. CA5 exhibits potent short-term cytotoxicity in PDAC cells

To investigate the short-term cytotoxicity of CA5, the SW1990 and CFPAC-1 cells were treated with a range of CA5 concentrations (0.1 to 100 nM) for 48 hours and cell viability was measured using the MTT assay. In these experiments, the standard first-line PDAC treatment drug Gemcitabine (Gem) was included as a reference drug. The dose-response curve for CA5 demonstrated its potent short-term cytotoxicity in the nanomolar range (**Figure 3.2A-B**), with half maximal inhibitory concentrations (IC_{50}) of 6.96 nM and 7.93 nM, for SW1990 and CFPAC-1 cells respectively. In contrast, the IC_{50} values for Gem were in the micromolar range of 2.50 μM and 8.94 μM for SW1990 and CFPAC-1 cells, respectively (**Figure 3.2D-E**). These results indicate that the IC_{50} values for CA5 were 359-fold and 1127-fold lower than Gem in the SW1990 and CFPAC-1 PDAC cell lines respectively and therefore that it exerts the same cytotoxicity as Gem at much lower concentrations.

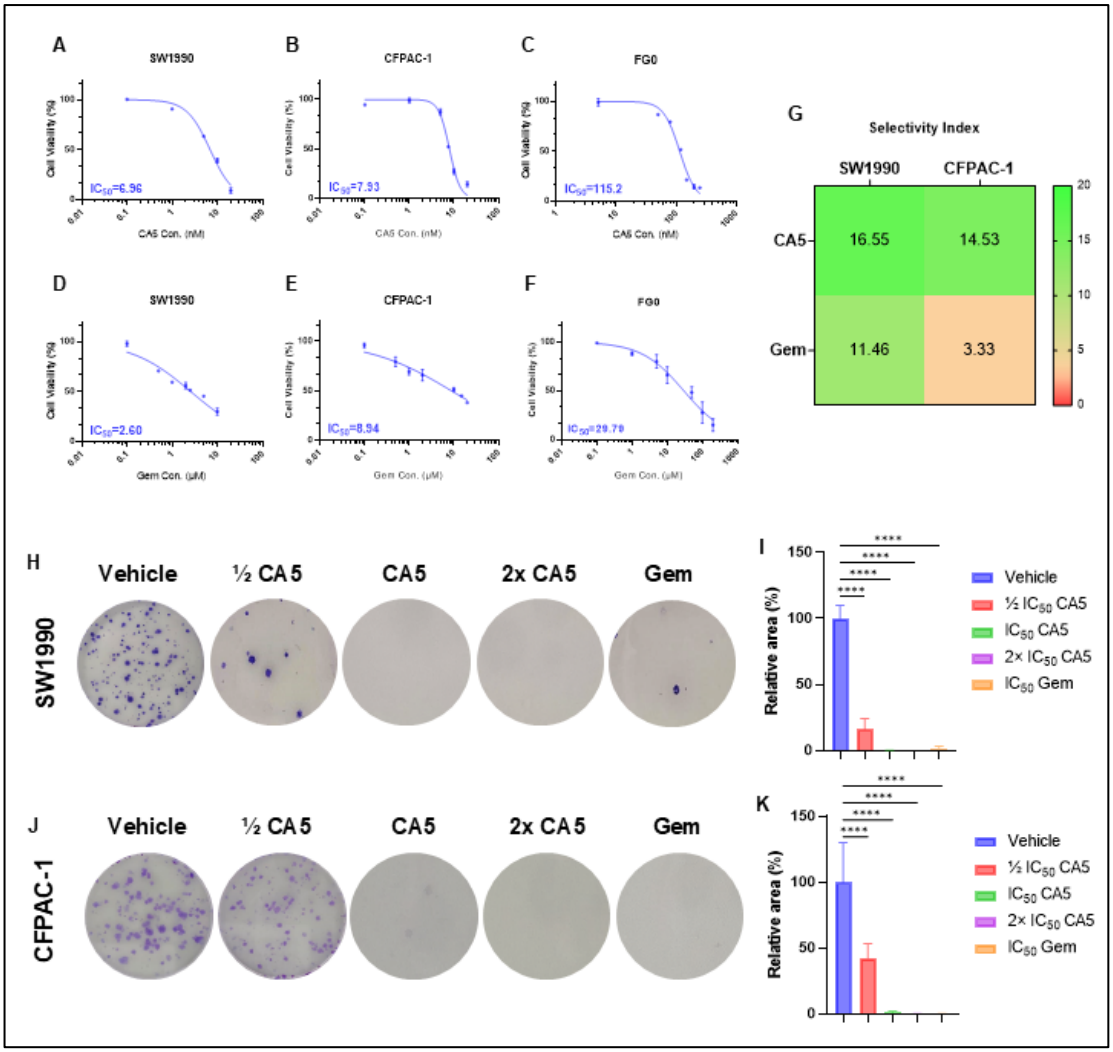

Figure 3.2. The short-term and long-term cytotoxicity and selectivity of CA5 versus Gemcitabine in PDAC cells.

A-F. Short-term cytotoxicity of CA5 on SW1990, CFPAC-1, and normal human skin fibroblasts FG0 cells treated with a range of concentrations of CA5 (A-C) and Gemcitabine (D-F) for 48 hours, followed by MTT assay to detect cell viability. GraphPad Prism 9 software was used to generate fit dose-response curves and calculate IC_{50} values. **G.** Heatmap visualization of the selectivity indices (SI) of CA5 and Gemcitabine. SI was calculated as the ratio of IC_{50} values (IC_{50} of normal fibroblasts FG0 cells / IC_{50} of SW1990 and CFPAC-1 PDAC cells). **H-K.** Long-term cytotoxicity and quantitative analysis of CA5 and Gemcitabine using colony formation assay in SW1990 (H, I) and CFPAC-1 (J, K) cells. Cells were treated with vehicle control, ½ IC_{50} CA5, IC_{50} CA5, 2× IC_{50} CA5, or IC_{50} Gem for 24 hours, then seeded at low density in drug-free medium in 35 mm dishes. After 10-14 days of culture, cells were fixed in a 1:3 mixture of glacial acetic acid and methanol and stained with 0.5% crystal violet.

Colony formation was photographed and quantified by measuring the colony area using ImageJ software and normalized to the vehicle control group.
Data represent the mean ± SD of at least three independent experiments where statistical analysis was performed using two-way ANOVA followed by *post hoc* test, with *p<0.05, **p<0.01, ***p<0.001, ****p<0.0001, ns indicates no significant difference.

3.2.2. CA5 exhibits high selectivity for PDAC cells

The selectivity of CA5 and Gem for PDAC cells was next assessed by determining their IC_{50} values in the normal human skin fibroblast cell line FG0 and then dividing these by their IC_{50} values in PDAC cells. **Figure 3.2C** shows that CA5 exhibited an IC_{50} of 115.2 nM in FG0 cells and thus its calculated selectivity indices were 16.6 and 14.5 in SW1990 and CFPAC-1 cells, respectively (**Figure 3.2G**). Gem, on the other hand, exhibited an IC_{50} of 29.79 μM in FG0 cells (**Figure 3.2F**), and thus had selectivity indices of 11.46 and 3.33 for SW1990 and CFPAC-1 cells, respectively (**Figure 3.2G**). CA5 was thus 1.45-fold and 4.35-fold more selective than Gem for SW1990 and CFPAC-1 cells respectively.

3.2.3. CA5 exhibits potent long-term cytotoxicity in PDAC cells

Clonogenic assays which predict potential tumour recurrence after drug treatment[139] were next performed. Briefly, SW1990 and CFPAC-1 cells were treated with ½ IC_{50}, IC_{50} and 2X IC_{50} CA5 or IC_{50} Gem for 24 hours after which they were replated at low density in drug-free medium and allowed to form colonies for 14 days. The results show that CA5 inhibited the colony forming ability of both PDAC cell lines in a dose-dependent manner (**Figure 3.2H-K**). Indeed, compared to vehicle treated cells, ½ IC_{50} CA5 reduced SW1990 and CFPAC-1 colony formation by approximately 85%, and 60% respectively while IC_{50} and 2x IC_{50} CA5 completely inhibited the colony forming ability of both cell lines (**Figure 3.2H-K**). Notably, SW1990 cells treated with IC_{50} Gem were still able to form colonies, albeit statistically significantly less than vehicle

treated cells. The results of the clonogenic assays demonstrated that CA5 significantly inhibited the colony-forming abilities of SW1990 and CFPAC-1 cells and exhibited long-term cytotoxicity like or greater than that observed for Gem.

3.2.4. CA5 exhibits potent cytotoxicity in PDAC 3D spheroid models

Compared to 2D cell cultures, 3D cell culture models more closely resemble the in vivo tumour cellular microenvironment, and is therefore a more reliable model for investigating the efficacy of a drug[140]. We, therefore, wished to establish spheroids of CFPAC-1 and SW1990 cells and then to use them as 3D models to test the cytotoxicity of CA5. Briefly, SW1990 and CFPAC-1 spheroids were established by seeding 5000 cells on agarose-coated plates for 6 days. However, unlike the CFPAC-1 cells which formed intact spheroids, SW1990 cells formed clumps which expanded into a layer over time, and they were therefore not used in these experiments (**Figure 3.3A**). CFPAC-1 spheroids were treated with CA5, or Gem (Day0 and Day3) and the volume of the spheroids were measured every 2 days, and on day 6 the spheroids were stained with Calcein-AM/PI to assess spheroid viability.

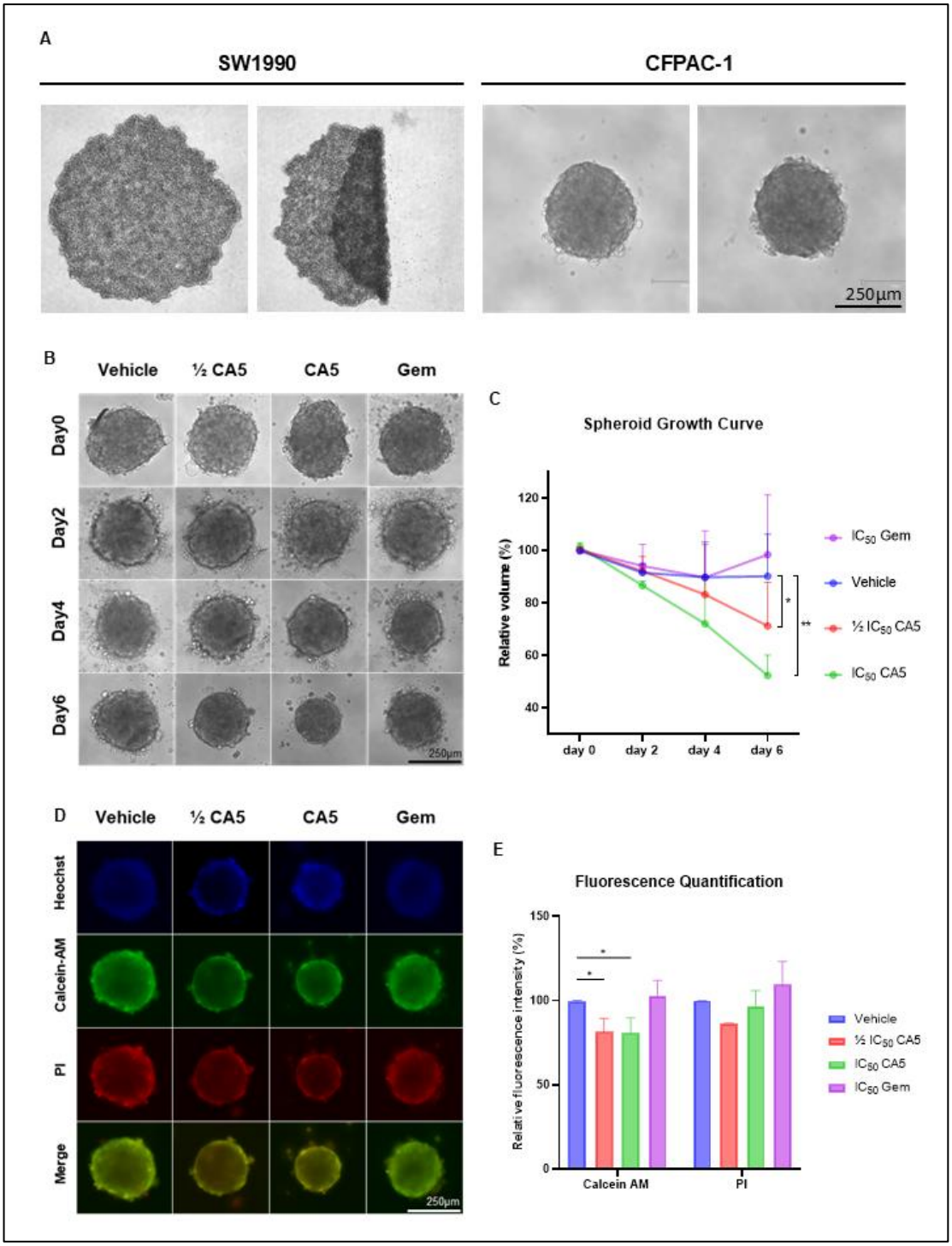

Figure 3.3. Efficacy of CA5 on three-dimensional (3D) spheroid model of PDAC cells.

A. Representative bright-field microscopy images showing morphological differences between SW1990 and CFPAC-1 pancreatic cancer spheroids after 6 days of culture on 1.2% agarose to prevent cell adhesion. Scale bar: 250 µm. **B-C.** Representative bright-field microscopy images (B) and quantification (C) of CFPAC-1 spheroids formed after

6 days of culture and treated with vehicle control, ½ IC_{50} CA5, IC_{50} CA5, or IC_{50} Gem on day 0 and day 3 and assessed for 6 days. Images were captured every two days and spheroid growth was quantified by measuring the area of spheroid using Segment Everything plugin to plot growth curves. Scale bar: 250 μm. **D-E.** Fluorescent live/dead cell staining and quantification of CFPAC-1 spheroids in (**A**) after 6 days of CA5 and Gem treatment. The spheroids were stained with Calcein-AM (green fluorescence) which stains live cells, propidium iodide (PI, red fluorescence) which stains dead cells, and Hoechst (blue fluorescence, nuclei) and imaged using a fluorescence microscope. Scale bar: 250 μm. At least 8 independent spheroids were analysed per group, and the average fluorescence intensities were measured using ImageJ software for statistical analysis.
Data represent the mean ± SD of at least three independent experiments with at least five samples per group. Statistical analysis was performed using two-way or three-way ANOVA followed by *post hoc* test. All microscopic images were captured using an EVOS M5000 fluorescence imaging system (20× objective). *p<0.05, **p<0.01, ***p<0.001, ****p<0.0001, ns indicates no significant difference.

The results showed that on day 6, ½ IC_{50} and IC_{50} CA5 caused significant spheroid shrinkage compared to the vehicle control (**Figure 3.3B, C**). Furthermore, the impact of Gem on spheroid growth was comparable to vehicle control (**Figure 3.3B, C**). In the Calcein-AM/PI dual staining assay Calcein-AM stains viable cells green and propidium iodide (PI) stains dead cells red. The results from this assay show that the Calcein-AM fluorescence intensity was significantly reduced in CFPAC-1 spheroids treated with ½ IC_{50} and IC_{50} CA5, compared to those treated with vehicle or Gem (**Figure 3.3D, E**). It is worth noting that there was no statistical difference between the Calcein-AM staining of vehicle and Gem treated spheroids suggesting that Gem did not inhibit CFPAC-1 spheroid viability. Interestingly, quantitation of the PI fluorescence intensity showed that there were no significant differences between the vehicle, CA5- or Gem-treated groups. This may be due to the tight cellular connections formed by the high expression of E-cadherin in CFPAC-1 spheroids, which might have hindered the penetration of the dye into the spheroid core[141]. Overall, unlike Gem, CA5 exhibited cytotoxicity in the 3D PDAC spheroid model used in this study.

3.2.5. CA5 inhibits PDAC cell invasion and migration

PDAC is a highly metastatic cancer and, therefore, an ideal therapeutic agent to treat this malignancy must have anti-metastatic activity[136]. The invasive and migratory ability of SW1990 and CFPAC-1 cells following short-term exposure to CA5 were therefore evaluated using transwell invasion and scratch motility assays respectively.

Briefly, for the transwell invasion assays, SW1990 and CFPAC-1 cells were treated with CA5 or Gem for 24 h before being seeded onto Matrigel-coated transwell inserts and cells that invaded the lower chamber of the transwell plate were stained with crystal violet. In both cell lines, CA5 demonstrated a dose-dependent inhibition of invasion and IC_{50} CA5 exhibited stronger anti-invasive effects than IC_{50} Gem (**Figure 3.4A-C**). Indeed, compared to the vehicle treated SW1990 and CFPAC-1 cells, ½ IC_{50} CA5 reduced invasion by approximately 73% and 62%; IC_{50} CA5 by 94% and 100%, and IC_{50} Gem by 47% and 92% respectively (**Figure 3.4A-C**).

For the scratch motility assays, confluent monolayer SW1990 and CFPAC-1 cells were treated with ½ IC_{50} CA5, IC_{50} CA5 or IC_{50} Gem immediately after scratch formation, and wound closure was monitored over 24 hours to assess the effects on cell migration. The results showed that at 24 hours both concentrations of CA5 and IC_{50} Gem effectively inhibited wound closure in both cell lines compared to vehicle control (**Figure 3.4D**). Quantitative analysis revealed that CA5 exhibited a statistically significant and dose-dependent inhibition of migration for both SW1990 and CFPAC-1 cells at 24 hours (**Figure 3.4E, F**). Furthermore, the inhibitory effect of IC_{50} CA5 was comparable to that of IC_{50} Gem in both PDAC cell lines tested (**Figure 3.4E, F**).

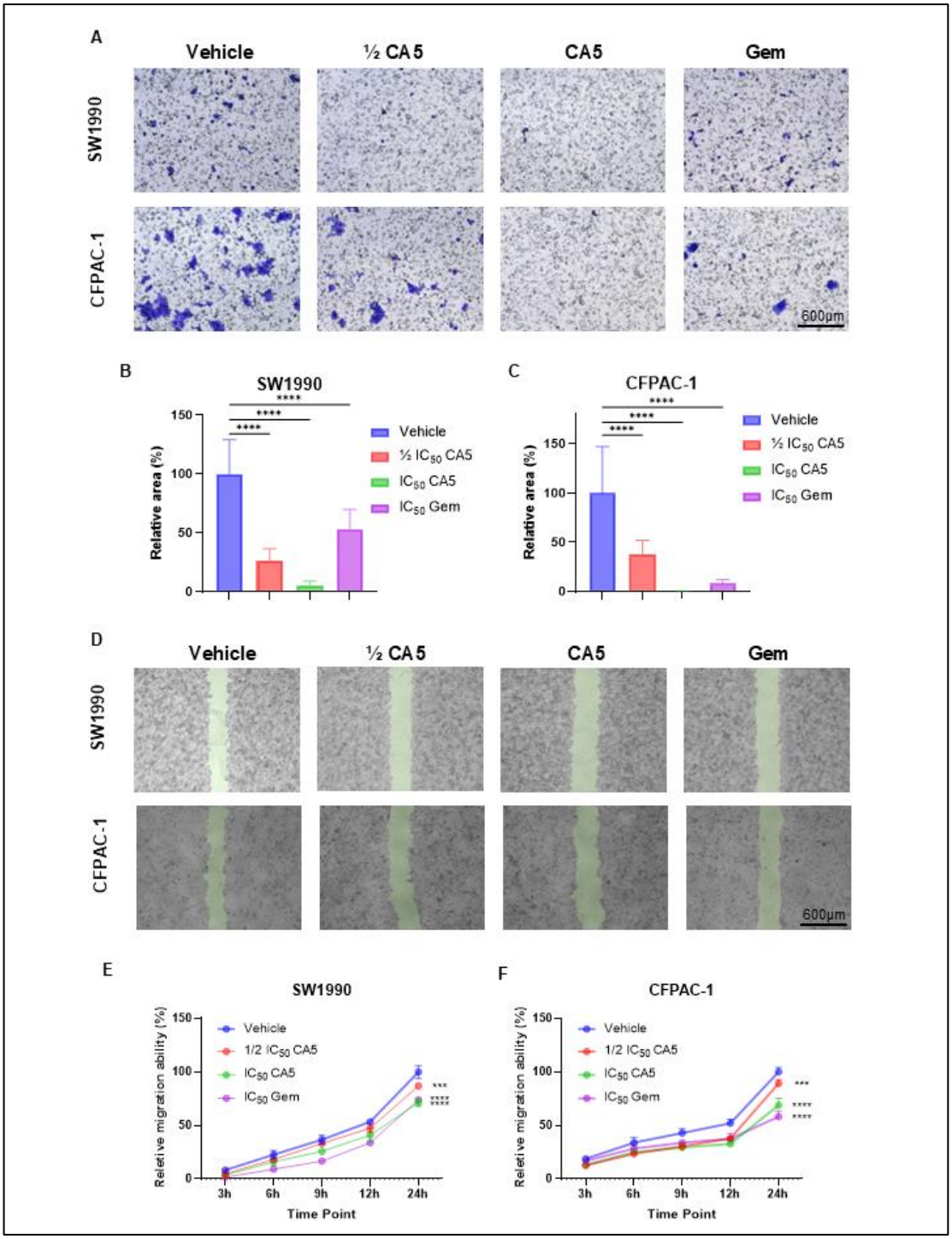

Figure 3.4. The effects of CA5 on migration and invasion capabilities of PDAC cells.

A. Representative images of transwell invasion assay showing the effects of CA5 or Gemcitabine treatment on SW1990 and CFPAC-1 cell invasion. Cells were pre-treated in 12-well plates with vehicle control, ½ IC_{50} CA5, IC_{50} CA5, or IC_{50} Gem for 24 hours. After treatment, cells were transferred to Matrigel-coated transwell inserts and subjected to FBS gradient-induced invasion for 24 hours. Cells that invaded through

the membrane were fixed in a 1:3 mixture of glacial acetic acid and methanol and stained with 0.5% crystal violet, and imaged under a microscope. Scale bar: 600 μm. **B-C.** Quantitative analysis of the invasive ability of SW1990 (B) and CFPAC-1 (C) cells in (A). Invasive cells were counted in ten random fields from captured images and the relative cell invasion was calculated and normalized to the invasion observed in the vehicle control group. **D.** Representative microscopic images of wound healing assay demonstrating the effects of CA5 and Gemcitabine treatment on SW1990 and CFPAC-1 cells migration. Cells were seeded in 12-well plates, followed by scratch wound creation using a sterile 2 μL pipette tip, subjected to FBS-serum starvation, and treated with vehicle control, ½ IC_{50} CA5, IC_{50} CA5, or IC_{50} Gem to the culture medium. Cells were imaged under a light microscope at 0, 3, 6, 9, 12, and 24 hours. Scale bar: 600 μm. **E-F.** Quantitative analysis of wound healing assay in SW1990 (E) and CFPAC-1 (F) cells in (D). The percentage of cells migrating into the scratch area was calculated using Segment Everything plugin at different time points (0, 3, 6, 9, 12, and 24 hours) and normalized to the migration area of the vehicle control group at the end of the experiment.
Data represent the mean ± SD of at least three independent experiments. Statistical analysis was performed using two-way ANOVA followed by *post hoc* test. All microscopic images were captured using an EVOS M5000 fluorescence imaging system (10× objective). *p<0.05, **p<0.01, ***p<0.001, ****p<0.0001, ns indicates no significant difference.

Taken together, the above experiments demonstrate that in PDAC cells, CA5 was selectively cytotoxic in short- and long-term 2D cell culture; inhibited 3D spheroid growth and viability; and inhibited cell invasion and migration. In many of these experiments, CA5 exerted superior anti-cancer activity compared to the clinical standard Gemcitabine. These findings strongly support the potential of CA5 as an anti-PDAC drug and lay a solid foundation for subsequent mechanistic studies.

3.2.6. Molecular mechanism of CA5 action in PDAC

To elucidate the molecular mechanisms by which CA5 exerts its anti-cancer activities in PDAC, this study explored its effects on the DNA damage response, cell cycle progression, and apoptosis induction.

3.2.6.1. CA5 binds to double-stranded DNA

Previous reports have shown that CA3, which has a structure highly similar to CA5, can reversibly bind to CG-rich regions in the minor groove of DNA[93], thereby exerting anti-cancer effects. Consequently, the DNA-binding capacity of CA5 was first verified through fluorescence spectroscopy measurements, a technique that measures changes in a molecule's fluorescence properties upon binding to target molecules. When a fluorescent molecule like CA5 absorbs light at specific wavelengths (excitation), it becomes excited to a higher energy state and subsequently releases energy by emitting light at longer wavelengths (emission). Since CA5 is inherently fluorescent, its interaction with DNA can be monitored by changes in the intensity of the emission band in its fluorescence spectrum when in its bound versus unbound states.

The fluorescence excitation-emission spectra of CA5 were analysed using a fluorescence spectrophotometer, scanning excitation wavelengths from 200-500 nm and emission wavelengths from 450-700 nm to generate a fluorescence intensity heat map (**Figure 3.5A**). The heat map revealed two characteristic excitation-emission pairs: a primary peak with excitation at 410 nm leading to emission at 530 nm, and a secondary peak with excitation at 270 nm resulting in emission at 550 nm, with the colour intensity indicating the strength of fluorescence (**Figure 3.5A**).

DNA itself showed a weak response to 410 nm excitation, with negligible fluorescence emission at 530 nm (**Figure 3.5B**). However, upon the addition of varying concentrations of DNA to the CA5 solution and excitation at 410 nm, significant fluorescence quenching was observed (**Figure 3.5C**). Indeed, the fluorescence emission intensity at 530 nm decreased markedly, and the maximum emission peak red-shifted to 544 nm (**Figure 3.5C**). This fluorescence quenching and peak shift phenomenon indicate that CA5 can bind to DNA and that the presence of DNA alters the fluorescent properties of CA5.

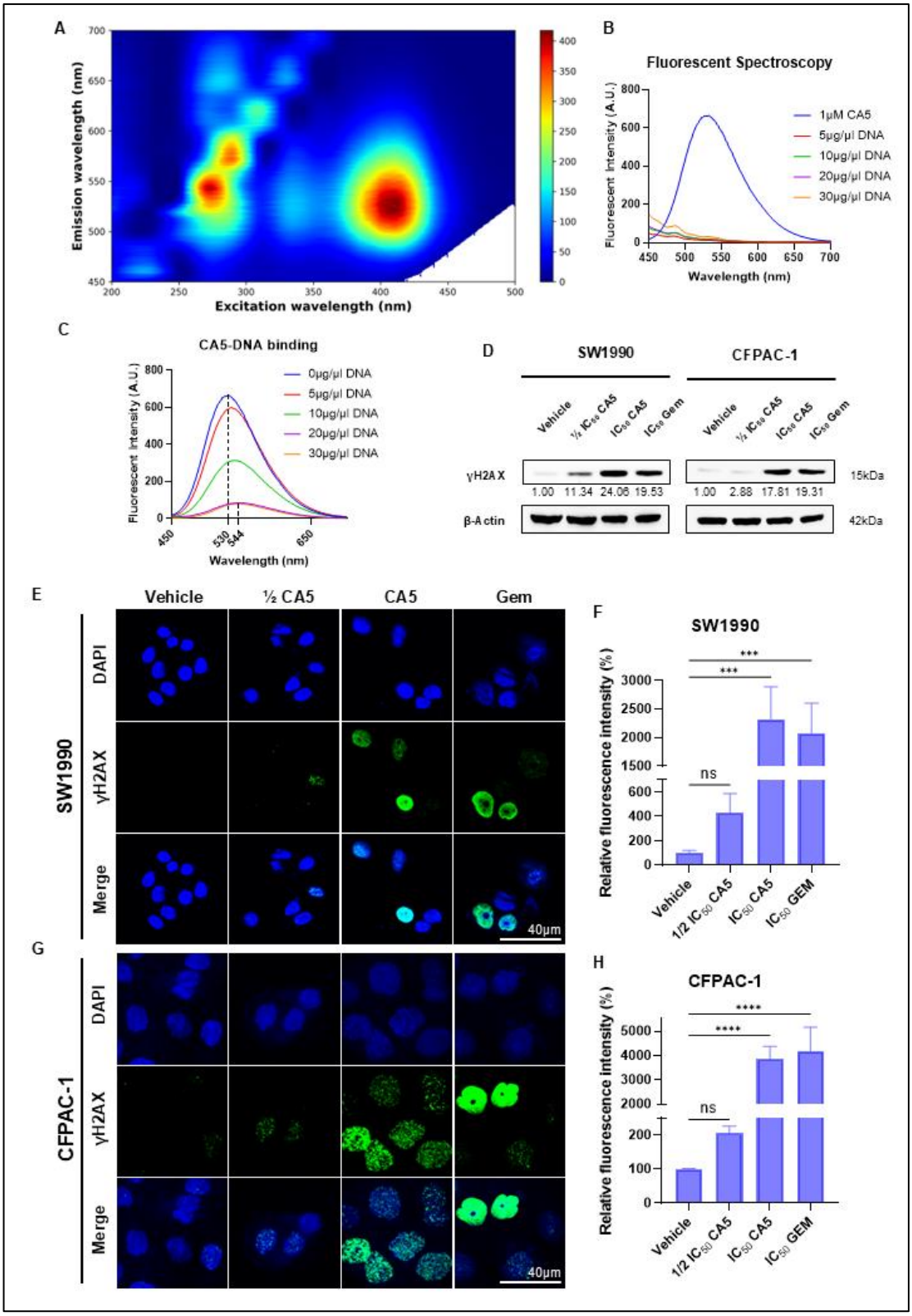

Figure 3.5. Characterization of CA5-DNA interaction mechanisms and evaluation of CA5-induced DNA damage response in PDAC cells.

A. Fluorescence excitation-emission matrix analysis of CA5 (room temperature dissolved in DMSO). CA5 (1 μM) was excited at wavelengths ranging from 200-500 nm, and fluorescence emission was recorded at 450-700 nm. The fluorescence intensities were measured using a Cary Eclipse fluorescence spectrophotometer, interpolated using SciPy's Clough-Tocher 2D algorithm, and visualised as a heat map in Python. **B.** Effects of DNA concentration on background fluorescence. Fluorescence measurements at 530 nm (excitation: 410 nm) were performed with either varying concentrations of plasmid DNA (5-30 μg/μL) or 100 μM CA5 alone. **C.** Fluorescence spectral analysis of CA5-DNA complex formation. Increasing concentrations of plasmid DNA (5-30 μg/μL) were added to 100 μM CA5, excited at 410 nm, and emission spectra were measured from 450-700 nm. A dose-dependent quenching effect was observed at the 530 nm emission peak. **D.** Western blot analysis of DNA damage marker γH2AX expression from protein extracted from SW1990 and CFPAC-1 cells after treatment with vehicle control, ½ IC_{50} CA5, IC_{50} CA5, or IC_{50} Gem for 48 hours. **E-H** Representative immunofluorescence analysis of γH2AX levels and quantification of fluorescence intensity. Panels (E) and (G) show representative images from SW1990 (E) and CFPAC-1 (G) cells following treatments as described in (D). Scale bar: 40 μm. Panels (F) and (H) show the corresponding quantification of γH2AX fluorescence intensity from 25 random fields from captured images for SW1990 (F) and CFPAC-1 (H) cells, respectively.

The numbers below the western blotting bands represent the average densitometry values from three biological repeats and protein band intensities were measured using ImageJ software and normalized to β-actin. Data represent the mean ± SD of at least three independent experiments. All microscopic images were captured using an LSM 880 confocal microscope imaging system (63× objective). Statistical analysis was performed using two-way ANOVA followed by *post hoc* test, with *p<0.05, **p<0.01, ***p<0.001, ****p<0.0001, ns indicates no significant difference.

3.2.6.2. CA5 induces DNA damage in PDAC cells

The induction of DNA damage by chemical agents is an effective strategy for killing cancer cells[142]. CA5's ability to induce DNA damage in SW1990 and CFPAC-1 cells was therefore assessed by measuring the levels of γH2AX, a sensitive marker of DNA damage, using western blotting and immunocytochemistry (ICC) techniques. Western blot analyses showed that 48 h of CA5 treatment led to a dose-dependent upregulation

of γH2AX in SW1990 and CFPAC-1 cells (**Figure 3.5D**). Gem treatment for 48 h also resulted in an increase in γH2AX in both PDAC cell lines. For ICC analyses, SW1990 and CFPAC-1 cells were also treated with CA5 or Gem for 48 h and the results confirmed those obtained for western blot analyses (**Figure 3.5E-H**). Indeed, IC_{50} CA5 showed stronger γH2AX signals than ½ IC_{50} CA5 in the nuclei of both cell lines, and the staining intensity was comparable to that obtained for IC_{50} Gem treatment (**Figure 3.5E-H**). Together these results indicated that CA5 can effectively induce DNA damage in PDAC cells.

3.2.6.3. CA5 induces cell cycle arrest in PDAC cells

DNA damage activates checkpoint mechanisms in mammalian cells, which halts cell cycle progression to provide sufficient time for DNA repair[143]. To investigate if the CA5-induced DNA damage led to cell cycle arrests, SW1990 and CFPAC-1 cells treated with drug for 48 h were subjected to flow cytometry analyses. The results revealed that ½ IC_{50} and IC_{50} CA5 treatment led to a marked increase in the S-phase population of SW1990 and CFPAC-1 cells (**Figure 3.6A-B**). In addition, ½ IC_{50} CA5, and to a lesser extent IC_{50} CA5, led to an increase in SW1990 cells in the G2/M phase (**Figure 3.6A)**. Gem treatment triggered an S-phase arrest in SW1990 cells but a G2/M arrest in CFPAC-1 cells (**Figure 3.6A-B**). Importantly, the flow cytometry analyses revealed that CA5 treatment induced a sub-G1 population of SW1990 and CFPAC-1 cells, indicating DNA fragmentation due to cell death (**Figure 3.6A-B**). In summary, CA5 induced DNA damage, triggered cell cycle arrests and cell death in PDAC cells.

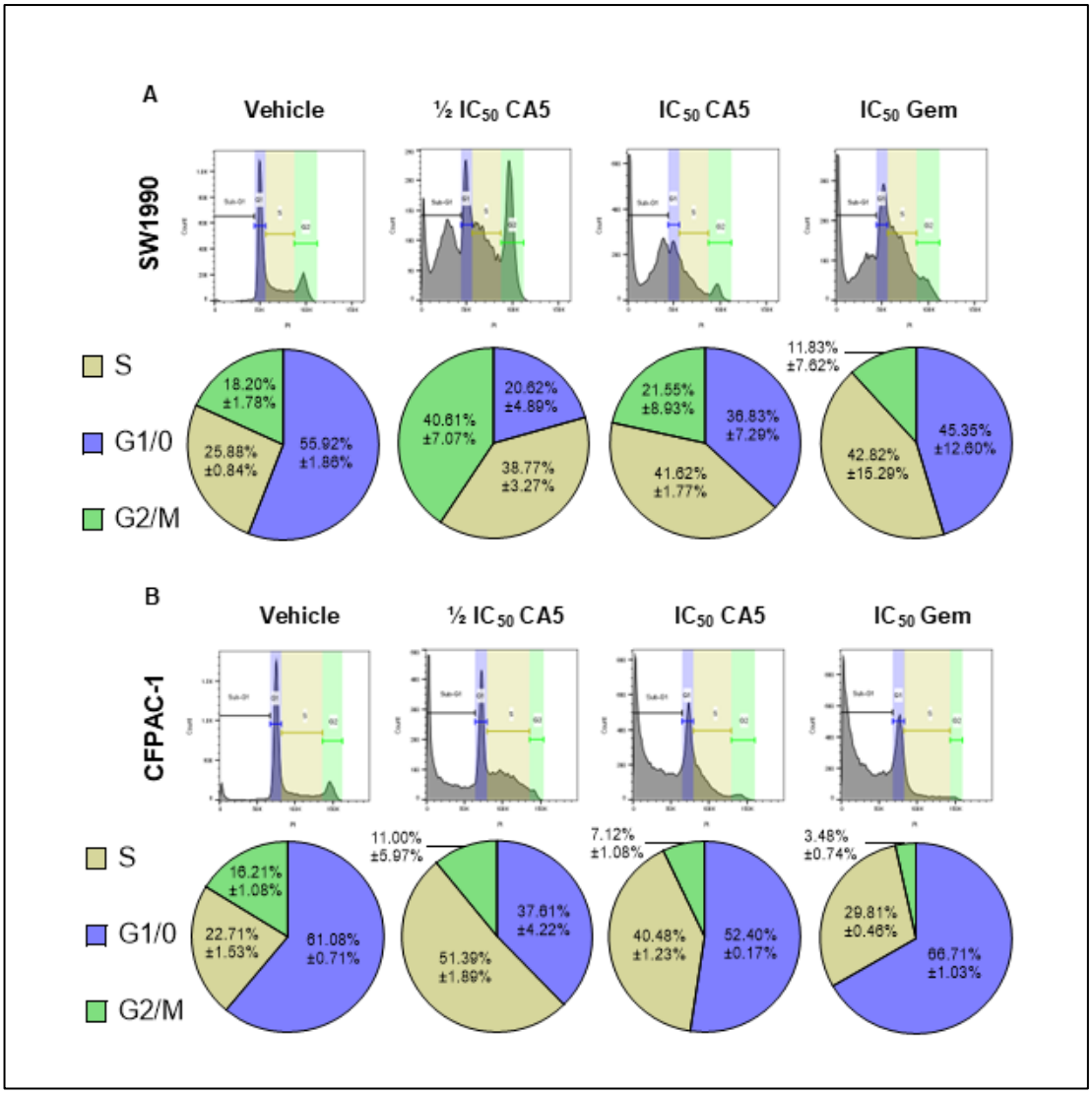

Figure 3.6. Cell cycle distribution patterns and regulation of cell cycle-related proteins in PDAC cells following CA5 treatment.

A-B. Representative flow cytometry histograms and quantitative analysis of cell cycle phase distribution of SW1990 (A) and CFPAC-1 (B) cells treated with vehicle control, ½ IC_{50} CA5, IC_{50} CA5, or IC_{50} Gem for 48 hours. Following treatment, cells were collected, fixed, and stained with propidium iodide (PI) for cell cycle analysis by flow cytometry. The percentage of cells in each phase was calculated from the flow cytometry data using FlowJo software.

Data represent the mean ± SD of at least three independent experiments with at least 50,000 cells recorded per experiment.

3.2.6.4. CA5 induces apoptosis in PDAC

To investigate if the CA5 induced sub-G1 peak observed in the flow cytometry analyses was due to PDAC cells undergoing apoptosis, Annexin V-FITC/PI double staining and flow cytometry analyses were performed. The results revealed that CA5 induced a dose-dependent decrease in the percentage of viable SW1990 and CFPAC-1 cells with a corresponding increase in the percentages of apoptotic and necrotic cells (**Figure 3.7A-D**). Indeed, in SW1990 cells, ½ IC_{50} CA5 reduced cell viability to 91.33% and induced the total apoptotic cell population (early + late) to 7.7% and the necrotic cell population to 0.92% and IC_{50} CA5 reduced cell viability to 41.1% and induced the total apoptotic cell population to 46.2% and the necrotic cell population to 12.8% (**Figure 3.7A, C**). CFPAC-1 cells demonstrated higher sensitivity to CA5, with ½ IC_{50} CA5 reducing cell viability to 62.2% and inducing 35.8% total apoptosis and 2% necrosis and IC_{50} CA5 further reducing viable cells to 26.7% and increased total apoptosis to 61.8% and necrosis to 11.5% (**Figure 3.7B, D**). While the SW1990 cells were more sensitive to CA5 than Gem (59% vs 32% total cell death) (**Figure 3.7C**), the CFPAC-1 cells were more sensitive to Gem than CA5 (83% vs 73% total cell death) (**Figure 3.7D**). Furthermore, CFPAC-1 cells were more sensitive than the SW1990 cells to both CA5 (73% vs 59% total cell death) and Gem (83% vs 32% total cell death) (**Figure 3.7C, D**).

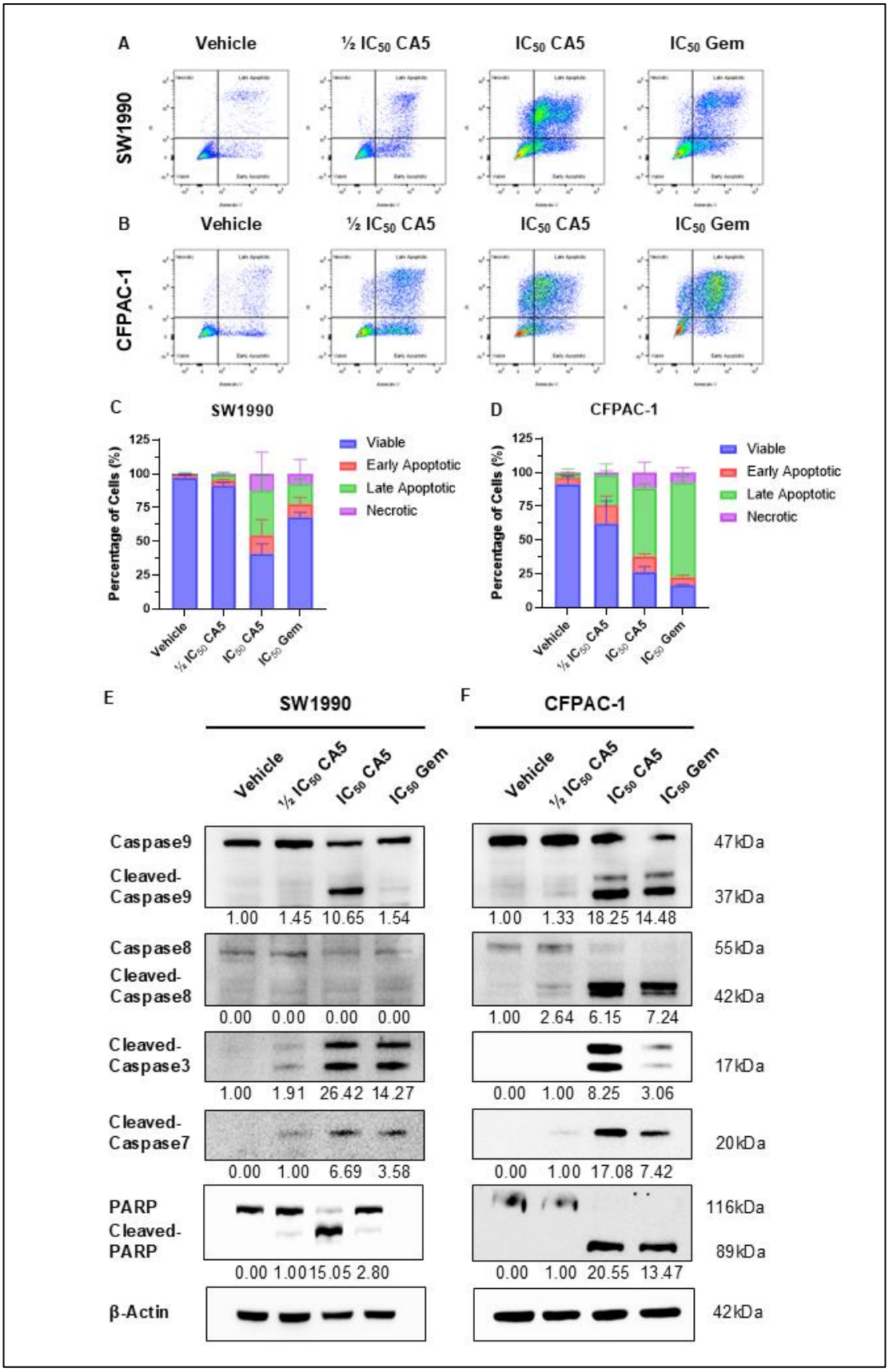

Figure 3.7. Apoptotic response and apoptosis-related protein expression in PDAC cells following CA5 treatment.

A-D. Flow cytometry analysis (A, B) and quantitative assessment (C, D) of apoptosis in SW1990 (A, C) and CFPAC-1 (B, D) cells after treatment with vehicle control, ½ IC_{50} CA5, IC_{50} CA5, or IC_{50} Gem for 48 hours. Cells were collected and stained with Annexin V-FITC and PI for apoptosis detection. Representative scatter plots show the distribution of cells in different quadrants: viable (Annexin V^-/PI^-), early apoptotic (Annexin V^+/PI^-), late apoptotic (Annexin V^+/PI^+), and necrotic (Annexin V^-/PI^+) populations. At least 50,000 cells were recorded per experiment. Quantitative analyses of the percentage of cells in each population are presented as bar graphs. **E-F.** Western blot analysis of apoptotic markers in SW1990 (E) and CFPAC-1 (F) cells following treatment with vehicle control, ½ IC_{50} CA5, IC_{50} CA5, or IC_{50} Gem for 48 hours. Total protein was extracted for western blot analysis of apoptosis-related proteins.
The numbers below the western blotting bands represent the average densitometry values from three biological repeats and protein band intensities were measured using ImageJ software and normalized to β-actin. Data represent the mean ± SD of at least three independent experiments. *$p<0.05$, **$p<0.01$, ***$p<0.001$, ****$p<0.0001$, ns indicates no significant difference.

To confirm that CA5 induced apoptosis in PDAC cells, we performed western blot analyses with antibodies to intrinsic and extrinsic apoptotic markers. The intrinsic apoptotic pathway is primarily mediated by cleaved caspase-9, while the extrinsic pathway is mainly regulated by cleaved caspase-8. Both pathways converge on the effector caspases-3/7 which lead to PARP cleavage. The results from the western blot analyses show that in SW1990 cells, IC_{50} CA5 strongly activated the intrinsic pathway since it increased cleaved caspase-9, caspases-3/7 and PARP (**Figure 3.7E**). In these cells, ½ IC_{50} CA5 only mildly increased levels of cleaved caspases-3/7 and PARP and while IC_{50} Gem induced similar levels of cleaved caspases-3/7 as IC_{50} CA5 it increased cleaved PARP levels similar to ½ IC_{50} CA5 (**Figure 3.7E**). In CFPAC-1 cells, IC_{50} CA5 activated both intrinsic and extrinsic pathways since it robustly increased both cleaved caspase-8 and caspase-9, leading to the activation of cleaved caspases-3/7 and PARP (**Figure 3.7F**). The results also showed that in CFPAC-1 cells, ½ IC_{50} CA5 had very little effects on the apoptotic markers and Gem activated both intrinsic and extrinsic apoptotic pathways as observed for IC_{50} CA5 (**Figure 3.7F**).

Overall, these results demonstrate that CA5 effectively induces PDAC cell death by apoptosis albeit through different apoptotic pathways depending on the cellular context.

3.2.7. CA5 may exert its effects in PDAC through modulation of TBX2

Previous literature has reported that CA5 not only binds to DNA but it also exhibits a high affinity for the transcription factor TBX2 and in melanoma, TBX2 levels have been shown to influence CA5 efficacy[144]. Therefore, the impact of CA5 on TBX2 levels and its downstream genes in PDAC were initially assessed using qRT-PCR and western blotting techniques.

Results from qRT-PCR analyses show that ½ IC_{50} CA5 significantly increased TBX2 mRNA levels in both SW1990 and CFPAC-1 cells (**Figure 3.8A-B**). However, IC_{50} CA5 treatment resulted in a significant decrease in TBX2 mRNA levels in SW1990 cells (**Figure 3.8A**), but, albeit not significant, it increased TBX2 mRNA levels in CFPAC-1 cells (**Figure 3.8B**). Western blot analyses revealed that while ½ IC_{50} CA5 had minimal effects on TBX2 levels in SW1990 cells, it slightly increased TBX2 levels in CFPAC-1 cells (**Figure 3.8C-D**). Consistent with what has been previously reported for the effect of IC_{50} CA5 on TBX2 levels in other cancers, it decreased TBX2 levels in both PDAC cell lines tested (**Figure 3.8C-D**). The discrepancy between the effects of CA5 on TBX2 mRNA and protein levels are consistent with studies from our laboratory that showed that the drug binds to TBX2 and targets it for degradation by the proteosome S pathway (**unpublished data**). It is worth noting that while Gem treatment dramatically increased TBX2 mRNA levels it had little effect on TBX2 protein levels in SW1990 and CFPAC-1 cells (**Figure 3.8A-D**).

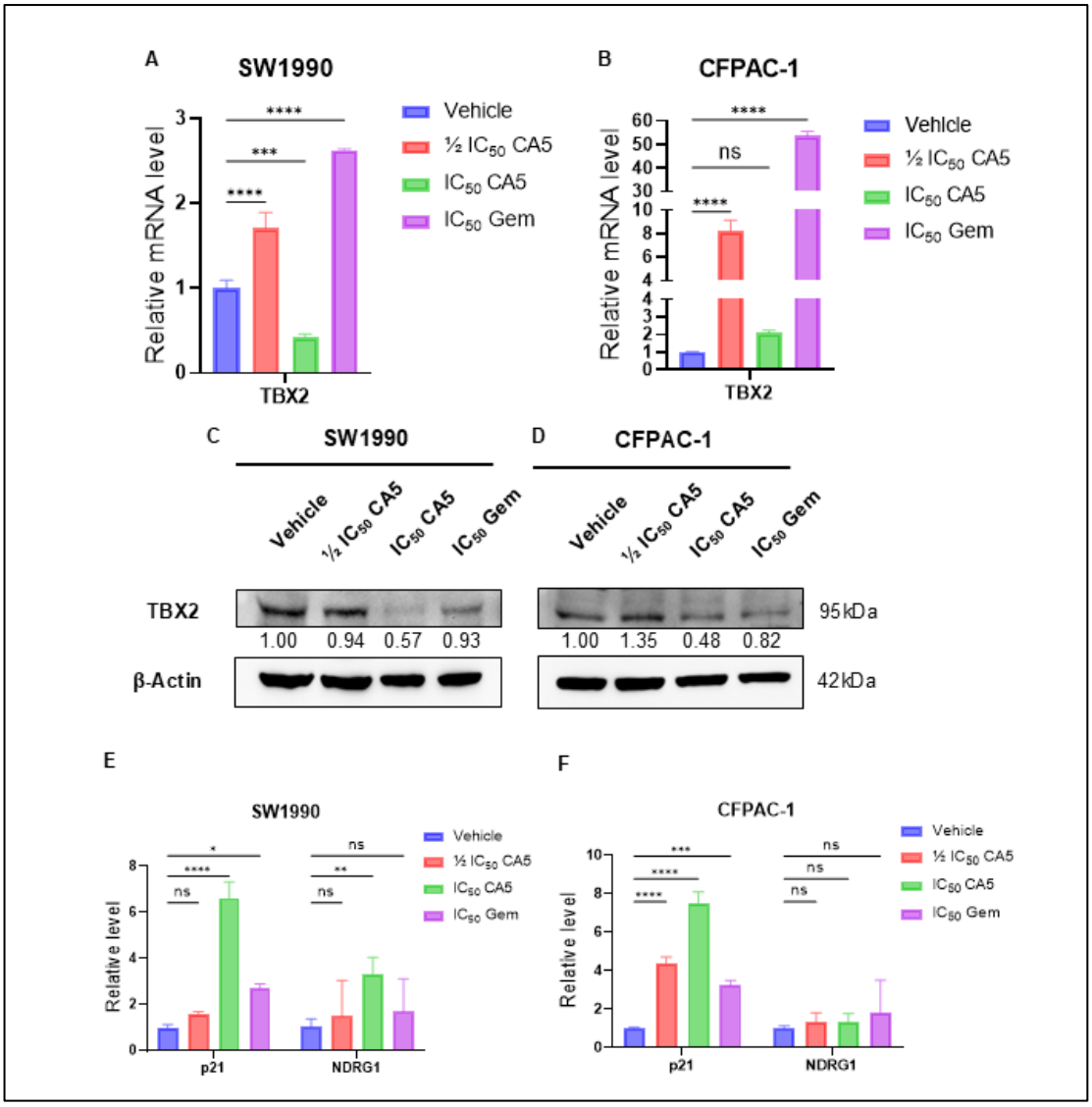

Figure 3.8. CA5-mediated transcriptional and protein-level regulation of TBX2 and its downstream target genes in PDAC cells.

A-B. Quantitative real-time PCR (qRT-PCR) analysis of TBX2 mRNA expression in SW1990 (A) and CFPAC-1 (B) cells following treatment with vehicle control, ½ IC_{50} CA5, IC_{50} CA5, or IC_{50} Gem for 48 hours. Total RNA was extracted, reverse transcribed to cDNA, and qPCR was performed using specific primers for *TBX2*. **C-D.** Western blot analysis of TBX2 levels in SW1990 (C) and CFPAC-1 (D) cells after treatment with vehicle control, ½ IC_{50} CA5, IC_{50} CA5, or IC_{50} Gem for 48 hours. Total protein was extracted for western blot analysis. **E-F.** qRT-PCR analysis of potential TBX2 downstream target genes in SW1990 (E) and CFPAC-1 (F) cells treated with vehicle control, ½ IC_{50} CA5, IC_{50} CA5, or IC_{50} Gem for 48 hours. Total RNA was extracted, reverse transcribed to cDNA, and qPCR was performed using specific primers to *p21* and *NDRG1*.

The numbers below the western blotting bands represent the average densitometry values from three biological repeats and protein band intensities were measured using ImageJ software and normalized to β-actin. Relative mRNA levels were calculated using the ΔΔCt method, with *GUSB* serving as the reference gene for normalization. Data represent the mean ± SD of at least three independent experiments. Statistical analysis was performed using two-way ANOVA followed by *post hoc* test, with *p<0.05, **p<0.01, ***p<0.001, ****p<0.0001, ns indicates no significant difference.

TBX2 has been reported to execute its oncogenic functions in breast cancer and rhabdomyosarcoma, in part, through its ability to transcriptionally repress tumour suppressors genes such as *p21*, and *NDRG1*[145,146]. These two genes have also been shown to function as tumour suppressors in PDAC[147,148] and it was therefore anticipated that the inhibition of TBX2 by CA5 may result in their de-repression. Indeed, qRT-PCR analyses showed that following IC_{50} CA5 treatment, *p21* and *NDRG1* were significantly upregulated in SW1990 cells (**Figure 3.8E**) and in CFPAC-1 cells, *p21* levels were significantly upregulated and *NDRG1* levels also increased, albeit not significantly (**Figure 3.8F**).

These findings suggest that the anti-cancer effects of CA5 may result, in part, from its ability to inhibit TBX2 and consequently allowing for the expression of key tumour suppressor genes.

3.2.7.1. TBX2 overexpression increases the sensitivity of SW1990 cells to CA5

A previous study reported that changes in TBX2 levels in melanoma can influence the efficacy of CA5[144]. To assess if this is also the case in PDAC, stable Dox-inducible TBX2-Flag cell lines were established using the piggyBac transposon system which involves the use of plasmids with DNA transposable elements flanking the DNA of interest. A transposase enzyme recognises the transposon-specific inverted repeats flanking the DNA of interest within the transposon vector and efficiently inserts this DNA into TTAA chromosomal sites of the host genome[149]. To ensure controllable

expression of TBX2 with minimal or no pleiotropic effects, the Tetracycline On (Tet-On) system was employed in which TBX2-Flag expression was under the control of the tetracycline inducible human cytomegalovirus (hCMV1) promoter. Expression of TBX2-Flag therefore occurred only in the presence of tetracycline, or its derivative doxycycline (Dox) and expression levels could be controlled by altering the concentration of Dox. Briefly, SW1990 cells stably transfected with the empty vector (EV-Flag), or TBX2-Flag were selected by treatment with the antibiotic Geneticin (G-418). Approximately 3 EV-Flag and 9 TBX2-Flag G-418 resistant clones were picked and expanded into cell lines and initial screening revealed that 10 μM Dox was able to induce TBX2-Flag in all 9 TBX2-Flag clones (**Figure 3.9A**). To identify the lowest concentration of Dox that was able to induce TBX2-Flag, Clone #9, the first established clone, was treated with a range of Dox concentrations (0 to 500 nM) for 24 h and the protein harvested from these cells were subjected to western blotting with an antibody to Flag. The results obtained showed that 50 nM Dox was the lowest concentration that effectively induced TBX2-Flag levels and therefore this concentration of Dox was selected for the next experiments (**Figure 3.9B).** Based on similar TBX2-Flag levels induced at 50 nM Dox, cell morphology, and growth rates, TBX2-Flag#1, and TBX2-Flag#9, hereafter referred to as TBX2-Flag#1, and TBX2-Flag#2, were selected for further investigations and EV-Flag served as an empty vector control (**Figure 3.9C**). Furthermore, **Figure 3.9C** shows that the levels of Dox induced TBX2-Flag decreases with time but was still detectable at 72 h.

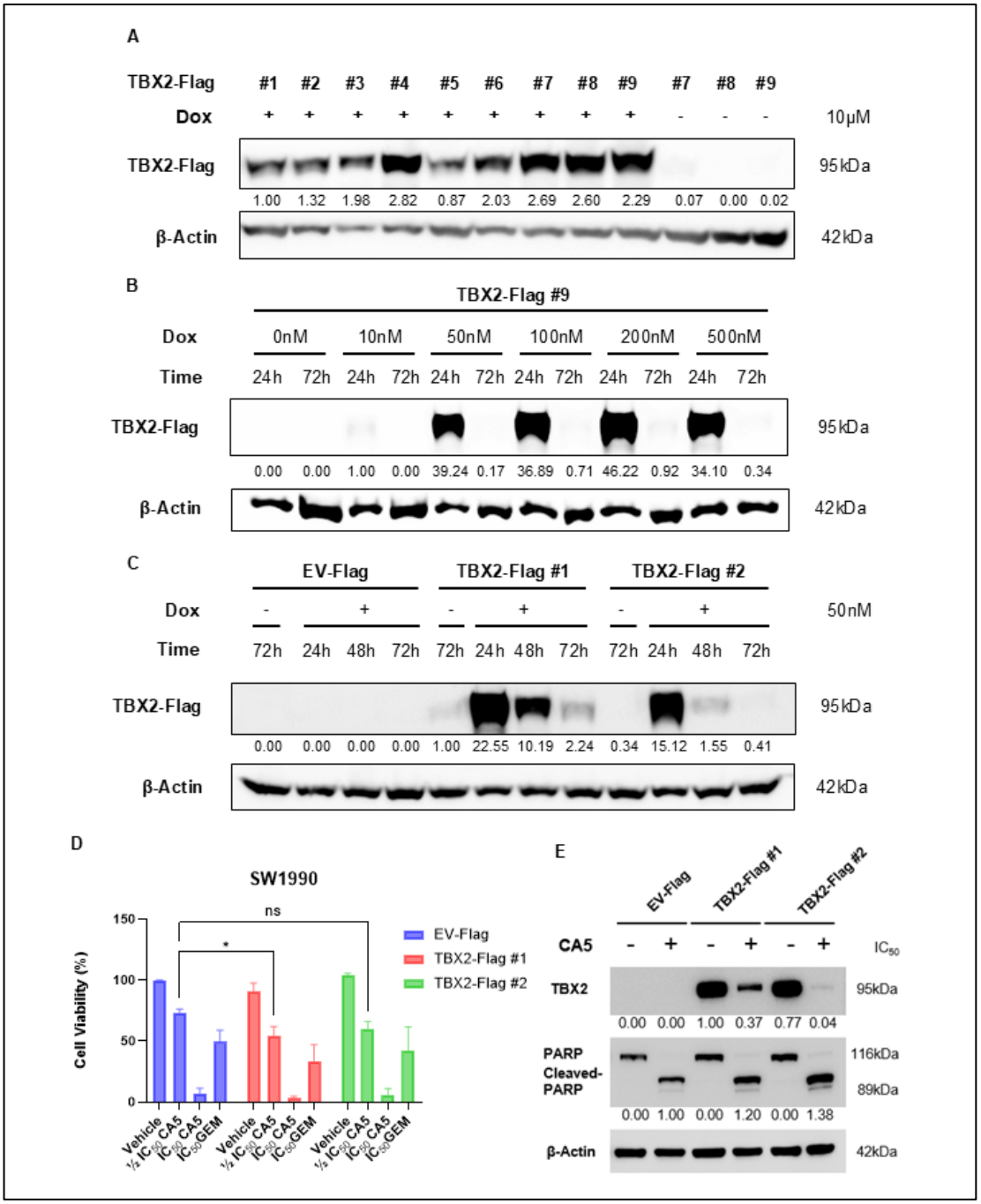

Figure 3.9. The effects of TBX2 overexpression on CA5 efficacy in SW1990 PDAC cells.

A. Western blotting screening of positive clones for Dox-inducible TBX2-Flag stable expression in SW1990 cells. The PiggyBac transposon system was used to construct Dox-inducible TBX2-Flag stable expression cell lines. Single-cell clones were isolated after 10 days of G418 selection, and TBX2-Flag expression was detected after 24 hours of 10 μM doxycycline induction. **B.** Dose-dependent and temporal analysis of TBX2-Flag expression in TBX2-Flag stable clone #9. Cells were treated with doxycycline (0-

500 nM) for 24 hours, and TBX2-Flag levels were analysed by western blotting at the end of induction and 48 hours post-induction. **C.** Time-course analysis of TBX2-Flag expression patterns in selected stable clones. EV-Flag (empty vector control), TBX2-Flag#1, and TBX2-Flag#2 (previously referred to as #9) clones were treated with 50 nM doxycycline, and TBX2-Flag expression was analysed by western blotting at the end of induction, 24 and 48 hours post-induction. **D.** Cell viability analysis of EV-Flag, TBX2-Flag#1, and TBX2-Flag#2 clones that were pretreated with 50 nM doxycycline for 24 hours to induce TBX2 expression, then treated with vehicle control, ½ IC_{50} CA5, IC_{50} CA5, or IC_{50} Gem for 48 hours. Cell viability was assessed using the MTT assay. **E.** Western blot analysis of apoptosis markers in TBX2-Flag expressing cells after CA5 treatment. TBX2-Flag clones were pretreated with 50 nM doxycycline for 24 hours, followed by drug treatment as described above. Total protein was extracted for western blot analysis of TBX2-Flag and Cleaved-PARP expression levels.
The numbers below the western blotting bands represent the average densitometry values normalized to β-actin using ImageJ software. Data represent the mean ± SD of at least three independent experiments. Statistical analysis was performed using three-way ANOVA followed by *post hoc* test, with *p<0.05, **p<0.01, ***p<0.001, ****p<0.0001, ns indicates no significant difference.

To investigate the effect of overexpressing TBX2 on the cytotoxicity of CA5, EV-Flag and TBX2-Flag#1, and TBX2-Flag#2 clones were treated with Dox for 24 h after which the cells were treated with CA5 for 48 h and then MTT assays were performed. As expected, the results revealed that CA5 inhibited cell viability of the EV-Flag and TBX2-Flag clones in a dose-dependent manner (**Figure 9D**). Importantly, Dox-induced TBX2-Flag cells were more sensitive to ½ IC_{50} CA5 treatment compared to EV-Flag (**Figure 9D**). Interestingly, treatment of EV-Flag and TBX2-Flag clones with IC_{50} CA5 in the presence of Dox, resulted in <10% viable cells in all 3 clones which suggests that Dox sensitized the cells to this concentration of CA5. However, western blotting of protein from EV-Flag and TBX2-Flag clones treated with IC_{50} CA5 showed that TBX2-Flag cells had higher levels of cleaved PARP (**Figure 9E**). This indicates, that while not obvious from the MTT cell viability assays in **Figure 9D**, that increased levels of TBX2 did indeed sensitise the PDAC cells to CA5. It is worth noting that Dox did not impact the sensitivity of the EV-Flag cells to IC_{50} Gem as approximately 50% of the

cells survived the combined treatment. However, compared to the EV-Flag cells, the TBX2-Flag cells treated with Dox + Gem resulted in cell viability less than 50% which suggests that TBX2 sensitised these cells to Gem.

Overall, CA5 demonstrated robust anti-PDAC activity through diverse mechanisms. It exhibited potent short-term and long-term cytotoxicity in both 2D and 3D cell cultures, surpassing gemcitabine in efficacy while maintaining good selectivity for cancer cells. The compound effectively inhibited cell migration, induced DNA damage, and triggered apoptosis via both intrinsic and extrinsic pathways. Its mode of action involves DNA-binding and modulation of TBX2 levels, with TBX2 overexpression enhancing CA5's effectiveness in certain cell lines. These comprehensive findings underscore CA5's promise as a potential therapeutic agent for PDAC.

CHAPTER 4
Discussion and Conclusion

PDAC remains one of the most lethal cancers, with a dismal 5-year survival rate of 13%[150]. Current treatments, including surgery and chemotherapy, show limited efficacy due to late diagnosis and therapy resistance, highlighting an urgent need for effective therapeutic strategies[151,152]. TBX2, a transcription factor frequently overexpressed in multiple cancers, drives cancer progression by regulating cell cycle and epithelial-mesenchymal transition (EMT)[153]. Notably, TBX2 is highly expressed in PDAC and correlates with poor prognosis and distant metastasis suggesting that it may be a central regulator of PDAC and therefore a novel therapeutic target to treat this highly lethal disease[41]. The Prince laboratory in collaboration with the Costa-Lotufo laboratory in Brazil have previously reported that Chromomycin A5 (CA5) has a strong binding affinity for TBX2 and exhibits anticancer activities in TBX2-driven breast cancer, melanoma, and rhabdomyosarcoma cells[91]. This study investigated the role of TBX2 in the pathogenesis of PDAC and evaluated the anticancer activities of CA5 in PDAC cells. The results show that (1) the depletion of TBX2 had minimal impact on PDAC cell proliferation, but significantly impaired cell migration; and (2) CA5 demonstrated potent and selective anticancer activity in PDAC cells through multiple mechanisms, including inducing DNA damage, cell cycle arrests, and apoptosis, and that its cytotoxicity was partially dependent on its ability to interfere with TBX2.

4.1. The role of TBX2 in PDAC cell proliferation and migration

TBX2 has been reported to be overexpressed in a range of cancer types where it frequently correlates with clinical stage and overall poor patient survival and

contributes to cancer hallmarks such as proliferation, migration, metastasis, resistance to cell death, and conferring drug resistance[62–80]. While the expression of TBX2 positively correlates with PDAC progression and metastasis[41] whether it contributes to these processes were not known at the start of this study. This study revealed a distinct function for TBX2 in PDAC, where short-term depletion of TBX2 had minimal impact on cell proliferation but significantly impaired cell migration. These results suggest that TBX2 contributes to PDAC cell invasion and metastasis and are consistent with the findings that TBX2 expression positively correlates with PDAC metastasis[41] and its roles in pro-invasion and migration in lung, breast, prostate, nasopharyngeal, gastric and colorectal cancer[62–64,66,68,70,71,73,75].

Following TBX2 knockdown, we observed an unexpected pattern in EMT markers. While N-cadherin levels increased significantly, other EMT markers (E-cadherin, β-catenin and vimentin) showed minimal changes. This apparent discrepancy between reduced migration capacity and EMT marker expression can be viewed in light of Zheng et al.'s research[4], where genetic deletion of EMT transcription factors Snail and Twist through Cre-lox recombination did not affect PDAC metastasis[4]. Future studies should investigate these potential EMT-independent mechanisms to fully elucidate how TBX2 regulates PDAC cell migration.

4.2. CA5 as a Potential PDAC Therapeutic Agent

This study is the first to demonstrate the anticancer activity of CA5 in PDAC and its potential as a therapeutic agent. Through a series of experiments, CA5 is shown to exhibit potent cytotoxicity at nanomolar concentrations, significantly outperforming the reference drug gemcitabine while maintaining favourable selectivity towards PDAC cells. These findings align with previous observations in PDAC by Pettit et al. [100], which demonstrated CA5's potent activity against multiple human cancer cell lines, including

pancreatic, breast, and lung cancer[100].

The anticancer efficacy of CA5 was further validated in 3D tumour spheroid models, which better simulate the spatial structure and intercellular interactions of tumours compared to traditional 2D cell cultures[154]. In these physiologically relevant models, CA5 demonstrated superior cytotoxicity compared to gemcitabine, effectively penetrating and disrupting tumour spheroids despite their complex architecture and barriers to drug delivery. These findings suggest that CA5 could overcome common clinical challenges such as poor drug penetration and resistance development that often limit treatment efficacy in PDAC patients.

The study also showed using scratch motility and transwell assays that CA5 treatment significantly suppressed PDAC cell migration and invasion, respectively. Thus, CA5 treatment phenocopied the effects observed when TBX2 was knocked down in PDAC cells. This suggests that CA5's anti-metastatic effects may be mediated through TBX2 inhibition, but further experiments are required to test this. For example, TBX2 could be ectopically expressed post CA5 treatment to see if it can rescue the migratory and invasive potential of PDAC cells. It is worth noting that, due to the cytotoxic nature of CA5, some of the impact on cell migration and invasion may be as a result of cell death due to the prior 24 hours exposure of the cells to CA5. The inhibitory effects of CA5 on PDAC cell migration and invasion are encouraging as PDAC's highly metastatic nature represents the primary cause of patient mortality[151].

4.3. Molecular Mechanisms of CA5 Action

This study revealed that CA5 exhibited cytotoxic effects in both SW1990 and CFPAC-1 PDAC cells, though with distinct cellular responses. In SW1990 cells, CA5 induced both S-phase and G2/M phase arrest, while primarily triggering S-phase arrest in CFPAC-1 cells. Furthermore, CA5 activated different apoptotic pathways in these cell

lines: predominantly the intrinsic pathway in SW1990 cells through caspase-9 activation, while engaging both intrinsic and extrinsic pathways in CFPAC-1 cells through activation of both caspase-8 and -9[155]. These findings demonstrate CA5's ability to effectively induce cell death in PDAC cells through multiple mechanisms that vary depending on the cellular context.

Similar to CA3, which reversibly binds to CG-rich regions in the minor groove of DNA through a 2:1 complex with Mg^{2+} [99], CA5 demonstrated strong DNA-binding capabilities as revealed by fluorescence spectroscopy analysis. Upon DNA-binding, CA5 exhibited significant fluorescence quenching and a characteristic red shift in emission peak from 530 nm to 544 nm. This DNA-binding property resulted in robust DNA damage in PDAC cells, evidenced by increased γH2AX levels in both SW1990 and CFPAC-1 cells. Among the chromomycin family members, CA5 has emerged as one of the most potent compounds, showing superior cytotoxicity at nanomolar concentrations across various cancer types. Further structural characterization of CA5-DNA-binding interactions, like the available crystal structure of CA3-DNA complex[99], would provide valuable insights into the molecular basis of CA5's superior cytotoxicity compared to other chromomycin compounds.

The data also showed that CA5 reduced TBX2 levels in PDAC cell lines at high concentrations, consistent with Sahm et al.'s findings in melanoma cells[91]. However, while their study showed that TBX2 knockdown increased sensitivity to CA5[91], results from the current study revealed that overexpressing TBX2 enhanced the sensitivity of PDAC cells to CA5. This suggests that the cytotoxicity of CA5 in PDAC cells depends on the availability of TBX2 and that there may be a potential context-dependent relationship between TBX2 expression and CA5 efficacy in different cancer types. The inhibition of TBX2 by CA5 had functional consequences, as it relieved the repression of the TBX2 target tumour suppressor NDRG1, which regulates cell motility and metastasis through modulation of EMT and cytoskeletal organisation[156]. It is important

to note that NDRG1 has not previously been validated as a TBX2 target in PDAC and it will be interesting for future promoter and functional studies to determine if this is the case.

4.4. Study Limitations and Future Directions

This study explored the role of TBX2 in PDAC and evaluated CA5 as a potential therapeutic agent through comprehensive *in vitro* experiments. While the findings provide valuable insights, several limitations need to be addressed in future research.

Firstly, while our transient knockdown experiments provided initial insights into TBX2's role in PDAC cell migration, the short-term nature of these experiments limited our understanding of TBX2's full biological functions. Future studies should employ stable or inducible knockdown systems to better characterise the long-term effects of depleting TBX2 on PDAC progression. Additionally, comprehensive transcriptomic analysis could help identify key pathways regulated by TBX2, particularly those involved in cell migration.

Secondly, all experiments were conducted in *in vitro* models, and the results need to be validated in animal models. This is important as the complexity of the *in vivo* environment, including tumour microenvironment and drug pharmacokinetics, may significantly influence CA5's efficacy and mechanisms of action.

Finally, future studies should explore strategies such as targeted delivery systems or structural modifications to enhance the tumour specificity of CA5. In addition, developing CA5 as an anti-PDAC drug would be improved through a systematic pharmacodynamic approach, particularly focusing on its potential synergistic effects with current standard-of-care treatments. Furthermore, studies should explore whether CA5 could enhance the efficacy of existing chemotherapeutic agents like gemcitabine and nab-paclitaxel, or targeted therapies such as the PARP inhibitor, Olaparib, which

might lead to more effective combination treatment strategies for PDAC.

4.5. Conclusion

In conclusion, this study provides evidence that TBX2 promotes PDAC cell migration through a mechanism that may be EMT-independent (**Figure 4.1**). These findings contribute to our understanding of TBX2's biological functions in PDAC and highlights its potential as a therapeutic target. However, further investigations are required to confirm its central role in PDAC.

The anticancer activity of CA5, a TBX2-targeting drug, appears to involve its ability to induce DNA damage leading to cell cycle arrests and cell death through apoptosis which is dependent on its ability to inhibit TBX2 (**Figure 4.1**). Given TBX2's role in conferring resistance to DNA damaging agents through its ability to repair DNA, suggests that the ability of CA5 to induce DNA damage while inhibiting TBX2 may prevent drug resistance development in PDAC cells. Future research should focus on strategies to improve the therapeutic selectivity of CA5 to advance these findings towards clinical application.

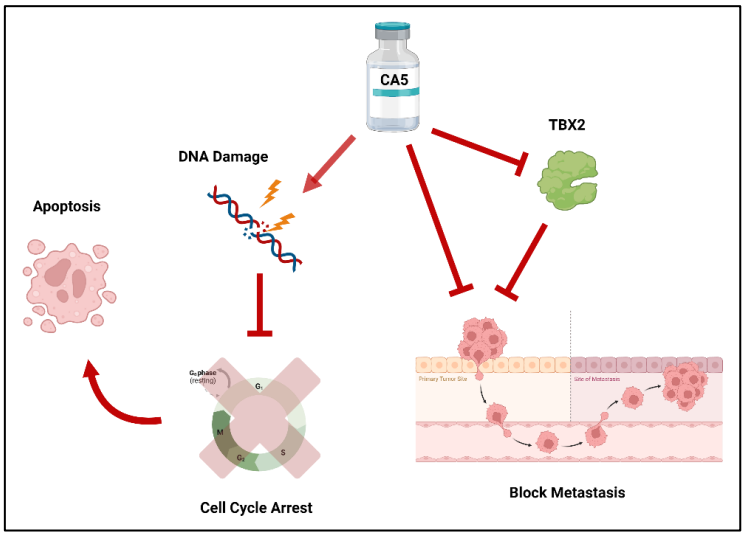

Figure 4.1. Mechanistic overview of CA5's anti-cancer activities: DNA damage, cell cycle arrest, apoptosis, and anti-metastatic effects partially through TBX2 inhibition.

CHAPTER 5
References

1. Ilic, I. & Ilic, M. International patterns in incidence and mortality trends of pancreatic cancer in the last three decades: A joinpoint regression analysis. *World J. Gastroenterol.* **28**, 4698–4715 (2022).
2. Siegel, R. L., Miller, K. D., Wagle, N. S. & Jemal, A. Cancer statistics, 2023. *CA. Cancer J. Clin.* **73**, 17–48 (2023).
3. Keihanian, T., Barkin, J. A. & Souto, E. O. Early Detection of Pancreatic Cancer: Risk Factors and the Current State of Screening Modalities. *Gastroenterol. Hepatol.* **17**, 254–262 (2021).
4. Olson, S. H. & Kurtz, R. C. Epidemiology of Pancreatic Cancer and the Role of Family History. *J. Surg. Oncol.* **107**, 1–7 (2013).
5. Yadav, D. & Lowenfels, A. B. The Epidemiology of Pancreatitis and Pancreatic Cancer. *Gastroenterology* **144**, 1252–1261 (2013).
6. Klein, A. P. Pancreatic cancer epidemiology: understanding the role of lifestyle and inherited risk factors. *Nat. Rev. Gastroenterol. Hepatol.* **18**, 493–502 (2021).
7. Kong, X., Sun, T., Kong, F., Du, Y. & Li, Z. Chronic Pancreatitis and Pancreatic Cancer. *Gastrointest. Tumors* **1**, 123–134 (2014).
8. Xiao, B., Jiang, Z.-Q., Hu, J.-X., Zhang, X.-M. & Xu, H.-B. Differentiating pancreatic neuroendocrine tumors from pancreatic ductal adenocarcinomas by the "Duct-Road Sign". *Medicine (Baltimore)* **98**, e16960 (2019).
9. Wen, J. *et al.* The Eighth Edition of the American Joint Committee on Cancer Distant Metastases Stage Classification for Metastatic Pancreatic Neuroendocrine Tumors Might Be Feasible for Metastatic Pancreatic Ductal Adenocarcinomas. *Neuroendocrinology* **110**, 364–376 (2019).
10. Görgülü, K. *et al.* The Role of Autophagy in Pancreatic Cancer: From Bench to the Dark Bedside. *Cells* **9**, 1063 (2020).
11. Karpińska, M. & Czauderna, M. Pancreas—Its Functions, Disorders, and Physiological Impact on the Mammals' Organism. *Front. Physiol.* **13**, 807632 (2022).
12. Anatomy Of Pancreas Infographics. *Vecteezy* https://www.vecteezy.com/vector-art/10366557-anatomy-of-pancreas-infographics.
13. Bhagavan, N. V. & Ha, C.-E. Chapter 20 - Perturbations of Energy Metabolism: Obesity and Diabetes Mellitus. in *Essentials of Medical Biochemistry* (eds. Bhagavan, N. V. & Ha, C.-E.) 261–274 (Academic Press, San Diego, 2011). doi:10.1016/B978-0-12-095461-2.00020-5.
14. Da Silva Xavier, G. The Cells of the Islets of Langerhans. *J. Clin. Med.* **7**, 54 (2018).

15. Paniccia, A. & Schulick, R. D. Chapter 4 - Pancreatic Physiology and Functional Assessment. in *Blumgart's Surgery of the Liver, Biliary Tract and Pancreas, 2-Volume Set (Sixth Edition)* (ed. Jarnagin, W. R.) 66-76.e3 (Elsevier, Philadelphia, 2017). doi:10.1016/B978-0-323-34062-5.00004-2.
16. Grant, T. J., Hua, K. & Singh, A. Molecular Pathogenesis of Pancreatic Cancer. *Prog. Mol. Biol. Transl. Sci.* **144**, 241–275 (2016).
17. Basturk, O. *et al.* A REVISED CLASSIFICATION SYSTEM AND RECOMMENDATIONS FROM THE BALTIMORE CONSENSUS MEETING FOR NEOPLASTIC PRECURSOR LESIONS IN THE PANCREAS. *Am. J. Surg. Pathol.* **39**, 1730–1741 (2015).
18. Westphalen, C. B. & Olive, K. P. Genetically Engineered Mouse Models of Pancreatic Cancer. *Cancer J. Sudbury Mass* **18**, 502–510 (2012).
19. Lee, A. Y. L. *et al.* Cell of origin affects tumor development and phenotype in pancreatic ductal adenocarcinoma. *Gut* **68**, 487–498 (2019).
20. Orth, M. *et al.* Pancreatic ductal adenocarcinoma: biological hallmarks, current status, and future perspectives of combined modality treatment approaches. *Radiat. Oncol.* **14**, 141 (2019).
21. Stefanoudakis, D. *et al.* Significance of TP53, CDKN2A, SMAD4 and KRAS in Pancreatic Cancer. *Curr. Issues Mol. Biol.* **46**, 2827–2844 (2024).
22. Korc, M. Pathways for aberrant angiogenesis in pancreatic cancer. *Mol. Cancer* **2**, 8 (2003).
23. Waters, A. M. & Der, C. J. KRAS: The Critical Driver and Therapeutic Target for Pancreatic Cancer. *Cold Spring Harb. Perspect. Med.* **8**, a031435 (2018).
24. Zhao, M., Mishra, L. & Deng, C.-X. The role of TGF-β/SMAD4 signaling in cancer. *Int. J. Biol. Sci.* **14**, 111–123 (2018).
25. Garajová, I., Peroni, M., Gelsomino, F. & Leonardi, F. A Simple Overview of Pancreatic Cancer Treatment for Clinical Oncologists. *Curr. Oncol.* **30**, 9587–9601 (2023).
26. Allen, P. J. *et al.* A Selective Approach to the Resection of Cystic Lesions of the Pancreas: Results From 539 Consecutive Patients. *Trans. Meet. Am. Surg. Assoc.* **124**, 237–247 (2006).
27. Hartwig, W. & Büchler, M. W. Pancreatic Cancer: Current Options for Diagnosis, Staging and Therapeutic Management. *Gastrointest. Tumors* **1**, 41–52 (2013).
28. Gaillard, F. Pancreatic cancer (staging) | Radiology Reference Article | Radiopaedia.org. *Radiopaedia* https://radiopaedia.org/articles/pancreatic-cancer-staging doi:10.53347/rID-6737.
29. O'Kane, G., Ladak, F. & Gallinger, S. Advances in the management of pancreatic ductal adenocarcinoma. *Can. Med. Assoc. J.* **193**, E844–E851 (2021).
30. Tummers, W. S. *et al.* Impact of resection margin status on recurrence and survival in pancreatic cancer surgery. *Br. J. Surg.* **106**, 1055–1065 (2019).
31. Ho, C.-K., Kleeff, J., Friess, H. & Büchler, M. W. Complications of pancreatic surgery. *HPB* **7**, 99–108 (2005).

32. Conroy, T. *et al.* FOLFIRINOX or Gemcitabine as Adjuvant Therapy for Pancreatic Cancer. *N. Engl. J. Med.* **379**, 2395–2406 (2018).
33. Principe, D. R. *et al.* The Current Treatment Paradigm for Pancreatic Ductal Adenocarcinoma and Barriers to Therapeutic Efficacy. *Front. Oncol.* **11**, 688377 (2021).
34. Wainberg, Z. A. *et al.* NALIRIFOX versus nab-paclitaxel and gemcitabine in treatment-naive patients with metastatic pancreatic ductal adenocarcinoma (NAPOLI 3): a randomised, open-label, phase 3 trial. *The Lancet* **402**, 1272–1281 (2023).
35. Valkenburg, K. C., de Groot, A. E. & Pienta, K. C. Targeting the tumour stroma to improve cancer therapy. *Nat. Rev. Clin. Oncol.* **15**, 366–381 (2018).
36. Alvarez, R. *et al.* Stromal disrupting effects of nab-paclitaxel in pancreatic cancer. *Br. J. Cancer* **109**, 926–933 (2013).
37. Zhang, L., Sanagapalli, S. & Stoita, A. Challenges in diagnosis of pancreatic cancer. *World J. Gastroenterol.* **24**, 2047–2060 (2018).
38. Xia, A.-L., Wang, X.-C., Lu, Y.-J., Lu, X.-J. & Sun, B. Chimeric-antigen receptor T (CAR-T) cell therapy for solid tumors: challenges and opportunities. *Oncotarget* **8**, 90521–90531 (2017).
39. Bochum, S., Berger, S. & Martens, U. M. Olaparib. *Recent Results Cancer Res. Fortschritte Krebsforsch. Progres Dans Rech. Sur Cancer* **211**, 217–233 (2018).
40. Helleday, T. The underlying mechanism for the PARP and BRCA synthetic lethality: Clearing up the misunderstandings. *Mol. Oncol.* **5**, 387–393 (2011).
41. Duo, S. *et al.* Expression and clinical significance of tbx2 in pancreatic cancer. *Asian Pac. J. Cancer Prev. APJCP* **10**, 118–122 (2009).
42. Abrahams, A., Parker, M. I. & Prince, S. The T-box transcription factor Tbx2: its role in development and possible implication in cancer. *IUBMB Life* **62**, 92–102 (2010).
43. Li, S. *et al.* Context-dependent T-BOX transcription factor family: from biology to targeted therapy. *Cell Commun. Signal.* **22**, 350 (2024).
44. Dong, L., Lyu, X., Faleti, O. D. & He, M.-L. The special stemness functions of Tbx3 in stem cells and cancer development. *Semin. Cancer Biol.* **57**, 105–110 (2019).
45. Lu, J., Li, X.-P., Dong, Q., Kung, H. & He, M.-L. TBX2 and TBX3: The special value for anticancer drug targets. *Biochim. Biophys. Acta BBA - Rev. Cancer* **1806**, 268–274 (2010).
46. Campbell, C., Goodrich, K., Casey, G. & Beatty, B. Cloning and Mapping of a Human Gene (TBX2) Sharing a Highly Conserved Protein Motif with the Drosophila *omb* Gene. *Genomics* **28**, 255–260 (1995).
47. Paxton, C., Zhao, H., Chin, Y., Langner, K. & Reecy, J. Murine Tbx2 contains domains that activate and repress gene transcription. *Gene* **283**, 117–124 (2002).
48. Wilson, V. & Conlon, F. L. The T-box family. *Genome Biol.* **3**, REVIEWS3008 (2002).

49. Lingbeek, M. E., Jacobs, J. J. L. & van Lohuizen, M. The T-box repressors TBX2 and TBX3 specifically regulate the tumor suppressor gene p14ARF via a variant T-site in the initiator. *J. Biol. Chem.* **277**, 26120–26127 (2002).
50. Lu, S. *et al.* TBX2 controls a proproliferative gene expression program in melanoma. *Genes Dev.* **35**, 1657–1677 (2021).
51. Vance, K. W., Carreira, S., Brosch, G. & Goding, C. R. Tbx2 is overexpressed and plays an important role in maintaining proliferation and suppression of senescence in melanomas. *Cancer Res.* **65**, 2260–2268 (2005).
52. Redmond, K. L. *et al.* T-box 2 represses NDRG1 through an EGR1-dependent mechanism to drive the proliferation of breast cancer cells. *Oncogene* **29**, 3252–3262 (2010).
53. D'Costa, Z. C. *et al.* TBX2 represses CST6 resulting in uncontrolled legumain activity to sustain breast cancer proliferation: a novel cancer-selective target pathway with therapeutic opportunities. *Oncotarget* **5**, 1609–1620 (2014).
54. Showell, C., Binder, O. & Conlon, F. L. T-box genes in early embryogenesis. *Dev. Dyn. Off. Publ. Am. Assoc. Anat.* **229**, 201–218 (2004).
55. Aanhaanen, W. T. J. *et al.* The Tbx2+ primary myocardium of the atrioventricular canal forms the atrioventricular node and the base of the left ventricle. *Circ. Res.* **104**, 1267–1274 (2009).
56. Suzuki, T., Takeuchi, J., Koshiba-Takeuchi, K. & Ogura, T. Tbx Genes Specify Posterior Digit Identity through Shh and BMP Signaling. *Dev. Cell* **6**, 43–53 (2004).
57. Jerome-Majewska, L. A. *et al.* Tbx3, the ulnar-mammary syndrome gene, and Tbx2 interact in mammary gland development through a p19Arf/p53-independent pathway. *Dev. Dyn. Off. Publ. Am. Assoc. Anat.* **234**, 922–933 (2005).
58. Rowton, M. *et al.* Regulation of mesenchymal-to-epithelial transition by PARAXIS during somitogenesis. *Dev. Dyn. Off. Publ. Am. Assoc. Anat.* **242**, 1332–1344 (2013).
59. Liu, N. *et al.* Functional variants in TBX2 are associated with a syndromic cardiovascular and skeletal developmental disorder. *Hum. Mol. Genet.* **27**, 2454–2465 (2018).
60. Behesti, H., Papaioannou, V. E. & Sowden, J. C. Loss of Tbx2 delays optic vesicle invagination leading to small optic cups. *Dev. Biol.* **333**, 360–372 (2009).
61. Radio, F. C. *et al.* TBX2 gene duplication associated with complex heart defect and skeletal malformations. *Am. J. Med. Genet. A.* **152A**, 2061–2066 (2010).
62. Wang, B. *et al.* The T Box Transcription Factor TBX2 Promotes Epithelial-Mesenchymal Transition and Invasion of Normal and Malignant Breast Epithelial Cells. *PLoS ONE* **7**, e41355 (2012).
63. Alqatati, A. *et al.* The expression level of T-box transcription factor TBX2 in breast cancer and its clinical significance. *World Cancer Res. J.* **8**, (2021).
64. Tasaka, R. *et al.* TBX2 expression is associated with platinum-sensitivity of ovarian serous carcinoma. *Oncol. Lett.* **15**, 3085–3090 (2018).
65. Liu, X. *et al.* TBX2 overexpression promotes proliferation and invasion through

epithelial-mesenchymal transition and ERK signaling pathway. *Exp. Ther. Med.* (2018) doi:10.3892/etm.2018.7028.
66. Lu, J. *et al.* TBX2 Expression predicts Tumor Recurrence and Adjuvant Chemotherapy Benefits in Gastric Cancer Patients following R0 Resection: a proposed approach for risk stratification. *J. Cancer* **11**, 3172–3179 (2020).
67. Chen, P., Tian, D. & Liu, M. The role of Tbx2 in pancreatic cancers and its regulation by Wnt/β-catenin signaling. *Chin.-Ger. J. Clin. Oncol.* **7**, 404–409 (2008).
68. Yu, H. *et al.* TBX2 Identified as a Potential Predictor of Bone Metastasis in Lung Adenocarcinoma via Integrated Bioinformatics Analyses and Verification of Functional Assay. *J. Cancer* **11**, 388–402 (2020).
69. Du, W.-L. *et al.* Effect of silencing the T-Box transcription factor TBX2 in prostate cancer PC3 and LNCaP cells. *Mol. Med. Rep.* **16**, 6050–6058 (2017).
70. Nandana, S. *et al.* Bone Metastasis of Prostate Cancer Can Be Therapeutically Targeted at the TBX2–WNT Signaling Axis. *Cancer Res.* **77**, 1331–1344 (2017).
71. Han, Y. *et al.* Increased expression of TBX2 is a novel independent prognostic biomarker of a worse outcome in colorectal cancer patients after curative surgery and a potential therapeutic target. *Med. Oncol.* **30**, 688 (2013).
72. Zhou, Y., Dong, M. & Li, X. TBX2-WNT3A Axis Mediates the Development of Colorectal Cancer In Vitro and In Vivo. *Adv. Ther.* **6**, 2200306 (2023).
73. Yin, D. *et al.* Circ_0060927 promotes colorectal cancer development by sponging miR-331-3p and upregulating TBX2. *Pathol. Res. Pract.* **264**, 155673 (2024).
74. Hu, R. *et al.* Clinical significance of TBX2 in esophageal squamous cell carcinomas and its role in cell migration and invasion. *Eur. Rev. Med. Pharmacol. Sci.* **24**, 3062–3068 (2020).
75. Lv, Y. *et al.* TBX2 over-expression promotes nasopharyngeal cancer cell proliferation and invasion. *Oncotarget* **8**, 52699–52707 (2017).
76. Yi, F., Du, J., Ni, W. & Liu, W. Tbx2 confers poor prognosis in glioblastoma and promotes temozolomide resistance with change of mitochondrial dynamics. *OncoTargets Ther.* **10**, 1059 (2017).
77. Liu, W.-K., Jiang, X.-Y. & Zhang, Z.-X. Expression of PSCA, PIWIL1, and TBX2 in Endometrial Adenocarcinoma. *Onkologie* **33**, 241–245 (2010).
78. Ding, N., Zhang, T., Yu, X. & Zhuang, S. T-Box Transcription Factor 2 Enhances Chemoresistance of Endometrial Cancer by Mediating NRF2 Expression. *Curr. Protein Pept. Sci.* **23**, 563–570 (2022).
79. Zhu, B. *et al.* TBX2 represses PTEN in rhabdomyosarcoma and skeletal muscle. *Oncogene* **35**, 4212–4224 (2016).
80. Mohamad, T., Kazim, N., Adhikari, A. & Davie, J. K. EGR1 interacts with TBX2 and functions as a tumor suppressor in rhabdomyosarcoma. *Oncotarget* **9**, 18084–18098 (2018).
81. Hanahan, D. Hallmarks of Cancer: New Dimensions. *Cancer Discov.* **12**, 31–46 (2022).

82. Prince, S., Carreira, S., Vance, K. W., Abrahams, A. & Goding, C. R. Tbx2 Directly Represses the Expression of the p21WAF1 Cyclin-Dependent Kinase Inhibitor. *Cancer Res.* **64**, 1669–1674 (2004).
83. Jacobs, J. J. *et al.* Senescence bypass screen identifies TBX2, which represses Cdkn2a (p19(ARF)) and is amplified in a subset of human breast cancers. *Nat. Genet.* **26**, 291–299 (2000).
84. Zhu, B., Zhang, M., Byrum, S. D., Tackett, A. J. & Davie, J. K. TBX2 blocks myogenesis and promotes proliferation in rhabdomyosarcoma cells. *Int. J. Cancer* **135**, 785–797 (2014).
85. Ribatti, D., Tamma, R. & Annese, T. Epithelial-Mesenchymal Transition in Cancer: A Historical Overview. *Transl. Oncol.* **13**, 100773 (2020).
86. Kumar, S. *et al.* A pathway for the control of anoikis sensitivity by E-cadherin and epithelial-to-mesenchymal transition. *Mol. Cell. Biol.* **31**, 4036–4051 (2011).
87. Wansleben, S., Davis, E., Peres, J. & Prince, S. A novel role for the anti-senescence factor TBX2 in DNA repair and cisplatin resistance. *Cell Death Dis.* **4**, e846–e846 (2013).
88. Davis, E. *et al.* Ectopic Tbx2 expression results in polyploidy and cisplatin resistance. *Oncogene* **27**, 976–984 (2008).
89. Yu, X., Yao, X., Song, F. & Zhu, X. T-Box Transcription Factor 2 Mediates Chemoresistance of Endometrial Cancer via Regulating FSP1-involved Ferroptosis. *Cell Biochem. Biophys.* (2024) doi:10.1007/s12013-024-01518-z.
90. Zhang, Z. *et al.* Loss of CHD1 Promotes Heterogeneous Mechanisms of Resistance to AR-Targeted Therapy via Chromatin Dysregulation. *Cancer Cell* **37**, 584-598.e11 (2020).
91. Del Bianco Sahm, B. *et al.* Targeting the Oncogenic TBX2 Transcription Factor With Chromomycins. *Front. Chem.* **8**, (2020).
92. Hu, Y. *et al.* Chromomycin SA analogs from a marine-derived Streptomyces sp. *Bioorg. Med. Chem.* **19**, 5183–5189 (2011).
93. Chakrabarti, S., Dasgupta, D. & Bhattacharyya, D. Role of Mg2+ in Chromomycin A3 – DNA Interaction: A Molecular Modeling Study. *J. Biol. Phys.* **26**, 203–218 (2000).
94. Pinto, F. *et al.* Dextrorotatory Chromomycins from the Marine Streptomyces sp. Associated to Palythoa caribaeorum. *J. Braz. Chem. Soc.* **31**, (2019).
95. Toume, K., Tsukahara, K., Ito, H., Arai, M. A. & Ishibashi, M. Chromomycins A2 and A3 from marine actinomycetes with TRAIL resistance-overcoming and Wnt signal inhibitory activities. *Mar. Drugs* **12**, 3466–3476 (2014).
96. Miyamoto, M. *et al.* Chromomycin A2, A3 and A4. *Tetrahedron* **23**, 421–437 (1967).
97. PubChem. PubChem. https://pubchem.ncbi.nlm.nih.gov/.
98. Guimarães, L. A. *et al.* Chromomycin A2 induces autophagy in melanoma cells. *Mar. Drugs* **12**, 5839–5855 (2014).
99. Bank, R. P. D. RCSB PDB - 1VAQ: Crystal structure of the Mg2+-(chromomycin

A3)2-d(TTGGCCAA)2 complex reveals GGCC binding specificity of the drug dimer chelated by metal ion. https://www.rcsb.org/structure/1vaq.
100. Pettit, G. *et al.* Antineoplastic agents 596. Isolation and structure of chromomycin A5 from a Beaufort Sea microorganism. *RSC Adv.* **5**, 9116–9122 (2015).
101. Florêncio, K. G. D. *et al.* Chromomycin A5 induces bona fide immunogenic cell death in melanoma. *Front. Immunol.* **13**, 941757 (2022).
102. Segeritz, C.-P. & Vallier, L. Cell Culture. *Basic Sci. Methods Clin. Res.* 151–172 (2017) doi:10.1016/B978-0-12-803077-6.00009-6.
103. Ulrich, A. B., Schmied, B. M., Standop, J., Schneider, M. B. & Pour, P. M. Pancreatic cell lines: a review. *Pancreas* **24**, 111–120 (2002).
104. Deer, E. L. *et al.* Phenotype and Genotype of Pancreatic Cancer Cell Lines. *Pancreas* **39**, 425–435 (2010).
105. Cao, Y., Liu, X. & Peng, L. Molecular engineering of dendrimer nanovectors for siRNA delivery and gene silencing. *Front. Chem. Sci. Eng.* **11**, 1–13 (2017).
106. HiPerFect Transfection Reagent. https://www.qiagen.com/us/products/discovery-and-translational-research/functional-and-cell-analysis/transfection/hiperfect-transfection-reagent.
107. Zhao, S. *et al.* PiggyBac transposon vectors: the tools of the human gene encoding. *Transl. Lung Cancer Res.* **5**, 120–125 (2016).
108. Zhang, M. *et al.* Gene Delivery and Expression Systems in Induced Pluripotent Stem Cells. in *Interface Oral Health Science 2016* (eds. Sasaki, K., Suzuki, O. & Takahashi, N.) 121–133 (Springer, Singapore, 2017). doi:10.1007/978-981-10-1560-1_11.
109. Analytical Methods Committee Amctb No, null. PCR - the polymerase chain reaction. *Anal. Methods Adv. Methods Appl.* **6**, 333–336 (2013).
110. Mo, Y., Wan, R. & Zhang, Q. Application of Reverse Transcription-PCR and Real-Time PCR in Nanotoxicity Research. *Methods Mol. Biol. Clifton NJ* **926**, 99–112 (2012).
111. Giri, D. How COVID-19 RT-PCR Test Works? Principle and Protocol. *LaboratoryTests.org* https://laboratorytests.org/covid-19-rt-pcr/ (2020).
112. Ponchel, F. *et al.* Real-time PCR based on SYBR-Green I fluorescence: an alternative to the TaqMan assay for a relative quantification of gene rearrangements, gene amplifications and micro gene deletions. *BMC Biotechnol.* **3**, 18 (2003).
113. Livak, K. J. & Schmittgen, T. D. Analysis of relative gene expression data using real-time quantitative PCR and the 2(-Delta Delta C(T)) Method. *Methods San Diego Calif* **25**, 402–408 (2001).
114. Western blot. *Wikipedia* (2024).
115. Sule, R., Rivera, G. & Gomes, A. V. Western blotting (immunoblotting): history, theory, uses, protocol and problems. *BioTechniques* **75**, 99–114 (2023).
116. Fiji. *ImageJ Wiki* https://imagej.github.io/software/fiji/index.
117. Hulkower, K. I. & Herber, R. L. Cell Migration and Invasion Assays as Tools for

Drug Discovery. *Pharmaceutics* **3**, 107–124 (2011).
118. Segment Anything. https://segment-anything.com/.
119. GitHub - THU-MIG/yolov10: YOLOv10: Real-Time End-to-End Object Detection [NeurIPS 2024]. https://github.com/THU-MIG/yolov10.
120. Kumar, P., Nagarajan, A. & Uchil, P. D. Analysis of Cell Viability by the MTT Assay. *Cold Spring Harb. Protoc.* **2018**, (2018).
121. Prism - GraphPad. https://www.graphpad.com/prism.
122. Lee, S.-Y., Koo, I.-S., Hwang, H. J. & Lee, D. W. In Vitro three-dimensional (3D) cell culture tools for spheroid and organoid models. *SLAS Discov. Adv. Life Sci. R D* **28**, 119–137 (2023).
123. Roper, S. J., Linke, F., Scotting, P. J. & Coyle, B. 3D spheroid models of paediatric SHH medulloblastoma mimic tumour biology, drug response and metastatic dissemination. *Sci. Rep.* **11**, 4259 (2021).
124. Cribbes, S., Kessel, S., McMenemy, S., Qiu, J. & Chan, L. L.-Y. A Novel Multiparametric Drug-Scoring Method for High-Throughput Screening of 3D Multicellular Tumor Spheroids Using the Celigo Image Cytometer. *SLAS Discov. Adv. Life Sci. R D* **22**, 547–557 (2017).
125. Newlove, S. & Hamnett, R. Immunocytochemistry-Immunofluorescence The complete ICC-IF technique guide. https://www.antibodies.com/applications/immunofluorescence.
126. Im, K., Mareninov, S., Diaz, M. F. P. & Yong, W. H. An Introduction to Performing Immunofluorescence Staining. *Methods Mol. Biol. Clifton NJ* **1897**, 299–311 (2019).
127. Wilkinson, J. Applications of Advanced Fluorescence Spectroscopy. *AZoM* https://www.azom.com/article.aspx?ArticleID=13958 (2017).
128. Jyoti, T. P., Chandel, S. & Singh, R. Flow cytometry: Aspects and application in plant and biological science. *J. Biophotonics* **17**, e202300423 (2024).
129. Pozarowski, P. & Darzynkiewicz, Z. Analysis of cell cycle by flow cytometry. *Methods Mol. Biol. Clifton NJ* **281**, 301–311 (2004).
130. FlowJo. https://www.flowjo.com/.
131. Wallberg, F., Tenev, T. & Meier, P. Analysis of Apoptosis and Necroptosis by Fluorescence-Activated Cell Sorting. *Cold Spring Harb. Protoc.* **2016**, pdb.prot087387 (2016).
132. Abrahams, A., Parker, M. I. & Prince, S. The T-box transcription factor Tbx2: its role in development and possible implication in cancer. *IUBMB Life* **62**, 92–102 (2010).
133. Lu, J., Li, X.-P., Dong, Q., Kung, H. & He, M.-L. TBX2 and TBX3: The special value for anticancer drug targets. *Biochim. Biophys. Acta BBA - Rev. Cancer* **1806**, 268–274 (2010).
134. Wansleben, S., Peres, J., Hare, S., Goding, C. R. & Prince, S. T-box transcription factors in cancer biology. *Biochim. Biophys. Acta BBA - Rev. Cancer* **1846**, 380–391 (2014).

135. Duo, S. *et al.* Expression and clinical significance of tbx2 in pancreatic cancer. *Asian Pac. J. Cancer Prev. APJCP* **10**, 118–122 (2009).
136. Joshi, V. B., Gutierrez Ruiz, O. L. & Razidlo, G. L. The Cell Biology of Metastatic Invasion in Pancreatic Cancer: Updates and Mechanistic Insights. *Cancers* **15**, 2169 (2023).
137. DepMap, B. DepMap 24Q2 Public. 25031191226 Bytes Figshare+ https://doi.org/10.25452/FIGSHARE.PLUS.25880521.V1 (2024).
138. Zheng, X. *et al.* Epithelial-to-mesenchymal transition is dispensable for metastasis but induces chemoresistance in pancreatic cancer. *Nature* **527**, 525–530 (2015).
139. Forgie, B. N., Prakash, R., Goyeneche, A. A. & Telleria, C. M. Vitality, viability, long-term clonogenic survival, cytotoxicity, cytostasis and lethality: what do they mean when testing new investigational oncology drugs? *Discov. Oncol.* **15**, 5 (2024).
140. Nyga, A., Cheema, U. & Loizidou, M. 3D tumour models: novel in vitro approaches to cancer studies. *J. Cell Commun. Signal.* **5**, 239–248 (2011).
141. Hartsock, A. & Nelson, W. J. Adherens and Tight Junctions: Structure, Function and Connections to the Actin Cytoskeleton. *Biochim. Biophys. Acta* **1778**, 660–669 (2008).
142. Moon, J. *et al.* DNA Damage and Its Role in Cancer Therapeutics. *Int. J. Mol. Sci.* **24**, 4741 (2023).
143. Plesca, D., Mazumder, S. & Almasan, A. DNA Damage Response and Apoptosis. *Methods Enzymol.* **446**, 107–122 (2008).
144. Sahm, B. D. B. *et al.* Targeting the Oncogenic TBX2 Transcription Factor With Chromomycins. *Front. Chem.* **8**, (2020).
145. McIntyre, A. J. *et al.* TBX2 acts as a potent transcriptional silencer of tumour suppressor genes through interaction with the CoREST complex to sustain the proliferation of breast cancers. *Nucleic Acids Res.* **50**, 6154–6173 (2022).
146. Prince, S., Carreira, S., Vance, K. W., Abrahams, A. & Goding, C. R. Tbx2 directly represses the expression of the p21(WAF1) cyclin-dependent kinase inhibitor. *Cancer Res.* **64**, 1669–1674 (2004).
147. Angst, E. *et al.* N-myc downstream regulated gene-1 expression correlates with reduced pancreatic cancer growth and increased apoptosis in vitro and in vivo. *Surgery* **149**, 614–624 (2011).
148. Hosokawa, M. *et al.* Over-expression of cysteine proteinase inhibitor cystatin 6 promotes pancreatic cancer growth. *Cancer Sci.* **99**, 1626–1632 (2008).
149. Li, M. A. *et al.* The piggyBac Transposon Displays Local and Distant Reintegration Preferences and Can Cause Mutations at Noncanonical Integration Sites. *Mol. Cell. Biol.* **33**, 1317 (2013).
150. Post, E. Pancreatic Cancer Five-Year Survival Rate Increases to 13%. *Pancreatic Cancer Action Network* https://pancan.org/news/pancreatic-cancer-five-year-survival-rate-increases-to-13/ (2024).

151. Kleeff, J. *et al.* Pancreatic cancer. *Nat. Rev. Dis. Primer* **2**, 16022 (2016).
152. Mizrahi, J. D., Surana, R., Valle, J. W. & Shroff, R. T. Pancreatic cancer. *Lancet Lond. Engl.* **395**, 2008–2020 (2020).
153. Peres, J. *et al.* The Highly Homologous T-Box Transcription Factors, TBX2 and TBX3, Have Distinct Roles in the Oncogenic Process. *Genes Cancer* **1**, 272–282 (2010).
154. Nath, S. & Devi, G. R. Three-Dimensional Culture Systems in Cancer Research: Focus on Tumor Spheroid Model. *Pharmacol. Ther.* **163**, 94–108 (2016).
155. Lossi, L. The concept of intrinsic versus extrinsic apoptosis. *Biochem. J.* **479**, 357–384 (2022).
156. Hu, Z. *et al.* NDRG1 attenuates epithelial-mesenchymal transition of nasopharyngeal cancer cells via blocking Smad2 signaling. *Biochim. Biophys. Acta* **1852**, 1876–1886 (2015).